COMSAT
Technical Review

COMSAT TECHNICAL REVIEW
Volume 11 Number 1, Spring 1981

Enhancement of FDM-FM satellite capacity by use of compandors*

G. G. SZARVAS AND H. G. SUYDERHOUD

(Manuscript received August 20, 1980)

Abstract

This paper presents the results of a study to determine the satellite capacity enhancement obtainable by using syllabic compandors. Syllabic companding applied to the speech channels of FDM-FM carriers can increase satellite capacity by as much as 100 percent, depending on the number of channels per carrier. Syllabic compandors presently produced by integrated circuit technology are small and inexpensive.

Compandors permit a higher level of satellite circuit noise and hence an FM index (and bandwidth) which is smaller than that required for uncompanded channels. The results presented in the paper are based on compandor advantage measurements and single- and multi-channel amplitude distribution measurements for both companded and uncompanded speech signals.

For data transmission, it is estimated that about 2-dB degradation may be encountered when long terrestrial access circuits are interconnected via a companded satellite circuit for international transmission.

1

Introduction

Syllabic companding of analog telephone circuits [1] and its application to frequency-division multiplex (FDM) systems [2] have been known for several decades. The compandor consists of a compressor and an expander. The compressor, located at the transmitting end of a circuit, reduces the range of the speech signal power and generally raises the low-level passages. The expander, located at the receiving end of the circuit, restores the original signal range. In addition, during the absence of speech and during intersyllabic pauses, the expander significantly attenuates circuit noise, thereby permitting a higher level of circuit noise than would otherwise be allowable. This feature, which has been exploited for economical engineering of transmission systems [3], [4], has been applied to obtain FM bandwidth economy in satellite transmission [5], [6].

In the past, compandor applications have been restricted for several reasons. First, it was difficult and expensive to implement compressors and expanders with matching characteristics over a wide dynamic range. Second, the expander action enhances circuit loss variations which must therefore be better controlled in companded circuits than in uncompanded circuits. Finally, companded circuits, engineered for speech transmission, often degrade performance for constant-level transmission such as signaling and data.

Some of these restrictions are no longer valid because of better circuit technology implementations which have revived interest in compandor applications. Inexpensive IC compandors with performance characteristics superior to those of older devices are now available. Furthermore, loss control of networks has generally improved. For example, companding is used in satellite communications for single-channel-per-carrier transmission of generally low losses and low-loss variations, as in the MARISAT network. The performance of such a service is analyzed in Reference 7.

The present paper examines the multichannel capacity enhancement of frequency modulated (FM) satellite carriers. Enhancement is obtained by companding each voice channel within the FDM groups and supergroups which modulate the FM carriers (CFDM-FM transmission).

Ideal compandor characteristics and parameters are discussed, followed by characteristic measurements of a modern IC compandor. This compandor was used in an extensive subjective test to assess its advantages. Based on the results and on multichannel load measure-

ments of compressed speech signals, the FDM-FM capacity enhancement has been calculated for various numbers of channels and FM carrier-to-noise (C/N) ratios. The effect on data transmission, amounting to a signal-to-noise (S/N) ratio degradation, has been estimated and will be described with some signaling measurements. Finally, results of a limited subjective test of tandem companded links are presented.

Many of the measurements were performed on a laboratory-simulated satellite link from earth station to earth station. The FM carrier had a bandwidth allocation of 2.5 MHz and was loaded under a variety of C/N ratios with up to 120 FDM speech channels.

Compandor operation

Compandor transfer characteristics and functional block diagram

The two parts of a compandor, the compressor and expander, are functionally complementary. The steady-state mean square level transfer characteristics, shown in Figure 1, are linear in decibels with a
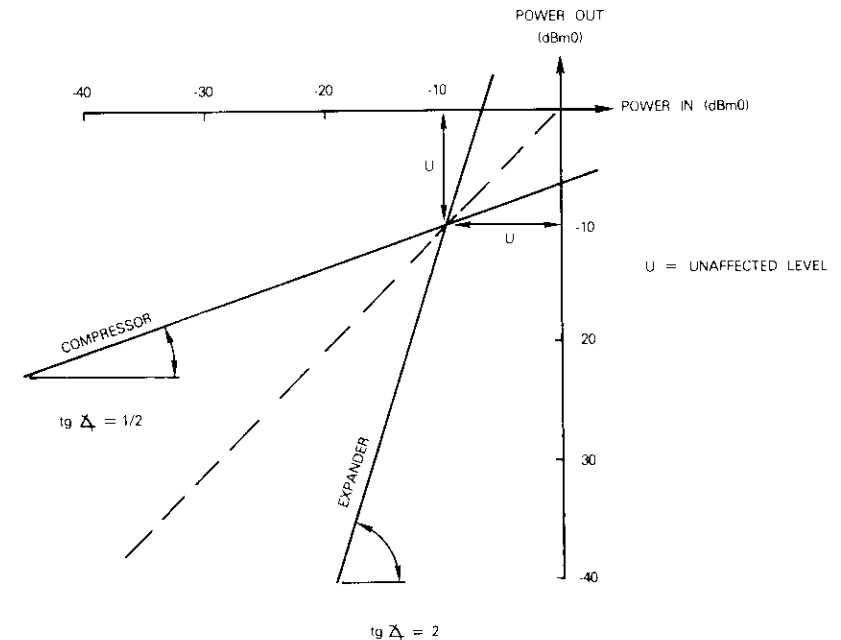

Figure 1. *Ideal Compandor Transfer Characteristics*

slope equal to $1/\alpha$ for compression and α for expansion (α is the compression ratio). The intercept shows that the signal of level U remains unchanged (after compression and after expansion); hence it is known as the "unaffected level."

The general equations relating power at input and output are

$$P_{C,\text{out}} = \frac{P_{C,\text{in}}}{\alpha} + \frac{\alpha - 1}{\alpha}U \quad \text{dBm0} \qquad \text{(compressor)} \qquad (1a)$$

$$P_{E,\text{out}} = \alpha P_{E,\text{in}} - (\alpha - 1)U \quad \text{dBm0} \qquad \text{(expander)} \quad . \qquad (1b)$$

It is appropriate to refer signal levels to the 0 transmission level point (TLP) (*i.e.*, dBm0) on both sides of the compressor and expander. However, the change in level must be carefully included in system calculations.

Telephone circuit compandors are nominally designed with $\alpha = 2$. The choice of unaffected level must be consistent with the channel loading of the system and depends on whether the system is AM or FM, single channel, or multichannel.

Level diagram description

The following nomenclature will be used (see Figure 2):

N_A = accumulated noise of the access circuit
N_S = satellite system noise contribution
N_T = total noise at the input to the expander
N_{CH} = noise appearing in the telephone channel at the output of the expander.

In the absence of the compandor,

$$N_T = N_{CH} = N_A + N_S \quad .$$

Figure 3 is a compandor level diagram derived from equations (1a) and (1b) for an unaffected level of -10 dBm0. The following examples describe some of the relevant features:

    a. Assume that only satellite system noise, N_S, exists. Equation (1b) (with $\alpha = 2$) can be used to determine the reduction in the intersyllabic or idle channel noise obtained by substituting N_S for $P_{E,\text{in}}$ and calculating the channel power, N_{CH}, at the output of the
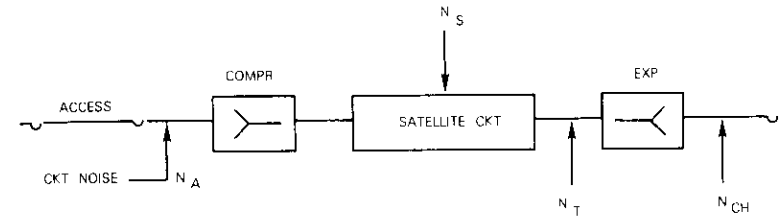
Figure 2. *Nomenclature*
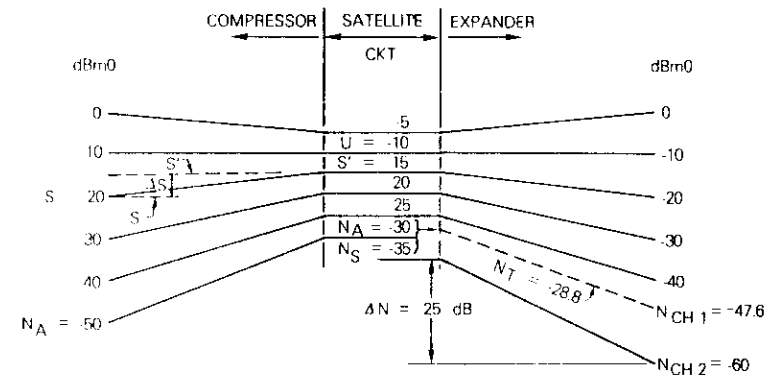
$N_{CH\ 1}$ IDLE CHANNEL NOISE WHEN N_A AND N_S EXIST
$N_{CH\ 2}$ IDLE CHANNEL NOISE WHEN ONLY N_S EXISTS

Figure 3. *Compandor Level Diagram*

expander, E. The noise reduction (in dB) is then

$$\Delta N = N_S - N_{CH} = N_S - (2N_S - U) = -N_S + U \quad . \qquad (2)$$

For example, if $N_S = -35$ dBm0 and $U = -10$ dBm0, ΔN is equal to 25 dB.

    b. Equation (1b) shows that the expander action increases system level variations by α. Therefore, transmission system level stability must be maintained within closer tolerances with compandors than without compandors.

    c. The compressor changes the access circuit signal level from

S to S' on the satellite system link, which amounts to an increase for all $S < U$ and a decrease otherwise. According to equation (1a), the change, ΔS, is equal to

$$\Delta S = S' - S = \frac{S}{2} + \frac{U}{2} - S = \frac{U - S}{2} \quad . \tag{3}$$

For example, if S is equal to -20 dBm0,

$$\Delta S = \frac{-10 + 20}{2} = 5 \, dB \quad .$$

The expander decreases the signal level by an equal amount and, during the presence of the signal, the system S/N ratio remains unchanged by the expander; thus, $N_{CH} = N_S - \Delta S$. As S, and thus S', decays to zero, however, noise is reduced by the amount calculated in equation (2).

   d. The range of the signal level decreases by a factor of 2 after compression. If S has a normal distribution with mean $\bar{S}$ and variance σ^2, $N(\bar{S}, \sigma^2)$, the compressed signal also has a normal distribution given by

$$N(\bar{S}', \sigma'^2) = N\left(\frac{\bar{S} + U}{2}, \frac{\sigma^2}{4}\right) \quad . \tag{4}$$

If, in addition to the system noise, N_s, an access circuit noise of level N_A exists, the idle channel noise (also intersyllabic noise) is given by

$$N_{CH} = 2N_T - U = 2\left\{10\log\left[\log^{-1}\left(\frac{N_A + U}{2 \times 10}\right)\right.\right.$$
$$\left.\left. + \log^{-1}\left(\frac{N_s}{10}\right)\right]\right\} - U \quad (dBm0) \tag{5}$$

and the channel "signal on" noise is given by

$$N_{CH,on} = 10\log\left[\log^{-1}\left(\frac{N_A + \Delta S}{10}\right)\right.$$
$$\left. + \log^{-1}\left(\frac{N_s}{10}\right)\right] - \Delta S \quad (dBm0) \quad . \tag{6}$$

If it is assumed that $N_A = -50$ dBm0, $N_s = -35$ dBm0, and $\Delta S = 5$ dB, N_{CH} becomes -47.6 dBm0, and $N_{CH,on}$ becomes -39.6 dBm0. If the access circuit noise is negligible, *i.e.*, $N_A \longrightarrow -\infty$, the idle channel noise level becomes -60 dBm0, whereas the channel "signal on" noise level becomes -40 dBm0. Thus, the idle channel noise is dominated by N_A, whereas the "signal on" noise is determined by the system noise level.

Transient response

Loss variations of syllabic compandors approximate syllabic variations of speech power through appropriate time constants in the signal envelope rectifiers which control compressor and expander transfer characteristics. The recommended transient response of the compandor and the attack and recovery times of the compressor have been defined for a 2000-Hz access signal step change from -16 to -4 dBm0 (attack), and a step change from -4 to -16 dBm0 (recovery) [8]. The output overshoot or undershoot should be less than 20 percent of the final level for the combination compressor-expander. The compressor attack time and recovery time should be less than 5 ms and 22.5 ms, respectively. The expander attack and recovery times should not differ significantly from those of the compressor, since excessive transient overshoot would occur.

The recovery transient of the expander causes a transition of the noise level, sometimes noticeable at the trailing end of a speech utterance, which is referred to as the "hush-hush" effect. Figure 4 illustrates this phenomenon, which assumes that the satellite system
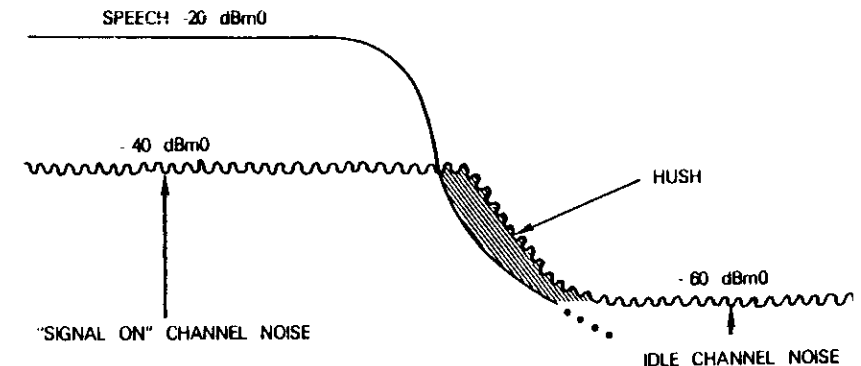

Figure 4. *Hush-Hush Effect*

speech-to-noise ratio is 20 dB, while the idle channel noise is assumed to be reduced to −60 dBm0. Under these circumstances, the "hush-hush" effect is quite noticeable.

Compandor advantage

During a telephone conversation over a companded link, a listener is exposed to idle channel noise during pauses, "signal on" channel noise during speech, and the hush-hush effect at the end of a speech utterance. The "signal on" noise is proportional to the speech power and therefore varies as a function of the vocal effort. This noise is usually masked when the speech power level is about 20 dB higher than the noise; masking effect decreases for speech S/N ratios less than 20 dB.

The combined influence of these factors has been evaluated in subjective listening tests by varying the satellite system noise level in the companded channel and comparing it with an uncompanded (linear) satellite reference channel. In this study, system noise of −51.2 dBm0p was chosen for the reference channel, corresponding to 7500-pW0p noise allocated for INTELSAT operation of the satellite telephone link.

The following definition of compandor advantage was adopted, and all results are quantitatively expressed accordingly:

Compandor advantage is the difference in dB between the actual satellite system noise levels when using compandors and the linear reference system noise level (−51.2 dBm0p) when the speech transmission performance of both channels yields subjectively equal quality.

Measured compandor and companded channel characteristics

The compandors used in the tests were designed with the Signetics NE570 IC, which has two identical, independent circuits. Each circuit can be used either as a compressor or an expander by appropriate pin interconnections and selection of external components. The unaffected level was selected at −11 dBm0.

Figure 5 gives compressor and expander characteristics, and Figure 6 shows the compandor tracking response. Figure 7 shows the tracking error in the presence of system noise, and Figures 8–11 show the dynamic responses. The parameters characterizing this compandor, as
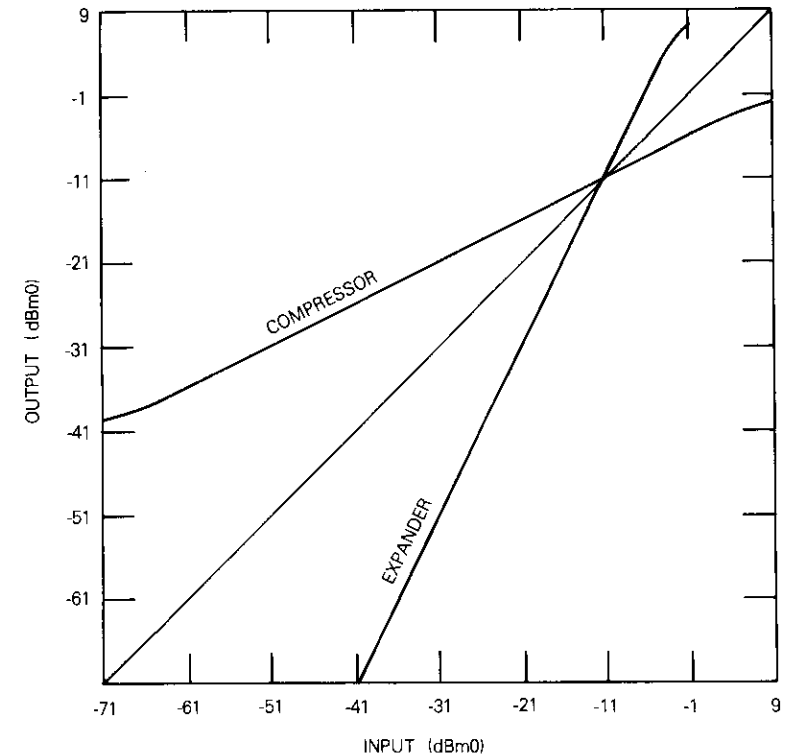
Figure 5. *Compressor and Expander Characteristics*

shown in Table 1, are well within CCITT recommendations [8]. This indicates that present IC technology may permit tighter specifications, which will be important for future applications.

Objective channel noise measurements were made at the top channel output of a simulated satellite carrier loaded with 120 channels (Appendix A). The access circuit noise was simulated by injecting noise at −60, −54, and −48 dBm0p. Figure 12 shows measurement results as a function of satellite system noise in the top baseband channel. The associated C/N ratios, shown on the abscissa, exceed normal operational values for meeting the experimental conditions required by the transmission of 120 channels in the 2.5-MHz bandwidth. Curves A show the channel noise without companding, and curves B show the idle channel output noise with companding. The improvement
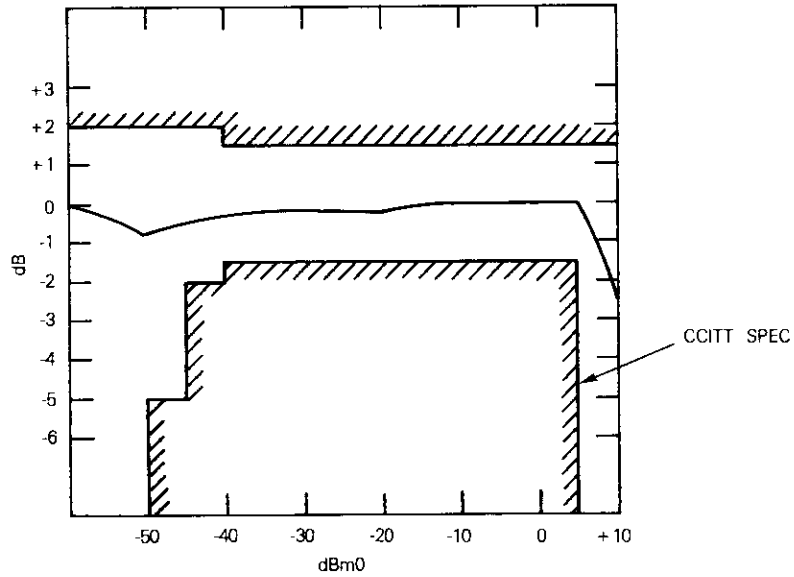
Figure 6. *Compandor Tracking Curve*
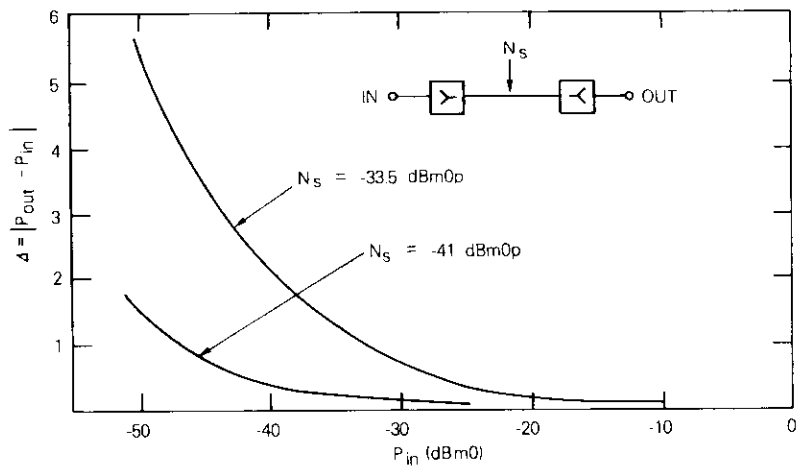
Figure 7. *Tracking Error in the Presence of System Noise*
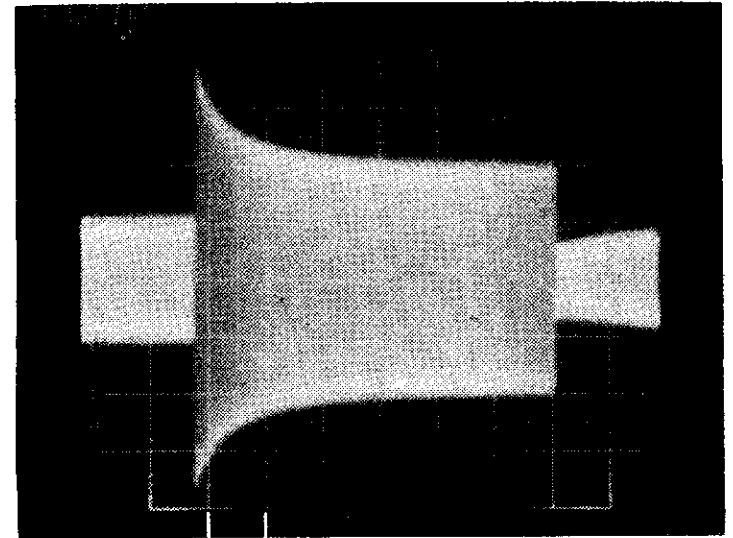
Figure 8. *Compressor Attack Response*
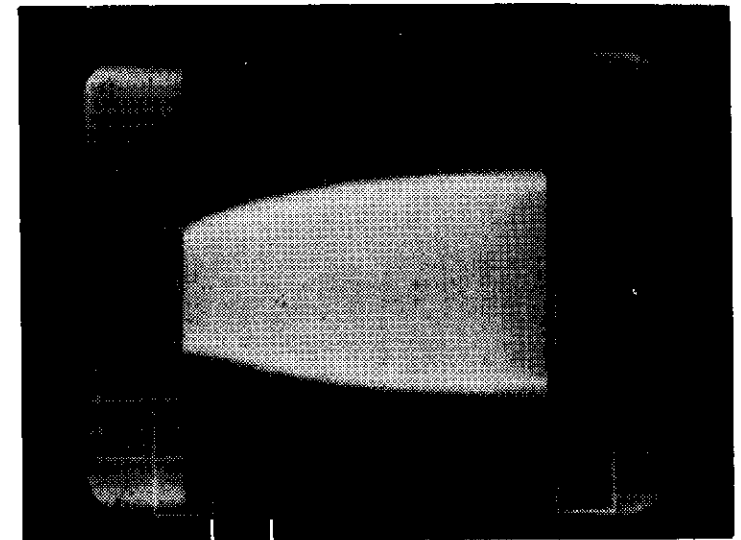
Figure 9. *Compressor Recovery Response*
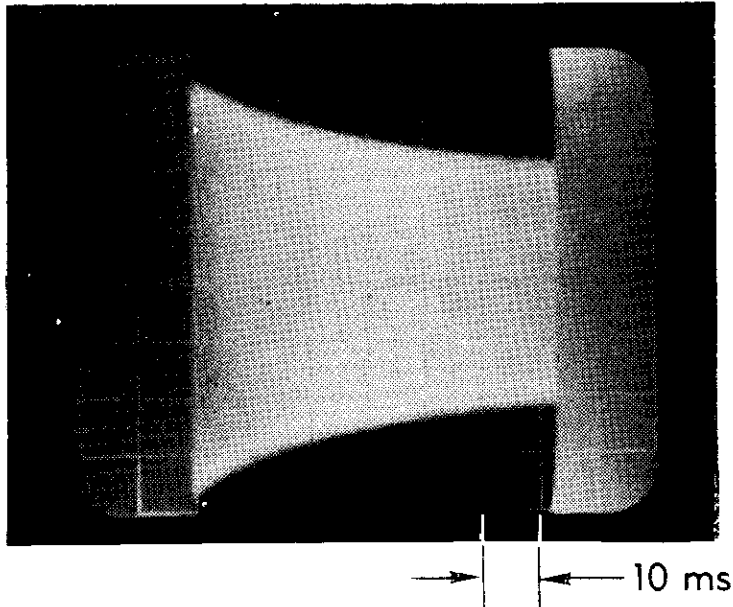
Figure 10. *Expander Attack Response*
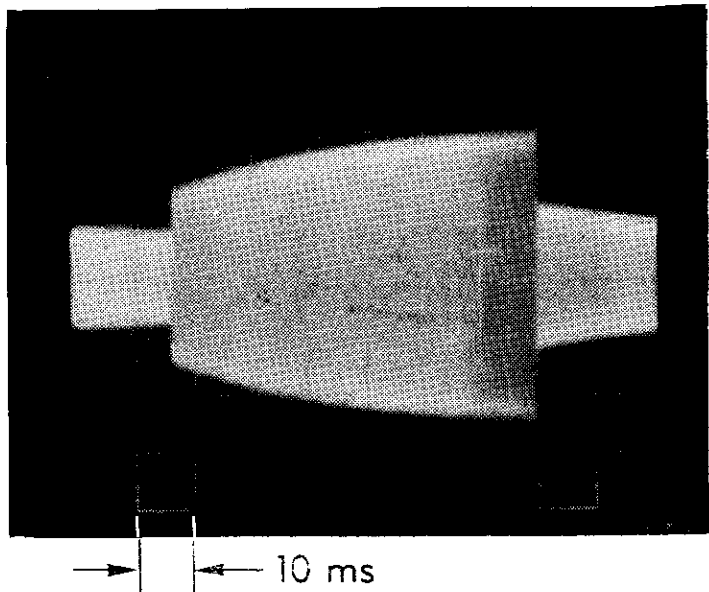
Figure 11. *Expander Recovery Response*

TABLE 1. COMPARISON OF COMPANDOR SPECIFICATION DATA

|	Used in Test (Signetics 570/571)		Specified in G.162	
Variation in Compressor Gain	±0.2		±0.5	
Variation in Expander Gain	±0.2		±0.5	
Compandor Tracking	(See Figure 6)			
Frequency Response	Comp	Exp	Comp	Exp
300–400 Hz and				
3000–3400 Hz	−0.5, +0.2	−0.7, +0.2	−1.1, +0.28	−2.2, +0.55
400–600 Hz and				
2400–3000 Hz	−0.3, +0.2	−0.2, +0.2	−0.55, +0.28	−1.1, +0.55
600–2400 Hz	−0.2, +0.2	−0.2, +0.2	−0.28, +0.28	−0.55, +0.55
Intermodulation	<40 dB		<26 dB	
Harmonic Distortion	<2 percent		<4 percent	
Transient Response Time				
Attack	3 ms		<5 ms	
Recovery	14 ms		<22.5 ms	
Back-to-Back Overshoot on 12-dB Step Change	+5, −8 percent		20 percent	

in noise level is attributed to the expander. For example, the idle channel noise advantage is about 15 dB when the access circuit noise is −54 dBm0p and the satellite system noise is −41 dBm0p.

Curves C show the "signal on" channel noise measured by transmitting a test tone of −20 dBm0 and removing it with a notch filter at the channel output. The "signal on" noise advantage is the difference between curves A and C, and is about 5 dB for the parameters of the previous example. During active periods of speech, the listener is exposed to "signal on" noise, and during pauses and intersyllabic pauses, to idle channel noise. Thus, if the "hush-hush" effect is neglected, the compandor advantage is expected to be between 5 and 15 dB, which are the "signal on" and the idle channel noise advantages, respectively.

The objectively measured values of Figure 12 agree with calculated values to within tenths of a decibel. The disagreement is larger for the

idle channel noise at the precompressor noise level of -60 dBm0, indicating a dynamic range limitation of the compressor.
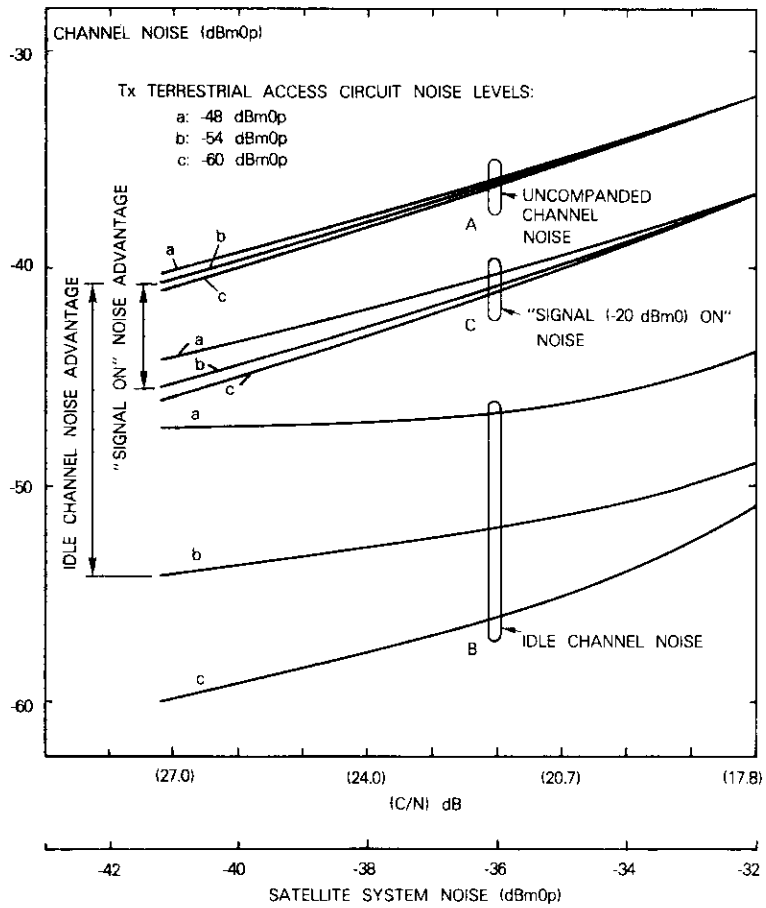

Figure 12. *Channel Noise vs Satellite System Noise*

Figure 13 shows the measured channel amplitude response and envelope delay; the differences between the companded and uncompanded channel are insignificant.
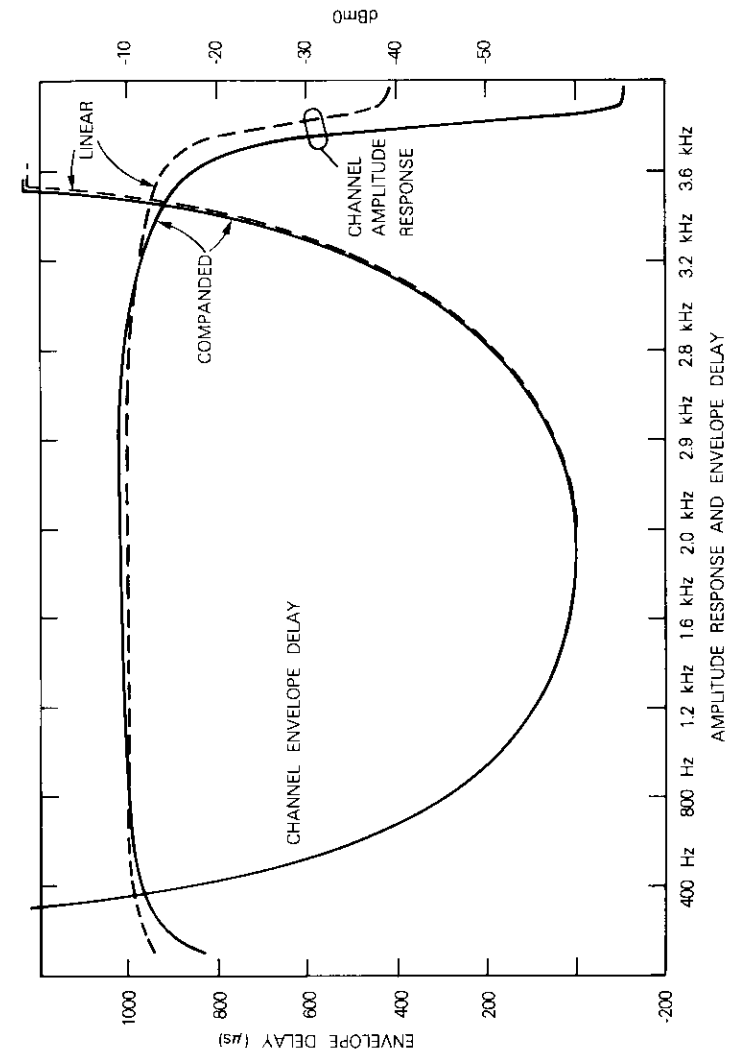
Figure 13. *Channel Amplitude Response and Envelope Delay*

Compandor advantage measurements

Compandor advantage was assessed by loading the carrier with 120 channels in the form of two supergroups (see Appendix A) occupying the 12- to 552-kHz baseband. The frequency deviation of the carrier was adjusted to be compatible with an allocated satellite bandwidth of 2.5 MHz. The C/N ratio was adjusted to yield the required top channel S/N ratio on the link, and preemphasis and deemphasis were used. The following conditions were included:

a. Noise was introduced at the input to the compressor to realistically simulate a terrestrial access circuit to the satellite link. Noise was not included on the receive terrestrial end at the output of the expander to expose possibly undesirable compandor effects and hence represents a worst-case condition.

b. As indicated by previous experiments in the presence of speech-correlated noise, subjects listening to only one side of the conversation have different opinions. Subjects concentrating on silences generally have a better opinion than those concentrating on speech. To avoid this, speech with a high activity factor was used, causing perhaps another worst-case condition.

c. The listening level was maintained constant at -29 dBm at the handset terminals by adjusting the level after the expander output. Thus, the test subjects were exposed only to S/N variations. Loudness, as a variable, was eliminated.

The reference and the unknown speech samples in the subjective test were produced from a master tape containing three phonetically balanced sentences by a male talker and a female talker. The master tape was recorded at the output of an 11,000-ft, 26-Ga subscriber loop connected to a 500-type telephone set used by the talkers.

Seven reference speech samples were recorded by replaying these six sentences at the master tape and adding band-limited random noise. The speech-to-noise ratios of the reference speech samples ranged from 15 to 33 dB in 3-dB increments. The unknown speech samples were recorded at the output of the top companded baseband channel by connecting the replayed master tape signal to the channel input at -20 dBm0 with access circuit noise levels of -48, -54, and -60 dBm0p. The C/N ratio had assigned values of 17.8, 20.7, 24, and 27 dB, yielding system noise levels of -32, -35, -38, and -41 dBm0p, respectively. The three access noise levels and the four satellite system noise levels yielded 12 speech samples (treatments) for evaluation.

Two groups of 13 treatments each were chosen; each group consisted of 6 unknown treatments and 7 reference treatments. The two groups were arrayed into two incomplete randomized block designs using a 13 × 4 format known as the Youden Square (YS) for subjective evaluation. The common set of reference conditions served as the connecting link between the two YS formats.

A total of 24 test subjects, 4 at a time, listened to the speech segments in a prescribed sequence. The speech samples were presented to the listeners over a subscriber loop and a 500-type telephone headset. The speech level at the telephone set was held constant at -29 dBm. Since the YS technique is well documented [9], further discussion will be limited to the results of the experiments.

Figure 14 shows the results in terms of channel noise vs system noise.
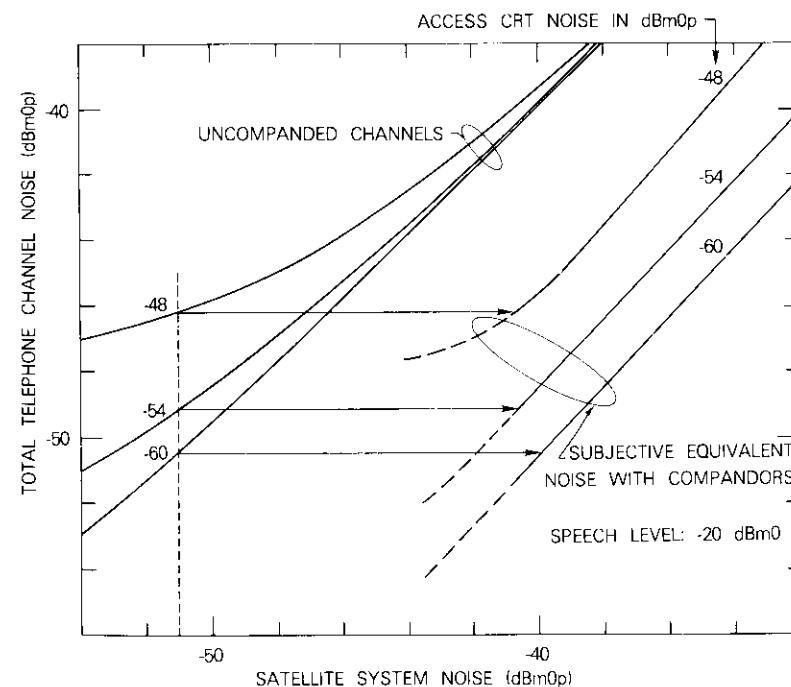
Figure 14. *Channel Noise* vs *Satellite System Noise*

noise for the speech level of -20 dBm0 with access noise as a parameter. Each companded performance curve is a least mean square approximation based on average measured values associated with the four discrete system noise levels. The standard deviation calculated from this analysis is 1.3 dB. The set of three curves on the left shows the channel noise for uncompanded channels. Similarly, the set of three curves on the right shows the subjectively perceived channel noise when compandors are used. The amount by which the companded curves shift to the right is the compandor improvement and represents the allowable increase in satellite system noise. There is a compandor advantage of 10 to 12 dB, since satellite noise of -41 to -39 dBm0p in a circuit with compandors provides performance equal to that of a -51-dBm0p satellite circuit without compandors.

Two sets of recordings were evaluated under identical conditions, but with a speech level of -16 dBm0 and then with a reduced load of 60 channels and appropriately reduced C/N ratios. These tests also resulted in a 10- to 12-dB compandor advantage. The measured results revealed the following:

    a. The compandor advantage is only slightly dependent on the speech level and the access circuit noise level.

    b. The 9-dB compandor advantage assumed for the compandor with a -11-dBm0 unaffected level used in later calculations is conservative.

    c. The subjective compandor advantage is between the idle channel noise advantage and the "signal on" noise advantage.

    d. The subjective compandor advantage can be roughly estimated by subtracting a constant of 5 to 6 dB [10] from the idle channel noise advantage to account for the subjective effects.

Multichannel load measurements

The instantaneous voltage of the baseband FDM multichannel signal is a statistical variable described by its distribution function. The FM modem used for transmission must be adjusted to ensure adequate FM improvement with an appropriate low probability of overload. For the uncompanded multichannel load, CCITT Rec. G.223 [11] specifies average and peak loads based on the classical work of Holbrook and Dixon [12]. A mathematically consistent solution for the same problem was recently published by deBoer-Hooijkamp [13], [14]. The results of these two approaches will be compared with measurements of both

uncompressed and compressed multichannel signals for various numbers of channels, n.

The long-term mean power, P_{av}, of n uncompanded telephone channels [10] is given by

$$P_{av} = P_t + 0.115\sigma^2 + 10\log\tau_L + 10\log n \quad (\text{dBm0}) \tag{8}$$

where P_t is the mean active speech level for the talker population with a normal distribution of $N(P_t, \sigma^2)$ and with τ_L representing a composite activity factor. Use of the well-established values [11] of $\sigma = 5.8$ dB, $\tau_L = 0.25$, and the per-channel load of $P_{av(1)} = -15$ dBm0 results in the value of -12.8 dBm0 for P_t. Thus, equation (8) can be expressed as

$$P_{av} = -15 + 10\log n \quad (\text{dBm0}) \quad . \tag{8a}$$

The long-term mean power, P'_{av}, of n compressed speech channels is given by replacing P_t with $(P_t + U)/2$ and σ^2 with $(\sigma/2)^2$ in equation (8):

$$P'_{av} = \frac{P_t + U}{2} + 0.115\left(\frac{\sigma}{2}\right)^2 + 10\log\tau_L + \log n \quad (\text{dBm0}) \quad . \tag{9}$$

Substituting the numerical parameters into equation (9) yields

$$P'_{av} = -11.47 + \frac{U}{2} + 10\log n \quad (\text{dBm0}) \quad . \tag{9a}$$

Using a compandor unaffected level of -11 dBm0 in equation (9a) results in a 2-dB decrease in P'_{av} compared to the P_{av} value given by equation (8a).

The peak load, P_{eq}, of n multiplexed telephone channels is expressed as the power of a sinusoidal signal whose amplitude is equal to the peak voltage of the multiplex signal [11]. The peak voltage is defined as the voltage exceeded with probability ε. The peak load of uncompanded channels without channel limiters [11], based on the work of Holbrook and Dixon [12], is shown in curve *A* in Figure 15. The ε value associated with this curve, as shown in Reference 13, is between 10^{-4} and 10^{-5}. The peak load with channel limiters hard limiting at $+10$ dBm0 is shown as curve *B* in Figure 15 for $\varepsilon = 10^{-5}$ [14]. For
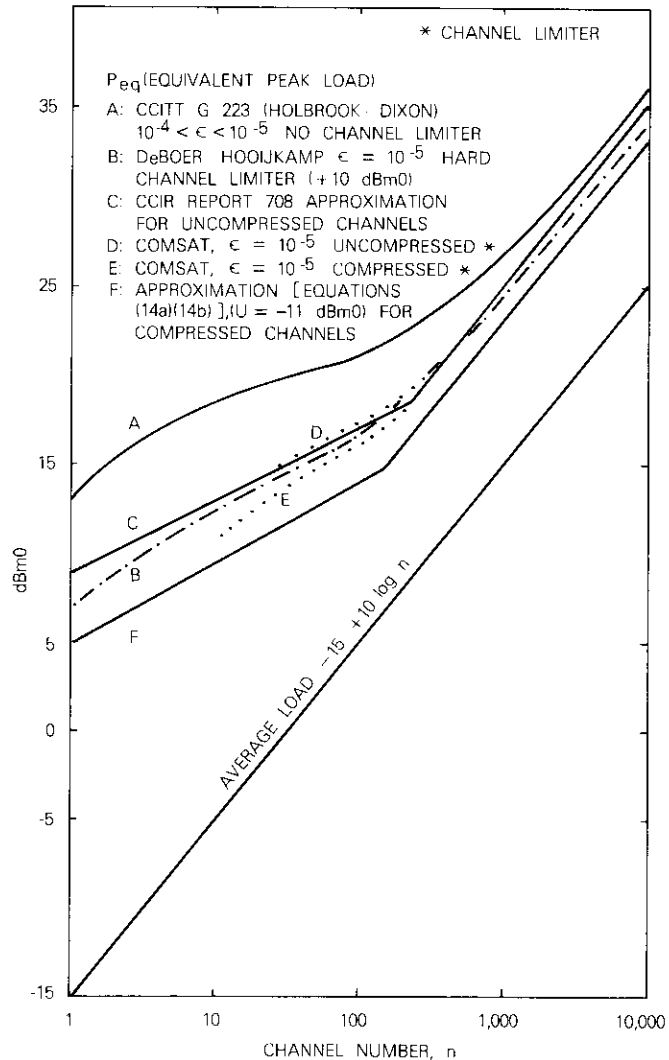
Figure 15. *Multichannel Equivalent Peak Load*

FDM-FM calculations, curve C of Figure 15 [15] is generally used. This curve is given by

$$P_{eq} = P_{av} + 10 = (-15 + 10 \log n) + 10 \quad (dBm0), \qquad n \geq 240 \quad (10a)$$

$$P_{eq} = (-1 + 4 \log n) + 10 \quad (dBm0), \qquad n < 240 \quad . \quad (10b)$$

Curves A, B, and C are parallel to the associated long-term average curve for channel numbers $n \gtrsim 200$. This is also evidenced by equation (10a), which shows a 10-dB difference between P_{eq} and the long-term average load, equation (8a), corresponding to a 13-dB (peak of the sinusoid) peak-to-average value. The law of large numbers ensures that, regardless of the form of the individual instantaneous speech voltage distribution, n multiplexed voice channels will begin to assume the characteristics of a Gaussian signal for large n. The peak-to-average ratio in that case approaches 13 dB (probability ε of exceeding the peak $= 10^{-5}$).

For values of n approaching 1, the signal exhibits increasing peakedness; using equations (10a) and (10b), this is given by

$$P_{eq}(n < 240) - P_{eq}(n \geq 240) = 14 - 6 \log n \quad . \quad (11)$$

The distribution of both compressed and uncompressed speech signals was measured for a single channel and for FDM composites of 12, 24, and 60 channels. The MUX transmit channel has an amplitude-limiting characteristic as shown in Figure 16. The composite signals
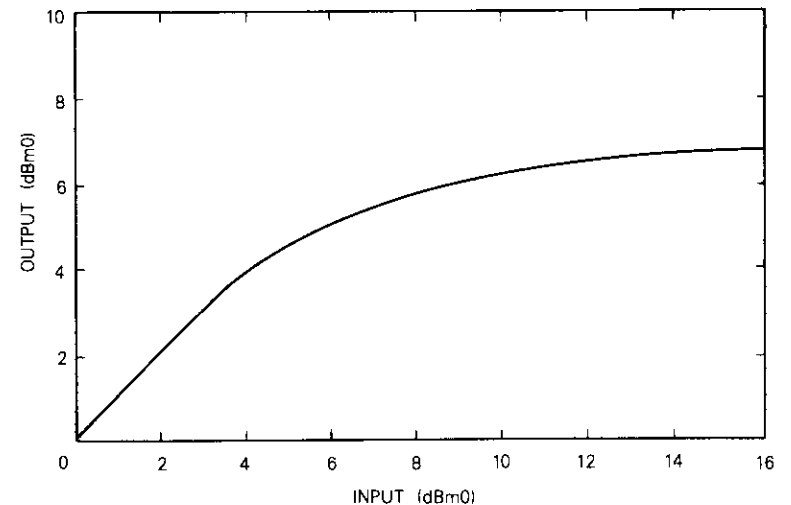

Figure 16. *MUX Transmit Channel Limiter Characteristics*

were derived from random samples of speech sources representing a Gaussian speech volume distribution $N(P_t = -15$ dBm0, $\sigma = 6$ dB) with 40-percent ensemble speech activity. The speech levels and activity were measured with a BPO* 5B speech voltmeter [16].

With the given parameters and equation (8), the long-term mean power of the companded channels in the test is given by

$$P_{av}(\text{test}) = -14.84 + 10 \log n \quad (\text{dBm0}) \quad . \tag{12}$$

Using a compandor with $U = -11$ dBm0 and equation (9) yields the long-term mean power of the compressed channels:

$$P'_{av}(\text{test}) = -15.94 + 10 \log n \quad (\text{dBm0}) \quad . \tag{13}$$

The distributions were measured with a special digitally implemented amplitude distribution meter. The amplitude distribution was determined as a histogram with amplitude range (x) divided into 16 equal intervals. Each interval was associated with a counter which determined the number of digitized samples occurring in a 16.6-minute interval. Figures 17–20 show the resulting cumulative frequency distributions of $|x|$ and, for comparison, the Gaussian distribution of $|x|$ referred to as a "half-normal" distribution. When the channel number increases, the measured distributions more closely approach the "half-normal" distribution. As a measure of approximation, the vertical distances Δ and Δ' were chosen at the 50-percent point of the "half-normal" distribution.

Based on the peak (defined at 10^{-5} probability) to rms values from the multichannel measurements, the uncompressed curve D of Figure 15 is obtained using extrapolation. Similarly, curve E is obtained by shifting the difference between equations (12) and (13) by 1 dB to reveal the differences between curves D and E on the same scale. This demonstrates that the compressed curve E is less peaked than the uncompressed curve D for lower channel numbers.

Simple load expressions for CFDM-FM calculations similar to equations (10a) and (10b) can be derived for use in FDM-FM calculations. First, the convergence of the measured cumulative peak-to-rms distributions with the "half-normal" distributions shown in Figure 21 should be examined. The abscissa scaling is given as the number of continuous talkers, which is obtained by multiplying the channel number by the activity factor of $\tau_L = 0.4$. Figure 21 shows that the

---

* Presently called British Telecom.
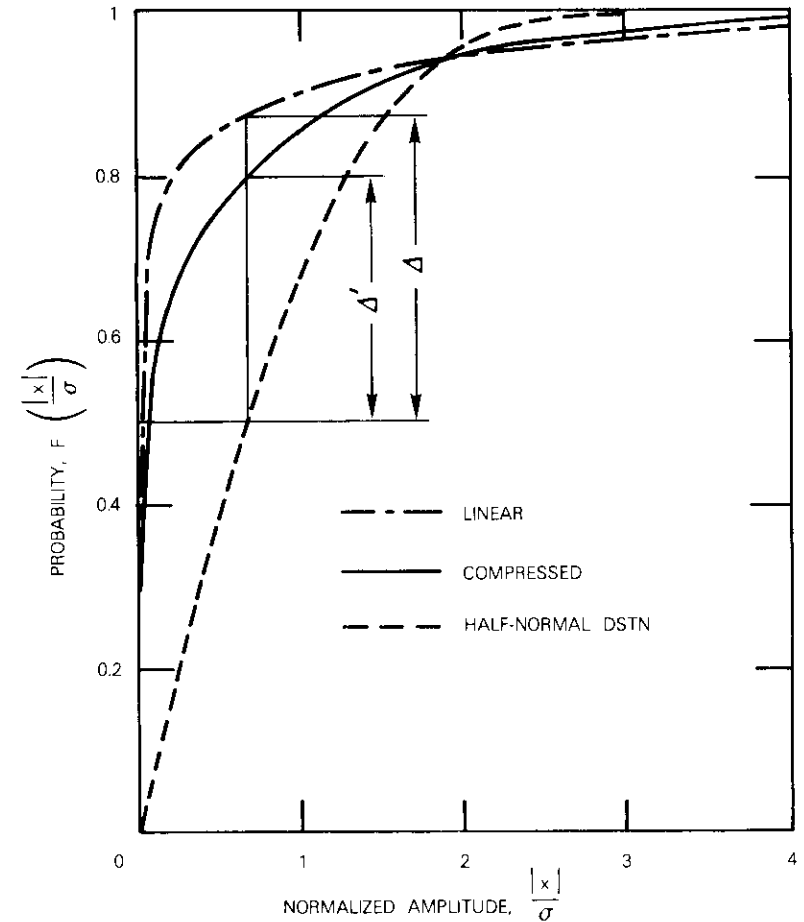
Figure 17. *Single-Channel Amplitude Distribution*

normal distribution can be used instead of the normalized uncompressed and compressed distributions, when the number of continuous talkers equals or exceeds about 60 and 40, respectively. With the generally used activity factor of $\tau_L = 0.25$, 60 continuous talkers correspond to $n = 240$ uncompressed channels, the limiting value for equation (10a). Similarly, for compressed channel numbers, $n = 160$ corresponds to 40 continuous talkers. The equivalent compressed multichannel load is given as
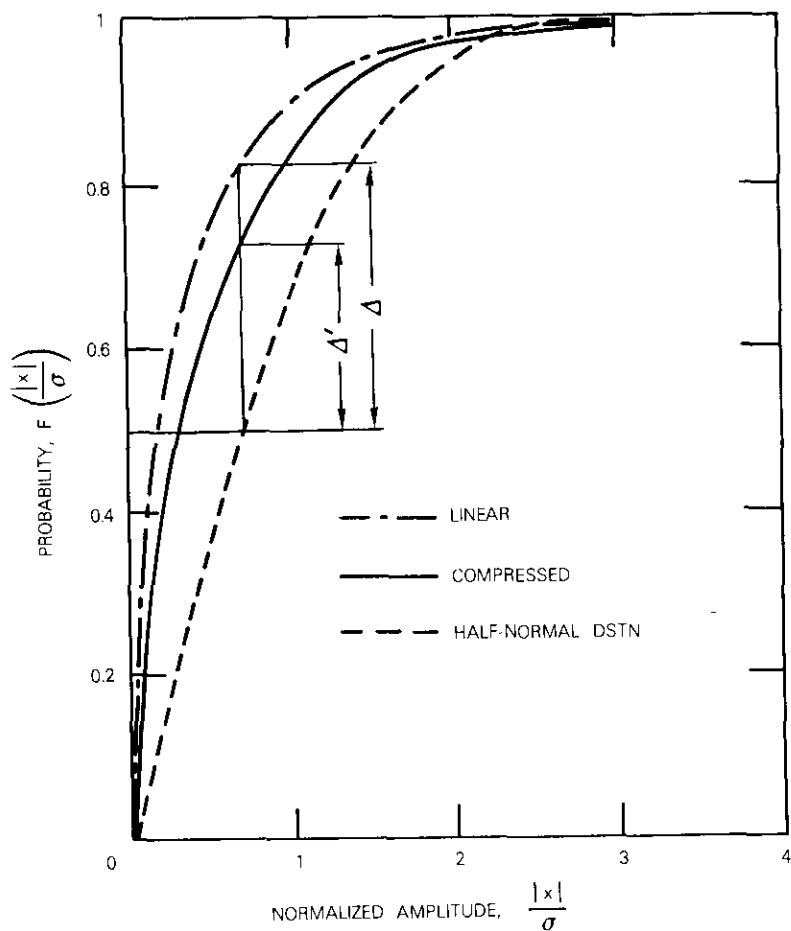
Figure 18. *12-Channel Amplitude Distribution*

$$P'_{eq} = P'_{av} + 10 = -11.47 + \frac{U}{2} + 10 \log n$$
$$+ 10 \quad (\text{dBm0}), \qquad n \geqq 160 \quad . \qquad (14a)$$

A linear approximation of P'_{eq} for $n < 160$ is

$$P'_{eq} = 0.42 + \frac{U}{2} + 4.6 \log n + 10 \quad (\text{dBm0}), \qquad n < 160 \quad . \qquad (14b)$$
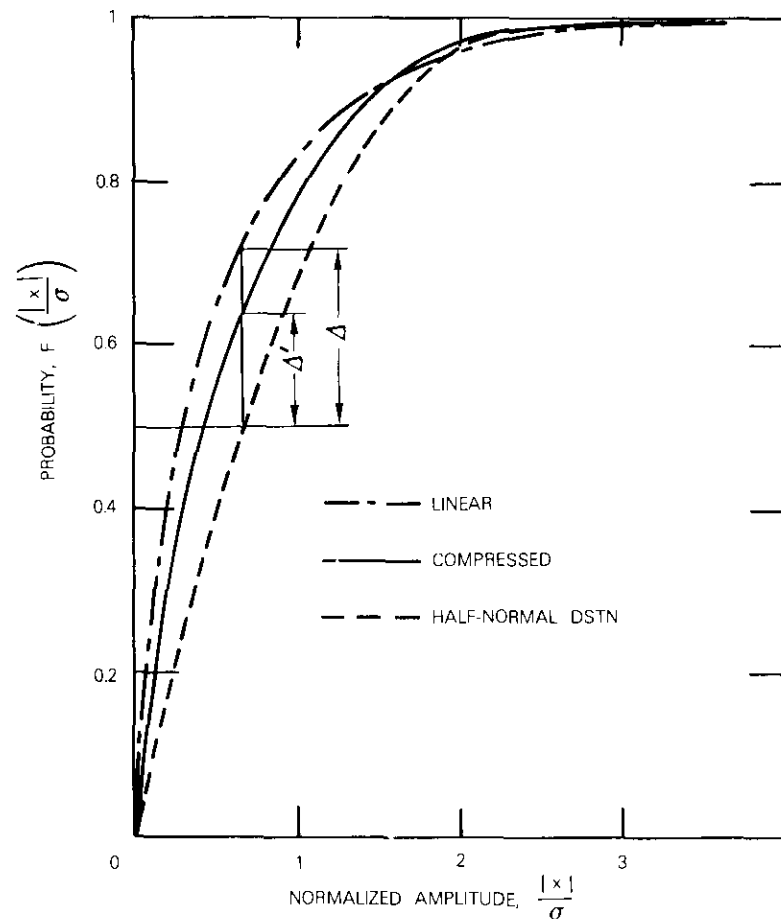
Figure 19. *24-Channel Amplitude Distribution*

The increasing peakedness for lower channel numbers is expressed as

$$P'_{eq}(n < 160) - P'_{eq}(n \geqq 160) = 11.05 - 5.4 \log n \quad . \qquad (15)$$

Equation (14b) is determined by fulfilling two conditions:

a. The lines given by equations (14a) and (14b) should intersect at $n = 160$.
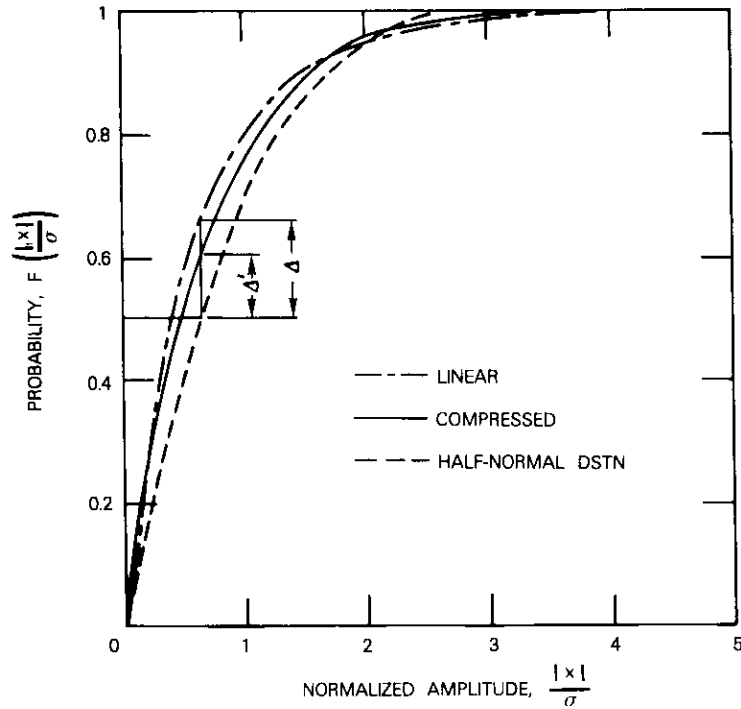
Figure 20. *60-Channel Amplitude Distribution*

b. The peakedness of the compressed load given by equation (15) should be about 2.5 dB less at channel number 12 (as shown in curves *E* and *F* of Figure 15) than that of the uncompressed load given by equation (11).

Equations (14a) and (14b) are based on the same P_t, τ_L, and σ parameters as equations (10a) and (10b). The P_{eq} curve *F* of Figure 15 is given by equations (14a) and (14b) for $U = -11$ dBm0.

It is of interest to compare the baseband and the IF frequency spectrum of the multiplexed signal consisting of a 120-compressed-channel load and that of the noise load (see Figures 22 and 23). The more spiked frequency spectrum of the multichannel load as compared to the noise load can be explained by the 4-kHz periodicity in the spectrum of the FDM baseband signal.
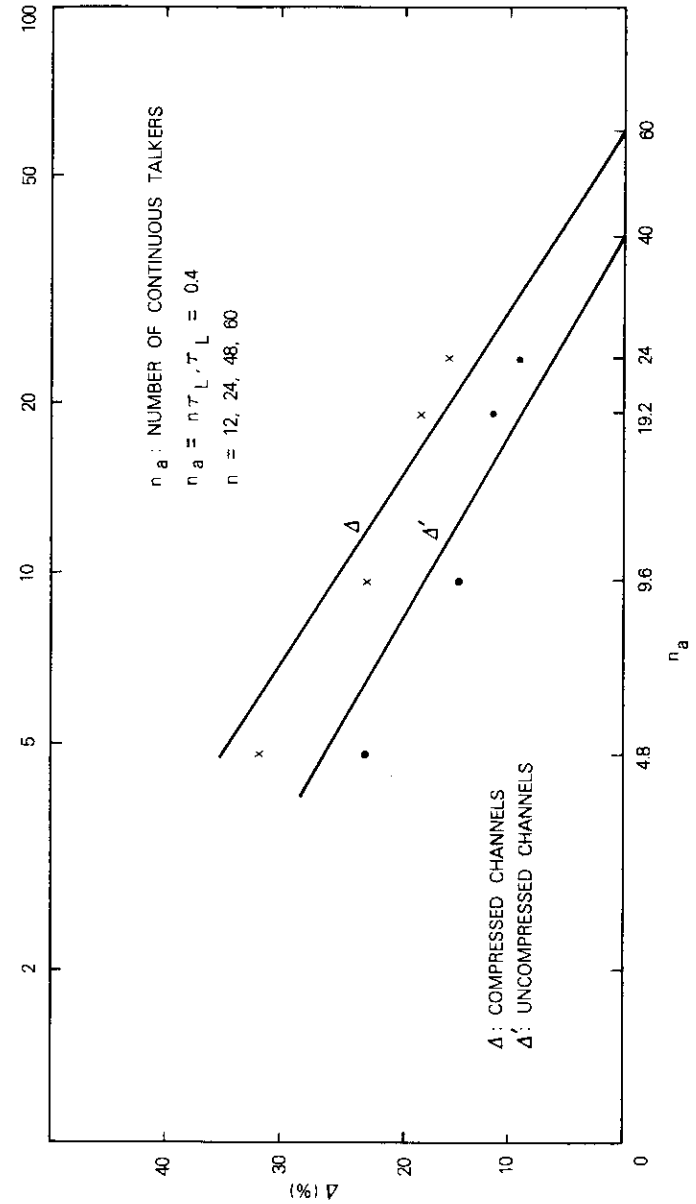
Figure 21. *Convergence to the Half-Normal Distribution*
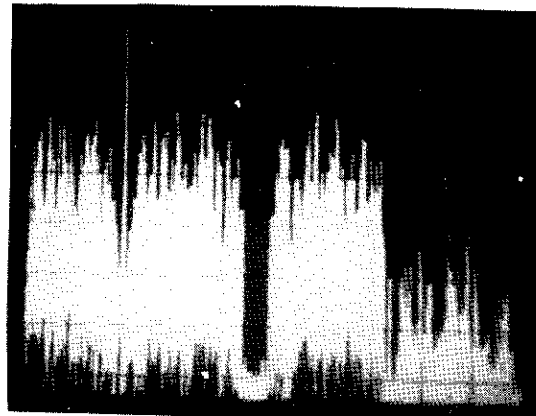
a. SPEECH LOAD

|12-252| |312-552|
  KHz   KHz
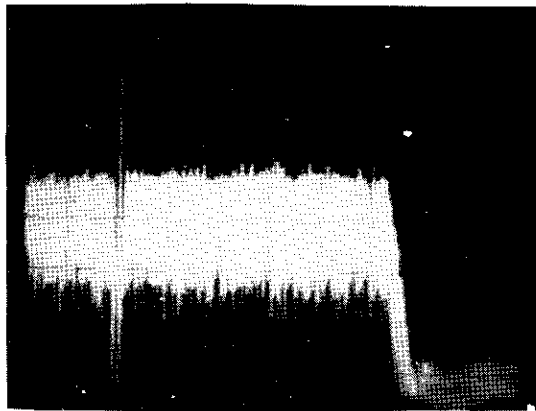
b. NOISE LOAD

SCALE UNITS. VERTICAL: 10 dB, HORIZONTAL: 0.1 MHz

SPECTRUM ANALYZER FILTER BW: 0.3 KHz

Figure 22. *Baseband Frequency Spectrum of Multichannel Load and Noise*

Communications capacity

The communications capacity (*i.e.*, number of voice channels) in the FDM-FM transmission mode is taken as a reference. Then, for the
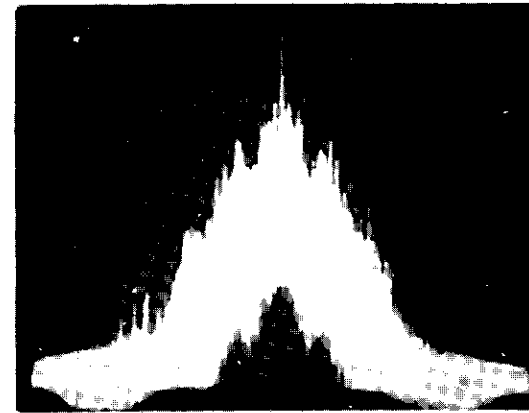
a. SPEECH LOAD
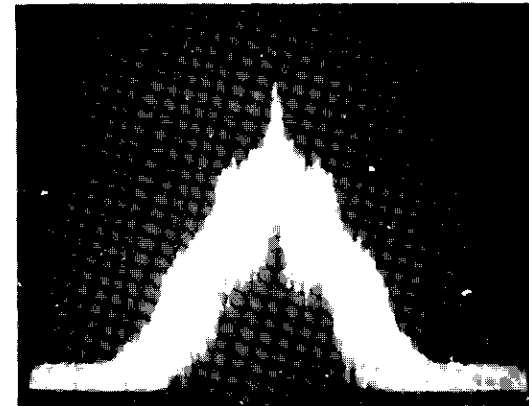
b. NOISE LOAD

SCALE UNITS: VERTICAL: 10 dB, HORIZONTAL: 0.5 MHz

SPECTRUM ANALYZER FILTER BW: 1 KHz

Figure 23. *IF Frequency Spectrum of Multichannel Load and Noise*

CFDM-FM transmission mode, the necessary condition for channel capacity to be independent of the unaffected level is given and the channel capacity is calculated. Finally, based on conservative assumptions, the CFMD-FM channel capacity is shown.

FDM-FM carrier channel capacity

The FM equation for FDM-FM operation above threshold is frequently expressed [15] in the following form:

$$\frac{TT}{N_s} = \frac{C}{N}\frac{B}{b}\left(\frac{f_r}{f_m}\right)^2 PW \qquad (16a)$$

$$B = 2\left[\log^{-1}\left(\frac{P_{eq}}{20}\right)f_r + f_m\right] \quad \text{(Carson's Rule bandwidth)} \quad (16b)$$

where

TT/N_s = test done to weighted noise ratio in the top baseband telephone channel = 1.318×10^5 (51.2 dB) for 7,500-pW0p system noise and 0-dBm0 test tone

C/N = carrier-to-noise ratio in bandwidth B

f_r = rms test tone deviation

b = telephone channel bandwidth = 3 kHz

f_m = maximum baseband frequency = $12 + 4 \times n$ kHz ~ 4.2 kHz × n (12 kHz in the low end of the frequency band is utilized for order wires; 4 kHz is the telephone channel spacing)

n = number of telephone channels

P = psophometric weighting factor, $10 \log P = 2.5$ dB

W = preemphasis weighting factor, $10 \log W = 4$ dB

P_{eq} = given by equations (10a) and (10b).

When f_r from equation (16a) is substituted into equation (16b) and $z^2 = B/n$ is introduced, the following equations are obtained where B/N is the occupied FM bandwidth per telephone channel:

$$z^3 - 8.4z - 6,933n^{-0.3}\left(\frac{C}{N}\right)^{-0.5} = 0 \quad , \qquad n < 240 \qquad (17a)$$

$$z^3 - 8.4z - 1,395\left(\frac{C}{N}\right)^{-0.5} = 0 \quad , \qquad n \geqq 240 \quad . \qquad (17b)$$

These equations relate $z = \sqrt{B/n}$ and C/N for $TT/N = 1.318 \times 10^5$, which is required for satisfactory link performance.

Figure 24 shows B/n, calculated from equations (17a) and (17b), as
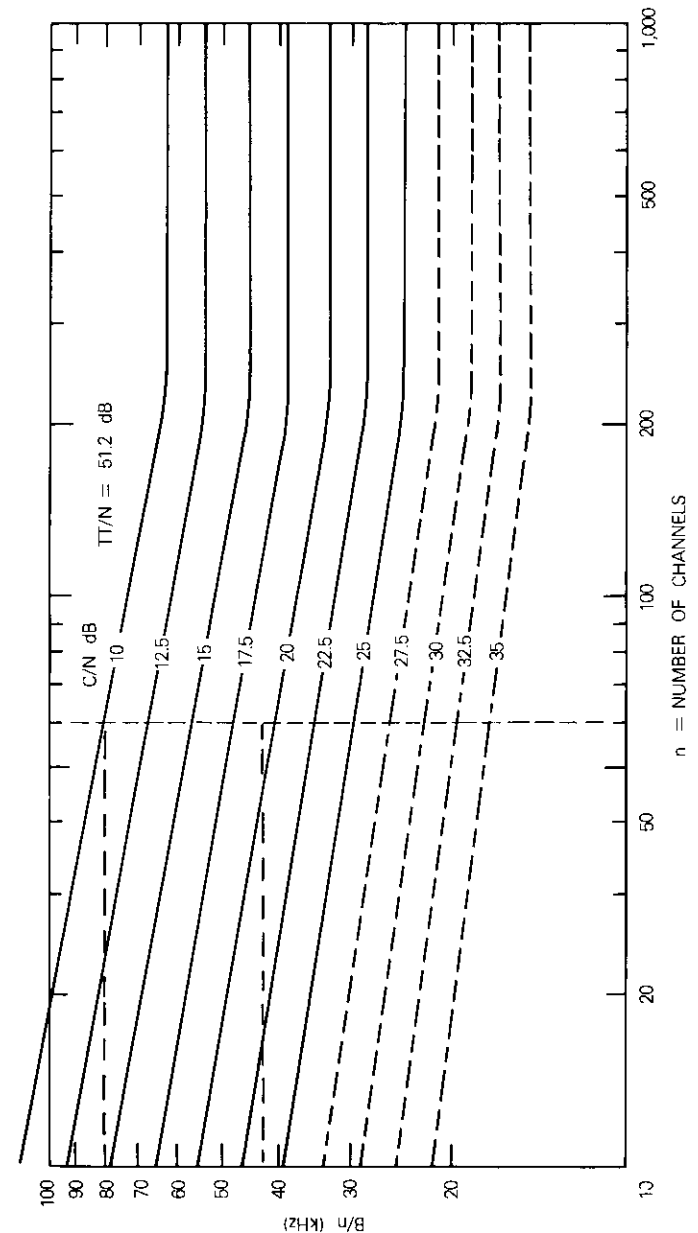
Figure 24. Occupied Bandwidth per Uncompanded Channel

a function of channel numbers at $TT/N = 51.2$ dB and with C/N as a parameter. The occupied bandwidth is obtained by multiplying B/n by the number of channels, n. For a given number of channels, the interception of a vertical line with the B/n curves indicates the influence of C/N on the occupied bandwidth. For approximate B/n calculations, Figure 25 can also be used.

	$a =$
UNCOMP	$6{,}993n^{-0.3}(C/N)^{-0.5}, n < 240$
	$1{,}395\ (C/N)^{-0.5}, n \geq 240$
COMP	$1{,}393\ n^{-0.27}(C/N)^{-0.5}, n < 160$
	$354\ (C/N)^{-0.5}, n \geq 160$

$a = z^3 - 8.4\ z$

B/n (kHz) $= z^2$
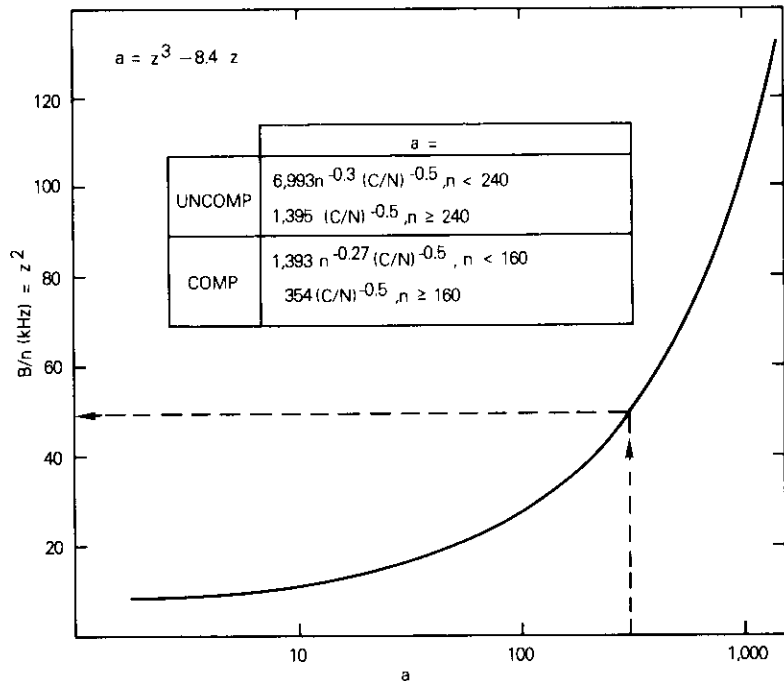
Figure 25. *Graphical Solution of the FM Equation*

CFDM-FM carrier channel capacity

For CFDM-FM calculations, equations (16a) and (16b) must be modified. In equation (16a), because of the compandor advantage A_c, a reduced test-tone-to-noise (TT/N'_s) ratio must be used:

$$\frac{TT}{N'_s} = \frac{TT}{N_s}\ 10^{-(A_c/10)} \qquad (18)$$

In equation (16b), the equivalent peak load of uncompressed P_{eq} is replaced by P'_{eq}, the equivalent peak load of compressed channels given by equations (14a) and (14b). Note that the test tone for TT/N'_s measurements and for adjusting the frequency deviation, f_r, has a level of 0 dBm0. This means that, with the compandor in the channel, the test tone level at the compressor input must be adjusted to $-U/2$ dBm0 to result in a post-compressor level of 0 dBm0. It is, therefore, important to note that the unaffected level cannot be selected arbitrarily, since it affects system loading [7].

If loading posed no restrictions, it would be advantageous to select the highest practicable value of U because compandor advantage increases with U. This increase in compandor advantage would permit higher system noise, thus permitting less FM bandwidth. However, an increased value of U would also increase system load, requiring more FM bandwidth. The necessary condition for total compensation of these opposing effects leads to a unique value of the unaffected level for an FM system with a given equivalent performance obtained by compandor advantage. Assume a general linear relationship between A_c and U:

$$A_c = \beta + \gamma U \quad (\text{dB}) \qquad (19)$$

where β and γ are constants.

Using equations (19), (18), and (16a), the FM equation for CFDM-FM operation can be written as

$$\frac{TT}{N_s}\ 10^{-[(\beta + \gamma U)/10]} = \frac{C}{N}\frac{B}{b}\left(\frac{f_r}{f_m}\right)^2 PW \quad . \qquad (20a)$$

The Carson's rule bandwidth is given by

$$B = 2\left[\log^{-1}\left(\frac{P'_{eq}}{20}\right)f_r + f_m\right] \quad . \qquad (20b)$$

In equation (20b), P'_{eq} is given by equations (14a) and (14b). Substituting f_r from equation (20a) into equation (20b) for $n \geq 160$ yields

$$B = 2f_m\left\{10^{[-1.47-(U/2)+10\log n]/20}\ 10^{-(\beta+\gamma U)/20}\right.$$
$$\left.\cdot\left(\frac{TT}{N_s}\right)^{0.5}\left(\frac{C}{N}\right)^{-0.5}\left(\frac{b}{BPW}\right)^{0.5} + 1\right\} \quad . \qquad (21a)$$

By combining n, β, (TT/N_s), (C/N), b, P, and W in a constant A, equation (21a) can be rewritten as

$$B = 2f_m\{AB^{-0.5}\,10^{[U/(0.5-\gamma)]/20} + 1\} \quad . \tag{21b}$$

Equation (21b) evidences that B is independent of U only when γ = ½, the inverse of the compression ratio, as expected.

Substituting B of equation (20a) into equation (20b) yields an expression which contains the product $P_r = f_r \cdot 10^{U/40}$. This gives another physical interpretation for the independence of B from U; if the value of U at the interface is low, f_r must be increased. The increase in f_r is obtained by an appropriate gain increase before the FM modulator and a decrease after the FM demodulator. This amounts to a centralized control of the value of U for all compandors to match the required system unaffected level. Thus, a particular subjective TT/N_s requirement determines a given bandwidth and an associated unique system unaffected level.

The capacity in the CFDM-FM transmission mode is calculated with the assumption given by equation (19), but with γ = ½, yielding A_c = 10 dB for the compander with $U = -11$ dBm0:

$$A_c = 15.5 + \tfrac{1}{2}U\,(\text{dB}) \quad . \tag{22}$$

Using equations (22) and (20a), and substituting f_r into equation (20b) yields

$$z^3 - 8.4z - 354\left(\frac{C}{N}\right)^{-0.5} = 0 \quad , \qquad n \geq 160 \tag{23a}$$

$$z^3 - 8.4z - 1{,}393\;n^{-0.27}\left(\frac{C}{N}\right)^{-0.5} = 0 \quad , \qquad n < 160 \tag{23b}$$

with $z = (B/n)^{0.5}$ as the unknown.

From equations (23a) and (23b), with the accuracy of the solution of Figure 25, the per-channel occupied bandwidth is shown in Figure 26 for C/N = 12.5 and 25 dB. The communications capacity enhancement of the CFDM-FM transmission mode, related to the FDM-FM transmission mode based on Figures 24 and 26, is shown in Figure 27.
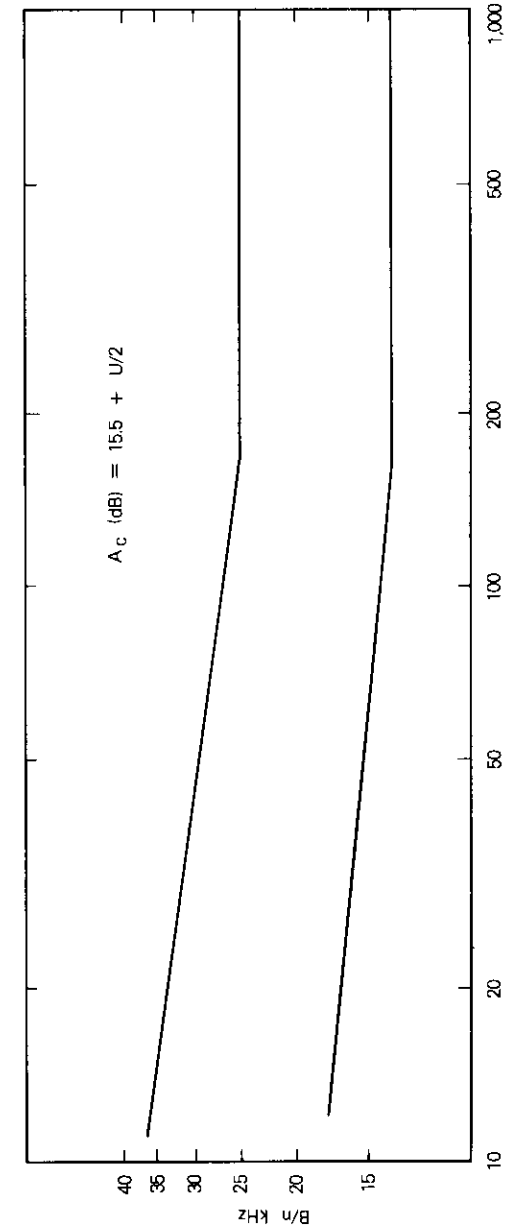
Figure 26. Occupied Bandwidth per Companded Channel
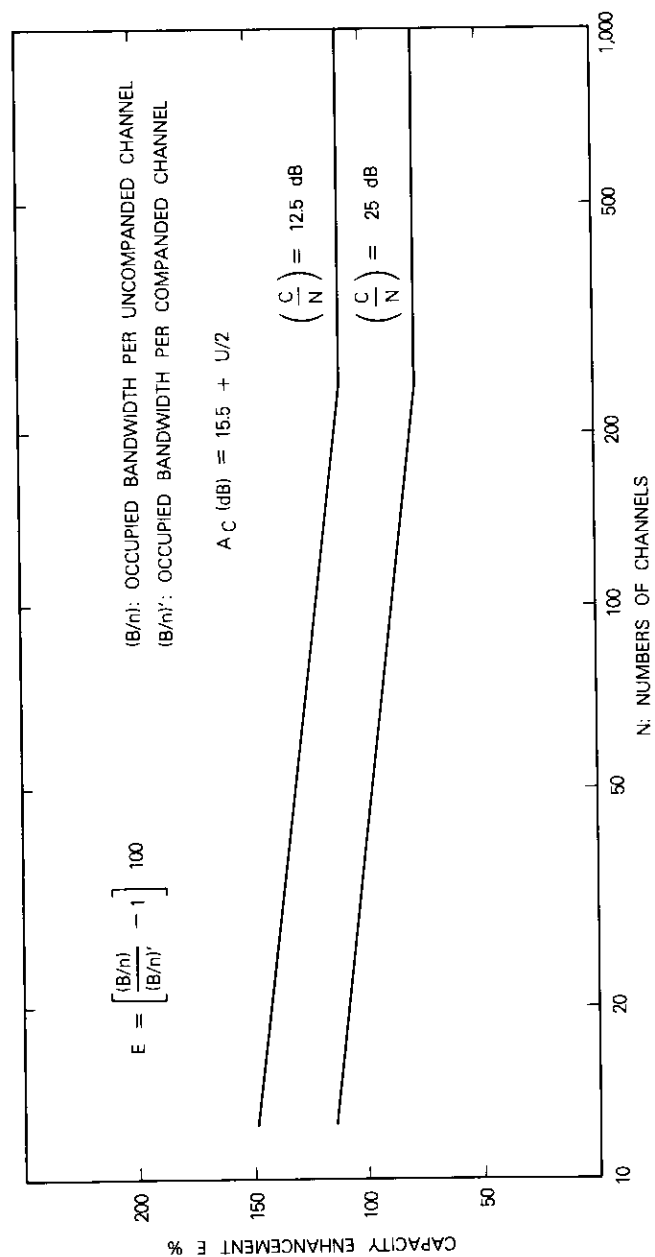
Figure 27. *Channel Capacity Enhancement*

CFDM-FM carrier communications capacity with conservative assumptions

Telephone channels are also used for transmission of non-speech signals, such as in-band signaling and data. For this type of signal, the S/N ratio, as will be shown, generally degrades in the CFDM-FM transmission mode. If the degradation is excessive, A_c values lower than those obtained from subjective tests must be used. Furthermore, the increased use of data transmission causes an increase in per-channel loading which must be taken into account.

In the following, two simplifying assumptions are made. First, the compandor advantage, A_c, with $U = -11$ dBm0 is assumed to be 9 dB, and second, $P'_{eq} = P_{eq}$. This A_c value is 1 dB more conservative than the value of approximately 10 dB used previously. The second assumption related to the equivalent peak load means that, instead of curve F of Figure 15, curve C for FDM-FM calculation must be used. Since in FM the TT/N and C/N ratios change dB for dB, the occupied bandwidth per companded channel can be found from the curves of Figure 24 (B/n for uncompressed channels) by substituting 9 dB (corresponding to A_c) for the C/N values shown. For example, for $n = 60$, and a C/N ratio of 10 dB, B/n is about 80 kHz for uncompanded channels. Interpolating $C/N = 19$ dB ($10 = 19 - 9$) results in a companded B/n of about 45 kHz. Thus, in this particular example, a capacity enhancement of almost 100 percent exists.

In INTELSAT operation, the number of channels and the allocated satellite bandwidth have selected values. Therefore, Table 2 is a more convenient form for showing the satellite capacity enhancement for different carrier sizes. For comparison, Table 3 shows the transmission parameters for regular FDM-FM carriers for INTELSAT IV-A and V. The following cases are examples:

  a. For a satellite bandwidth of 2.5 MHz and a C/N value of 13.5 dB, 60-channel loading is possible. Table 3 compares this loading with 24-channel loading in the same bandwidth at the comparable C/N value of 12.7 dB. It may thus be concluded that better than 2:1 channel capacity enhancement is possible.

  b. For a 10-MHz satellite bandwidth and a 14.5-dB C/N, 312-channel loading is possible. This value, compared to 192-channel loading at a 14.7-dB C/N value according to Table 3, represents a capacity enhancement of 1.63.

To obtain an average channel capacity enhancement factor, it can be assumed that compandors are inserted into the voice channels of

TABLE 2. CFDM-FM OPERATION (9-dB ADVANTAGE)

No. of Channels	Top Baseband Frequency (kHz)	Satellite Bandwidth (MHz)	Occupied Bandwidth (MHz)	0 dBm0 Test Tone rms Deviation (kHz)	C/N (dB)	Multichannel rms Deviation (kHz)
48	204	2.5	2.1	138.5	10.8	267.7
60	252	2.5	2.1	125.0	13.5	252.6
72	300	2.5	2.1	113.2	15.85	237.3
96	408	2.5	2.1	91.5	20.38	203.2
132	552	5.0	4.3	213.6	12.53	505.6
192	804	5.0	4.3	167.0	17.93	426.0
252	1052	5.0	4.3	123.1	22.9	347.5
192	804	7.5	6.3	291.0	11.48	742.3
252	1052	7.5	6.3	235.0	15.6	663.4
312	1300	7.5	6.3	186.4	19.5	585.5
252	1052	10.0	8.3	347.3	11.04	980.4
312	1300	10.0	8.3	287.1	14.54	901.8
432	1796	10.0	8.3	201.6	20.4	745.1
432	1796	15.0	13.0	402.8	12.46	1488.7
612	2540	15.0	13.0	284.9	18.48	1253.3
612	2540	20.0	18.0	464.7	12.8	2044.2
792	3284	20.0	18.0	361.4	17.23	1808.8
972	4028	20.0	18.0	283.8	21.1	1573.4
792	3284	25.0	21.6	475.2	14.06	2378.4
972	4028	25.0	21.6	386.6	17.62	2143.3
1092	4892	25.0	21.6	318.2	21.0	1869.7

all INTELSAT FDM-FM carriers. Based on the INTELSAT status report on carriers and channel loading for February 16–22, 1979, and Table 2, an average enhancement of 70 percent was calculated (see Table 4).

Data transmission and signaling

Transmission of two types of non-speech signals was considered in the CFDM-FM operating mode: data transmission at a constant power which is increasingly used over international telephone channels; and CCITT No. 5 in-band signaling, which is frequently used in the INTELSAT network.

Data Transmission

Assuming only satellite system noise, the S/N degradation for data transmission, Δ(S/N), is as follows. In the FDM-FM operating mode with a system noise level of N_s and a data transmission level of S_D, the S/N ratio is $(S_D - N_s)$ dB. In the CFDM-FM operating mode, the system noise is increased to $N_s' = N_s + A_c$, and the signal level increases to $(S_D + U)/2$ due to the compression. This results in an (S/N)' ratio of $[(S_D + U)/2] - N_s - A_c$. The degradation is thus given by

$$\Delta\left(\frac{S}{N}\right) = \frac{S}{N} - \left(\frac{S}{N}\right)' = \frac{S_D - U}{2} + A_c \quad \text{(dB)} \quad . \tag{24}$$

Substituting A_c of equation (19) and using the value $\gamma = 1/\alpha = 0.5$ shows that equation (24) is independent of U.

In FDM-FM transmission, the data signal-to-system-noise ratio (unweighted) is 35.78 dB for $S_D = -13$ dBm0 level [17] and unweighted noise of $-51.2 + 2.5 = -48.7$ dBm0. Equation (14) shows that in the CFDM-FM transmission mode with $U = -11$ dBm0 and the conservative value of $A_c = 9$ dB used previously, the degradation, Δ(S/N) is 8 dB. However, when the CFDM-FM channel is considered part of an international end-to-end connection which includes terrestrial links with their own noise contributions, the overall degradation is less than that of the CFDM-FM channel alone. Figure 28 shows the model of the international connection, which is a modified version of Figure 2, *CCITT Orange Book*, Rec. G.103.

TABLE 3. INTELSAT IV-A AND V TRANSMISSION PARAMETERS

Carrier Capacity (no. of channels, n)	Top Baseband Frequency, f_m (kHz)	Allocated Satellite Bandwidth Unit, b_u (MHz)	Occupied Bandwidth, b_o (MHz)	Deviation (rms) for 0-dBm0 Test Tone. b_r (kHz)
12	60.0	1.25	1.125	109
24	108.0	2.5	2.00	164
36	156.0	2.5	2.25	168
48	204.0	2.5	2.25	151
60	252.0	2.5	2.25	136
60	252.0	5.0	4.0	270
72	300.0	5.0	4.5	294
96	408.0	5.0	4.5	263
132	552.0	5.0	4.4	223
96	408.0	7.5	5.9	360
132	552.0	7.5	6.75	376
192	804.0	7.5	6.4	297
132	552.0	10.0	7.5	430
192	804.0	10.0	9.0	457
252	1052.0	10.0	8.5	358
252	1052.0	15.0	12.4	557
312	1300.0	15.0	13.5	546
432	1796.0	15.0	13.0	401
432	1796.0	17.5	15.75	517
432	1796.0	20.0	18.0	616
612	2540.0	20.0	17.8	454
432	1796.0	25.0	20.7	729
792	3284.0	25.0	22.4	499
972	4028.0	36.0	36.0	802
1092	4892.0	36.0	36.0	701

(regular FDM-FM carriers)

Multichannel rms Deviation, f_{mc} (kHz)	Carrier to Total Noise Temperature Ratio (C/T) Operating (dBW/K)	C/N Ratio in Occupied Bandwidth (dB)	Ratio of Unmodulated Carrier Power to Max Carrier Power Density under Full Load Conditions (dB/4 kHz)
159	−154.7	13.4	20.0
275	−153.0	12.7	22.3
307	−150.0	15.1	22.8
292	−146.7	18.4	22.6
276	−144.0	21.1	22.4
546	−149.9	12.7	25.3
616	−149.1	13.0	25.8
584	−145.5	16.6	25.6
529	−141.4	20.7	24.2
799	−148.2	12.7	27.0
891	−145.9	14.4	27.5
758	−140.6	19.9	25.8
1020	−147.1	12.7	28.0
1167	−144.4	14.7	28.6
1009	−139.9	19.4	27.0
1627	−144.1	13.6	30.0
1716	−141.7	15.6	30.2
1479	−136.2	21.2	27.6
1919	−138.5	18.2	30.8
2276	−139.9	16.1	31.9
1996	−134.2	21.9	28.9
2688	−141.4	14.1	32.2
2494	−132.8	22.3	30.0
4417	−135.2	17.8	34.5
4118	−132.4	20.7	32.2

TABLE 4. CFDM-FM ENHANCEMENT WITH
CONSERVATIVE ASSUMPTIONS

Satellite Path	No. of FDM-FM Channels	No. of CFDM-FM Channels	Enhancement (%)
INTELSAT IV-A F4, Major Atlantic Path 1	8,796	14,480	65
INTELSAT IV-A F1, Primary Atlantic	11,028	18,984	72
INTELSAT IV-A, Indian Ocean	10,296	17,940	74
INTELSAT IV, Pacific	5,268	9,276	76
Total	35,388	60,680	71

The modifications are as follows:

   *a.* Exchange noise contributions (200 pW0p maximum per exchange) are neglected.

   b. The international connection, which is no longer than 2,000 km, is replaced by a satellite connection with -50-dBm0p and -42-dBm0p noise contributions for FDM-FM and CFDM-FM, respectively.*

   c. The S/N ratio at the receiving modem is the same as that at reference point A because of the negligible exchange and circuit noise contributions after reference point A.

   d. For S between the transmit points of the modem and the local exchange, a loss (L_1) of 0 dB with a σ of 3 dB is assumed.

At the transmitting end, the modem transmission levels were assumed to be -13 dBm0, the present standard level, and -15 dBm0, a potential standard level. In the companded case, the compandors with an unaffected level of -11 dBm0 were assumed to be in the CT3's. For the signal, losses L_1, L_3, L_4, and L_5 and for the noise contribution N_i, losses $L_{(i+1)}$ to L_7 were considered in the S/N calculation at reference

---

*In the uncompanded case, the noise level between CT3's is 10,000 pW0p (-50 dBm0p), of which the satellite link contribution is 7,500 pW0p (-51.25 dBm0p). In the companded case, the satellite link noise is increased with a 9-dB compandor advantage to -42.55 dBm0p (59,600 pW0p). Thus, the total noise is $59,600 + 2,500$ pW0p $= -42$ dBm0p.
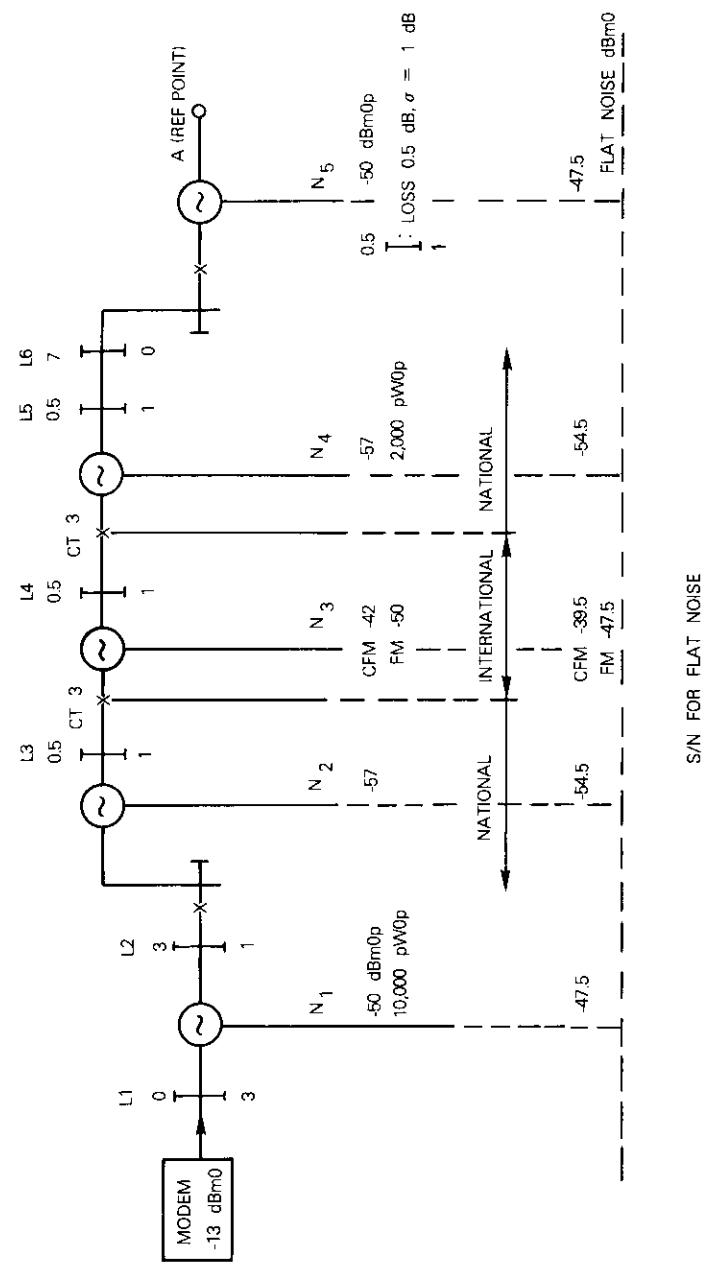
Figure 28. *Typical International Connection for Data Transmission Penalty Calculations*

point A. Loss L_6 is an artifice enabling the noise power levels to be indicated as if they were injected at zero relative level points on the individual circuit sections.

For a particular set of L_i's, the S/N ratio was calculated as follows:

a. Uncompanded Case: The signal level at reference point A is the transmit level diminished by the given losses in the transmission path. The noise level is given by the addition of noise contributions transferred to A. Each transferred noise contribution is attenuated by the losses in the direction of transfer.

b. Companded Case: The signal attenuated with losses L_1 and L_3 is compressed at the transmit CT3, attenuated with L_4, expanded at the receive CT3, and finally attenuated with L_5 to determine the signal level at reference point A. The signal increase at compression and decrease at expansion yield two additional losses, a negative and a positive loss, which are taken into account for transferring the noise contributions to reference point A.

The calculations were performed by computer for all combinations of L_i, $L_i + \sigma_i$, and $L_i - \sigma_i$ values. The output gave the individual S/N values, their mean and standard deviation, and the number of S/N values belonging to equidistant S/N intervals.

Table 5 shows the calculated means and standard deviations. The calculated distributions approximate the Gaussian distribution in their middle range. The standard deviations of the approximating normal distributions, slightly exceeding that of the calculated distributions, are also included in Table 5.

TABLE 5. CALCULATED MEANS AND STANDARD DEVIATIONS

	FDM-FM		CFDM-FM	
Signal Level (dBm0)	−13	−15	−13	−15
Mean S/N (dB)	31.85	29.85	29.82	28.18
Calculated Standard Deviation (dB)	2.72	2.72	2.34	2.43
Standard Deviation of the Approximating Normal Distribution (dB)	2.89	2.89	2.56	2.67

Based on the mean S/N ratios and on the standard deviations of the approximating normal distributions, the probability of not fulfilling the requirements of S/N = 24, 25, and 26 dB was calculated. Figure 29 shows the curves based on the calculated probability values.
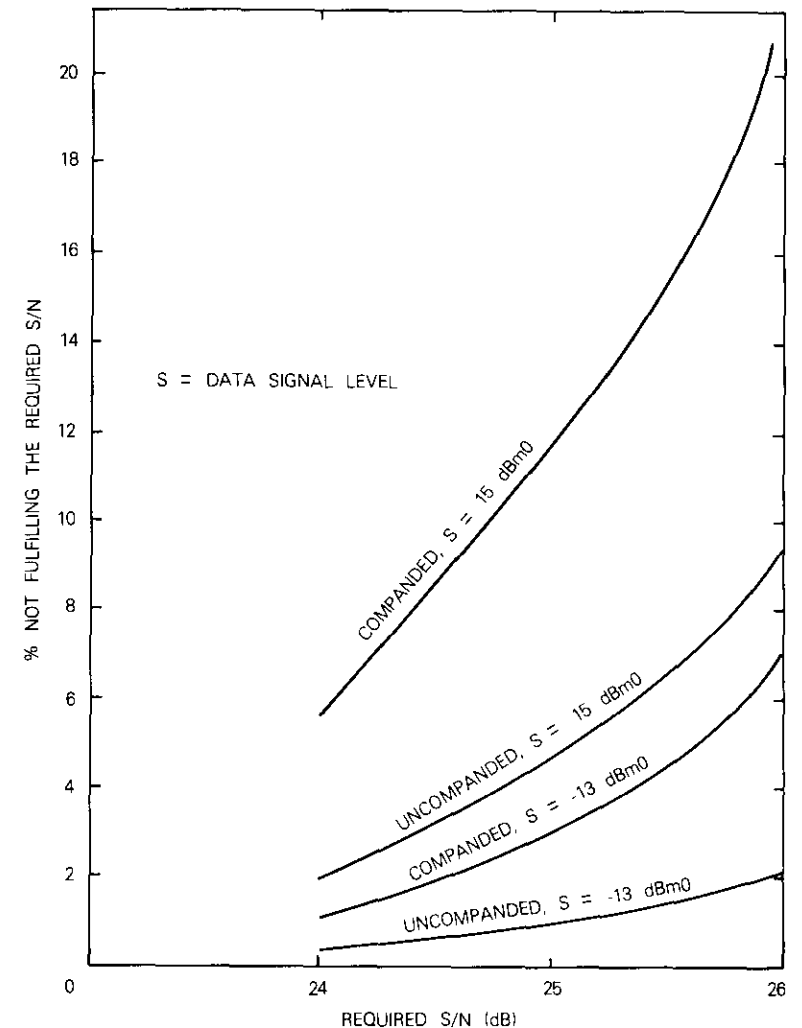
Figure 29. *Probability of Not Fulfilling the S/N Requirements*

Table 5 shows that, at the present standard data signal level of −13 dBm0, the mean S/N degradation for the given representative international circuit is 2 dB when the satellite link operates in the CFDM-FM transmission mode. In addition, Figure 29 shows that, at the same

−13-dBm0 level, the probability of not fulfilling, for example, the S/N = 24 dB requirement increases from about 0.4 percent in the FDM-FM transmission mode to about 1.2 percent in the CFDM-FM transmission mode.

In addition to the S/N ratio, the data transmission bit-error rate (BER) depends on parameters such as channel envelope delay and frequency response, impulse noise, and type of modem. The impulse noise is attenuated by the expander, with U being above the data signal level. The envelope delay and frequency response are generally not influenced by the insertion of a compandor (see Figure 13). This was confirmed by the measurements in Table 6, showing equal BERs at equal S/N ratios for the companded and uncompanded channel.

Signaling

In the CCITT No. 5 signaling system, the line signals are 2000- and 2400-Hz tone bursts, with a minimum duration of 100 ± 20 ms. The line signals are long compared to the compandor time constants; therefore, measurements were made only for the register-to-register signaling, where the signals are dual-frequency tone bursts (MF signals) of $-7- \pm 1$-dBm0 level per frequency [18], 55-ms duration, and 50-percent duty cycle.

In the CFDM-FM transmission mode, a repeated pattern of high frequency, low frequency, and maximum-difference frequency pairs representing the numbers 0, 1, and 7 was transmitted without access circuit noise and at the system noise level of -32 dBm0p. No transmission errors were detected, even when the standard transmission level was decreased by more than 10 dB.

Compandors in tandem

The terrestrial access circuit sections of an international connection may also include compandors. Therefore, the study included a limited experiment with two compandors in tandem.

A telephone circuit connection was made for live conversation between two parties, S and L, with L as the evaluator. The evaluator had to compare three circuit conditions, each with three circuit sections, as shown in Figure 30. The first and third sections, representing a low-noise uncompanded access circuit and a companded receive access circuit with high noise, respectively, remained unchanged. The second circuit section, representing the satellite system

TABLE 6. BER FOR TRANSMISSION RATE OF 4800-Bit/s MODEM TYPE BELL 208A

Satellite System Noise (dBm0p)	Transmission Level (dBm0)	Type of Channel	S/N	No. of Repetitions[a]	Mean Error	Standard Deviation	BER
−32	−13	Uncompanded	19	5	381.2	20.7	4×10^{-4}
	−13	Companded	20	5	9.8	5.1	1×10^{-5}
	−16	Companded	18.5	1	213		2×10^{-4}
−35	−13	Uncompanded	22	1	2		2×10^{-6}
	−16	Uncompanded	19	4	376	31	4×10^{-4}
	−13	Companded	23	2	0		$<1 \times 10^{-6}$
	−16	Companded	21.5	1	0		$<1 \times 10^{-6}$
	−20	Companded	19.5	2	126	1.4	1×10^{-4}
−35[b]	−13	Uncompanded	19	5	263	34	3×10^{-4}
	−13	Companded	20	5	44	23	4×10^{-5}

[a] 10^6 bits/repetition.
[b] Two channels in tandem.
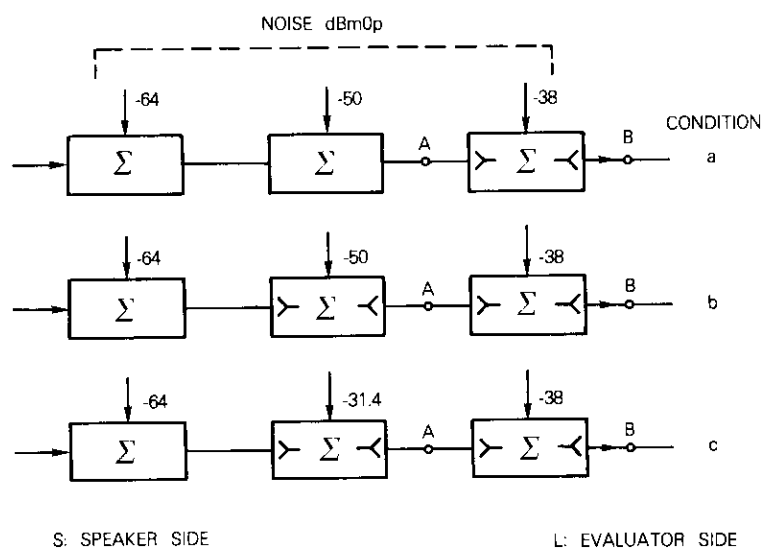
Figure 30. *Compandors in Tandem Test Conditions for Subjective Evaluation*

section, changed from uncompanded with a noise level of -50 dBm0p (condition a) to companded with the same noise level (condition b) to companded with the noise level increased to give the same idle channel noise output as in condition a (condition c).

Seven test subjects compared conditions b and a, followed by conditions c and a. They were required to rate conditions b and c relative to condition a in five categories (much worse, worse, equal, better, and much better). When the category ratings were associated with integers from -2 to $+2$, the means and standard deviations were as follows:

	Mean	Standard Deviation
condition b compared to condition a	-0.14	0.9
condition c compared to condition a	-1.14	0.7

The results indicate that condition b was no different from condition a for the sample size used. Condition c was worse than condition a. It may be concluded that the subjective speech performance of a circuit is not affected by insertion of tandem compandors if the noise contributions remain unchanged. However, the speech performance is degraded when the noise contribution of the additional companded circuit section is increased to result in equal idle channel noise at the output. Therefore, the performance of tandem compandors utilizing the compandor advantage to recover performance is between the two limiting cases tested, and is expected to result in some degradation compared to non-tandem usage.

Discussion

Data transmission

Although the use of compandors may result in a carrier capacity increase of 100 percent or more depending on the channel numbers and C/N ratios (see Figure 27), this increased capacity is possible only for speech transmission. Data transmission, however, is adversely affected.

There are two methods of diminishing data transmission degradation, both at the expense of the required bandwidth. One method is to increase the S/N ratio of all channels by using less compandor advantage than that measured in subjective experiments. An example of such a compromise solution resulted in an average channel capacity enhancement of 70 percent. With this compromise solution, the S/N degradation for data transmission over a representative international connection is 2 dB and the speech transmission performance is somewhat better than required.

The second method ensures the required speech transmission performance and selectively ensures a better S/N ratio for the data

transmitting channels. A selective S/N increase for data transmission can be achieved by channel dedication and routing techniques or, without channel dedication, by improving the channel S/N ratio during data transmission. This second alternative may utilize the echo control disabling tone preceding the data transmission to raise the compandor unaffected level. Improving the S/N ratio for data-only transmission is more economical in terms of bandwidth, but more complicated than achieving a compromise improved S/N for all channels.

Compressed multichannel load

The bilinear approximation of the equivalent compressed peak load P'_{cq} is based on the measured peak ($\varepsilon = 10^{-5}$) to rms differences of compressed and uncompressed multichannel loads and on the Gaussian distribution approximation for higher channel numbers. The P'_{cq} approximation is nearly as good as the bilinear P_{cq} approximation of the uncompressed load, although somewhat conservative, since the channel limiter action has a more significant effect on uncompressed load than on compressed load measurements. A mathematically consistent derivation of the compressed multichannel load is quite feasible. The derivation method is the same as that given in References 13 and 14 for the uncompressed load.

Compandor advantage definition

The compandor advantage definition given in this paper, $N'_s - N_s$ (designated "Definition A"), is not the only possible definition. In particular, another definition (designated "B") [19] should be considered. This definition is given as $(TT - N_s) - [(TT)' - N'_s]$, where $(TT)'$ is the compressed 0-dBm0 test tone power, which is equal to $U/2$.

A compandor advantage, found with definition A to be 10 dB at $U = -11$, is transformed to 15.5 dB when definition B is used. The two definitions give the same numerical values only for $U = 0$ dBm0. Definition B normalizes the compandor advantage to $U = 0$ dBm0. In addition, when the test tone deviation, f_r, is interpreted as the deviation associated with the compressed test tone, the $U/2$ term of the multichannel load is cancelled in the Carson's Rule bandwidth expression. Thus, definition B permits CFDM-FM calculations without the formal presence of U.

The authors prefer definition A. The presence of U in the calculations is a reminder that the load is changed when compressors are used. As

mentioned previously, the changed load must be taken into account external to the FM-modulator-to-FM-demodulator path.

Conclusions

Measurements, evaluations, and calculations have shown that compandors can significantly enhance satellite communications capacities by an average of 70 percent and by as much as 100 percent for smaller carriers. These projected increases would not degrade the subjectively perceived quality of the speech transmission.

A noise penalty of about 2 dB will be encountered by data signals in an end-to-end international connection, including terrestrial (i.e., national) extensions with their own noise contributions. Companded connections in tandem will generally tend to cause a performance degradation, which is perhaps more severe for data transmission than for speech.

Acknowledgments

References

[1] N. C. Norman, "The Voice-Operated Compandor," *Bell Labs Record*, 1934, p. 98.
[2] E. M. Rizzoni, "Compandor Loading and Noise Improvement in Frequency Division Multiplex Radio-Relay Systems," *Proc. IRE*, February 1960, pp. 208–220.
[3] W. R. Lundry and L. F. Willey, "The N2 Carrier Terminal-Circuit Design," *Bell System Technical Journal*, Vol. XLIV, No. 5, May–June 1965, pp. 761–785.
[4] G. W. Bleisch and C. W. Irby, "The N3 Carrier System: Objectives and Transmission Features," *Bell System Technical Journal*, Vol. XLV, No. 6, July–August 1966, pp. 767–799.

[5] R. C. Skevington, "Compandors for FDM/FM Voice Traffic," *NTC '79* Conference Record, pp. 12.5.1–12.5.5.

[6] K. Jonnalagadda, "Syllabic Companding and Voice Capacity of a Transponder," *RCA Review*, Vol. 41, No. 3, September 1980, pp. 257–268.

[7] S. J. Campanella, H. G. Suyderhoud, and M. Wachs, "Frequency Modulation and Variable Slope Delta Modulation in SCPC Satellite Transmission," *Proc. of the IEEE*, Vol. 65, No. 3, March 1977, pp. 419–434.

[8] *CCITT Orange Book, Geneva, 1976*, Vol. III-1, Rec. G.162.

[9] H. G. Suyderhoud, "Subjective Assessment of Delta Modulation at 16, 24, 32, and 40 kbit/s for Satellite Circuit Application," 4th Digital Satellite Conference, Montreal, Canada, 1978.

[10] Bell Telephone Laboratories, Inc., *Transmission Systems for Communications*, Ch. 9 and 28, 1971.

[11] *CCITT Orange Book, Geneva, 1976*, Vol. III-1, Rec. G.223.

[12] B. D. Holbrook and J. T. Dixon, "Load Rating Theory for Multichannel Amplifiers, *Bell System Technical Journal*, Vol. 18, No. 4, October 1939, pp. 624–644.

[13] T. deBoer and C. Hooijkamp, "The Required Load Capacity of FDM Multi-Channel Amplifiers, *Philips Telecommunications Review*, Vol. 36, 1978, pp. 225–242.

[14] T. deBoer and C. Hooijkamp, "The Required Load Capacity of FDM Multi-Channel Amplifiers if Single-Channel Peak Limiting is Employed," *Philips Telecommunications Review*, Vol. 38, January 1980, pp. 27–36.

[15] *CCIR Green Book, Kyoto, 1978*, Volume IV, Report 708.

[16] R. W. Berry, "Speech-Volume Measurements on Telephone Circuits," *Proc. IEE*, Vol. 118, No. 2, February 1971, pp. 335–338.

[17] *CCITT Orange Book, Geneva, 1976*, Vol. VIII-1, Rec. V.2.

[18] *CCITT Orange Book, Geneva, 1976*, Vol. VI-1, Rec. Q.153.

[19] H. L. Weinberger, Private Communication.

Appendix A. Block diagram of the experimental link

In the majority of experiments, a laboratory simulated earth station to earth station to satellite connection was used with an allocated satellite bandwidth of 2.5 MHz (the present minimum INTELSAT bandwidth) and an occupied bandwidth of 2 MHz. The carrier was loaded with compressed multichannel speech.

Because the experimental phase was restricted to operating in the 2.5-MHz allocated bandwidth and because of the need to encompass all conditions for assessing compandor advantage, most of the test recordings were made by varying the *C/N* ratio while the simulated link was loaded with 120 speech
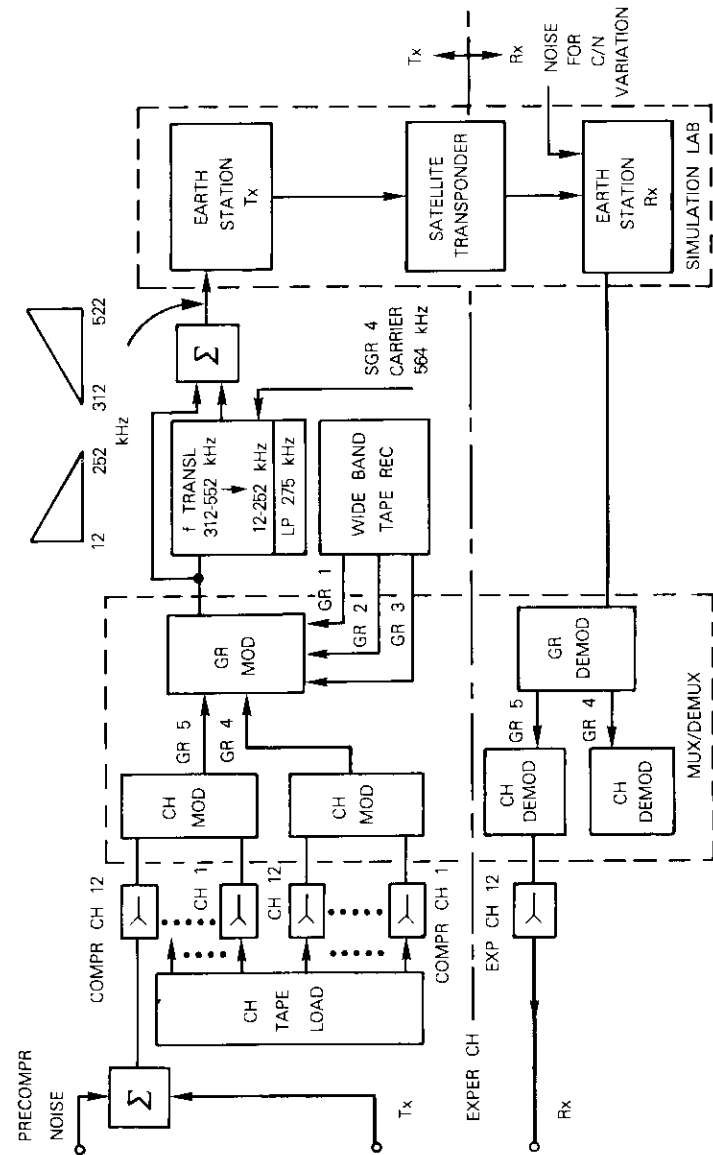
Figure A-1. *Experiment Block Diagram*

channels. A limited number of subjective evaluations were also performed on recordings made with a 60-channel load and $C/N = 12.7$ dB to verify the results obtained for 120-channel loading and high C/N ratios.

In Figure A-1, the multichannel load consisted of two supergroups originating from one single supergroup source. One supergroup load was directly applied (312–552 kHz), and the second was a down-converted version (12–252 kHz). In the supergroup, the channels of groups GR4 and GR5 were loaded with conversational speech, recorded, and labeled "CH. TAPE LOAD." Groups GR4 and GR5 were recorded on two tracks of a wideband tape recorder, and GR4 was recorded with a 25-ms delay (between the recorder and playback heads) on the third track. The replay of the three tracks provided group loading for GR1, GR2, and GR3. The inherent delay between the channel-loading tape recorders and the group-loading wideband tape recorder decorrelated the supergroup channels. The combined load of the two supergroups was adjusted for the proper rms value of 120 channels. The individual channel sources were adjusted to simulate an actual speech volume distribution. All recordings and measurements were made on the top baseband channel (GR5, CH 12).

Figure A-2 is a detailed block diagram of the simulated satellite link. The necessary system parameters were adjusted for 60- and 120-channel companded telephone loading.

Appendix B. Distribution meter

The distribution meter was built to measure the voltage distribution of linear and compressed single-channel and multiple-channel signals. It will be described based on the functional block diagram of Figure B-1 and an application example used for the distribution measurements of Figures 17 to 20.

The absolute value of the speech samples was measured and distributed in 16 equidistant intervals. The read-only memories (ROMs) have 1,024 memory cells, each addressed by a 10-bit combination which is one of the 1,024 possible digitized voltage values. Since four bits are necessary to identify 16 intervals, only one of the two ROMs was needed and programmed. Each group of $1,024:16 = 64$ ROM 4-bit words was programmed identically. The identical words were addressed with the analog-to-digital (A/D) converted voltage samples associated with the appropriate positive and negative intervals of the A/D converter (0- to +5-V and 0- to −5-V input voltage range, respectively).

In the measuring phase of the distribution meter, the ROM, and consequently the voltage sample, addresses the 256-word random access memory (RAM) bank of $8 \times 4 = 32$ bits per word. The addressed RAM word is transferred to a decimal counter, augmented with one, and rewritten to the same location. Therefore, the RAM words are associated with voltage intervals and count the number of samples belonging to the interval.

The measuring phase is terminated when the selected number of 10^5, 10^6, 10^7, or 10^8 samples is distributed in intervals. The sampling rate can be 9.756,
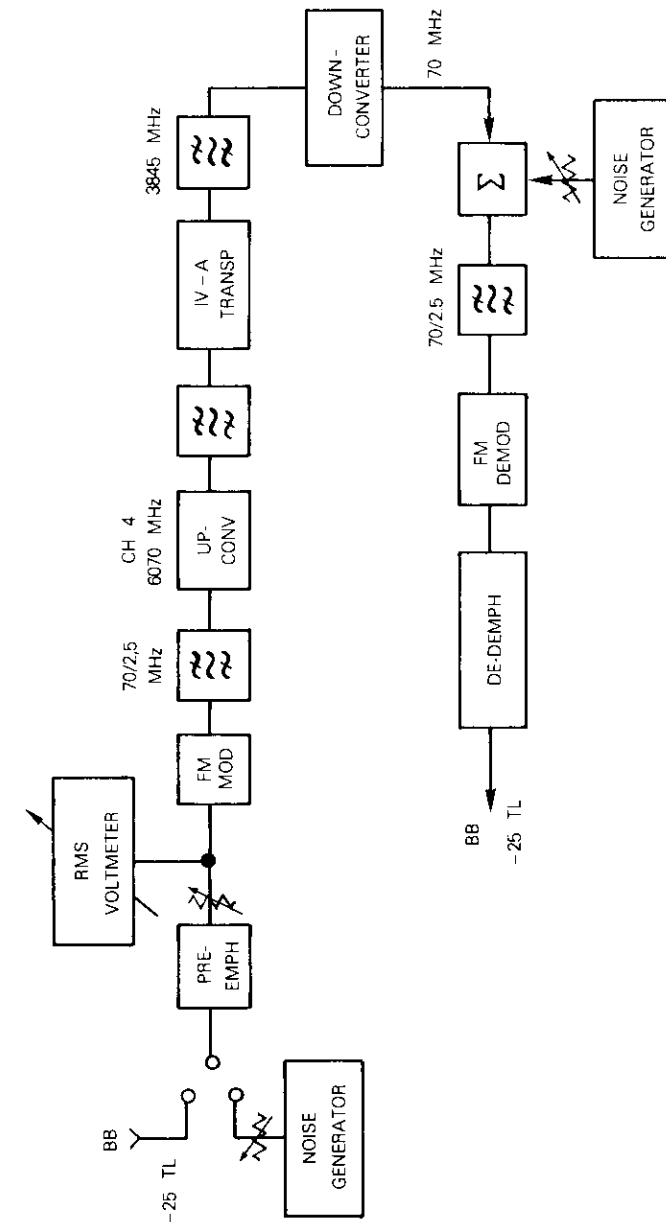
Figure A-2. Simulated Satellite Link Block Diagram

312.5, or 833 kHz. The number of the not necessarily equidistant intervals for the ± 5-V analog input range can be selected from 2^4 to 2^x.

The signal to be measured must be amplified to utilize the distribution meter input voltage dynamic range. The voltage amplification is appropriately adjusted using the overload indicator, which is lit whenever the input voltage equals or exceeds 5 V.

The distribution measurement is concluded with the recording phase, which can be manual or automatic. In both cases, the RAM content is addressed by a counter (right side on the address line). This counter is augmented step-by-step with a pushbutton for manual recording of the RAM's content, which is shown on a display, together with the address counter state representing the interval number. In the automatic recording mode, the same information is printed on a connected HP5050 digital recorder at a speed of 80 ms per RAM word. The continuous mode can also be selected when repetitive measurements and recordings are made.

The measuring phase of the distribution measurement is preceded by the initializing and idle phases. The measurement is started by depressing the "start" pushbutton, which transfers the distribution meter from the idle phase to the subsequent initialization, measuring, and recording phases.

Figure B-1. *Distribution Meter Functional Diagram*
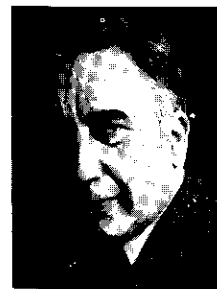
George G. Szarvas received a Dipl. Eng. degree in electrical and mechanical engineering from the Technical University in Budapest, Hungary. He has completed postgraduate courses at the Royal Institute for Technology in Stockholm, Sweden. Before he joined COMSAT in 1969, Mr. Szarvas had worked for the Telecommunications Research Institute in Hungary, for L. M. Ericsson and Facit Electronics in Sweden, and for the Swedish Tele-administration. He is currently a member of the technical staff in the Signal Processing Department of the Communications Processing Laboratory. He is a member of the IEE.

Henri G. Suyderhoud received the Ingenieur degree from Delft Technological University in the Netherlands in 1955, and an M.S. degree in applied mathematical statistics from Rutgers, New Brunswick, in 1966. He is currently Manager of the Signal Processing Department of the Communications Processing Laboratory where he is responsible for signal processing research and development using both digital and analog techniques as well as the development of subjective evaluation techniques to assess transmission quality. His experience includes development of echo cancellers and speech processing and encoding techniques for achieving transmission economy. Prior to joining COMSAT, Mr. Suyderhoud worked for 11 years at Bell Telephone Laboratories in the fields of exchange area and toll transmission engineering, echo control, and picture phone. He is a senior member of IEEE and the American Statistical Association.

Synchronization accuracy and error analysis of open-loop TDMA systems*

T. R. LEI

(Manuscript received August 15, 1980)

Abstract

Open-loop acquisition and synchronization is a method of controlling TDMA burst position without the need of traffic stations to observe their own down-link burst returns. In an open-loop network, the burst transmit delay of each station is calculated by a controlling station based on knowledge of satellite and earth station positions. Ranging stations with sufficient geographic separations perform satellite range measurements which allow determination of the satellite position.

Synchronization accuracy in an open-loop TDMA system is a function of range measurement and traffic station implementation errors. Antenna site location error and earth station electric path length calibration errors also affect the overall system accuracy. This paper discusses possible error sources that may be encountered in an open-loop TDMA system. Numerical examples of burst position errors are given for stations located in the Atlantic Ocean region.

Introduction

In a TDMA system, earth stations access a given satellite transponder sequentially in time so that each station uses the full power and bandwidth of the transponder during assigned time intervals. Each station must transmit its traffic burst at a precise moment to prevent it from overlapping with those of other stations. A traffic burst is initially placed in its assigned time slot during the acquisition process and is maintained in its allocated position by means of synchronization.

Open-loop acquisition and synchronization [1]–[3] is a method by which TDMA frame synchronization can be achieved without the need of traffic stations to observe their own down-link burst returns. Contrary to the closed-loop method, which implies control of burst transmission time by observing the position of the burst in the frame, open-loop control accomplishes this function through calculations based on knowledge of the satellite and earth station positions.

A periodic time marker is required to establish the time reference for traffic bursts within a TDMA frame. This common time marker, known as the reference burst, can be generated either by an oscillator on board the satellite or by a reference station(s) on the ground. This paper assumes that a reference station transmits reference bursts to the satellite, which broadcasts them to traffic stations via a global coverage antenna. As shown in Figure 1, after receiving the reference burst, each station must establish a transmit time reference so that a traffic burst transmitted at this precise moment will be coincident with the reference burst at the satellite. The time delay, D_n, between the received reference burst and the transmit time reference is referred to as the transmit reference delay for station n. At any given time, each station may require different values of D_n because of the unequal distances between the satellite and stations; besides, the values of D_n are generally time dependent because of the small motions of geostationary satellites. These motions result in changes in the distance between satellites and earth stations, and can be as much as 80 km for a satellite with 0.0005 eccentricity and stationkeeping tolerances of $\pm 0.1°$ E/W and $\pm 0.1°$ N/S. The variations in D_n can be as much as 540 μs depending on the station's location.

A traffic station must position and maintain its traffic burst to within a preassigned time slot S_n seconds apart from the reference burst as shown in Figure 1. The actual time of transmission at station n must be S_n seconds after the transmit time reference, and hence t_n seconds

after the received reference burst, that is, $t_n = D_n + S_n$. The value of t_n, or D_n, is calculated either locally at the traffic station or at a central controlling station which broadcasts the results via the satellite to traffic stations. The accuracy of these values is proportional to the accuracy of the estimated satellite position, which is determined by one or more ranging stations. This position is affected by error sources such as range measurement, calibration, and computation error. This paper discusses error sources that may be encountered in an open-loop system; consequently, it derives the accuracy of the calculated transmit reference delay, D_n, and determines the burst position accuracy.
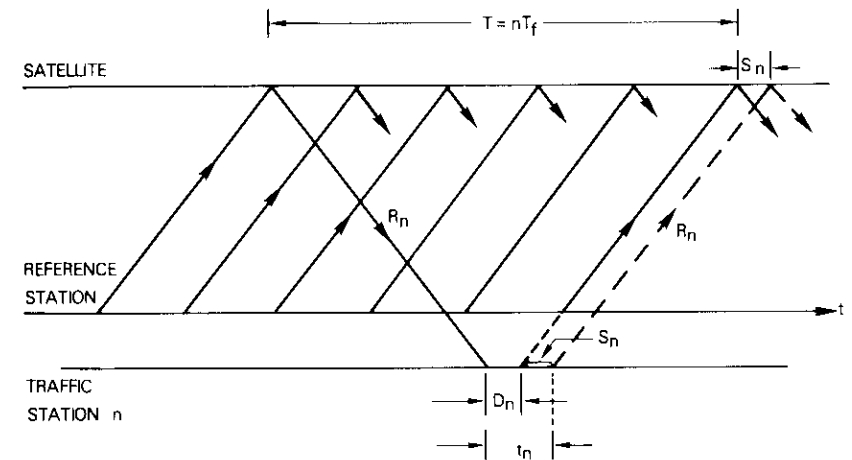

Figure 1. *Burst Transmission Timing Diagram*

Open-loop acquisition and synchronization

In an open-loop TDMA network, a traffic station transmits its burst by implementing the transmit reference delay D_n, which is obtained according to the timing diagram shown in Figure 1:

$$D_n = nT_f - 2\frac{R_n}{c} \qquad (1)$$

where R_n = distance between the satellite and
             the traffic station
         c = velocity of light
         T_f = TDMA frame period
         n = an integer.

R_n is obtained in terms of the coordinates of the satellite and the traffic station.

The satellite coordinates are determined by a central station based on the satellite ranges provided by ranging stations which constantly measure their propagation delays to the satellite. For the case of three ranging stations, the following equations hold:

$$R_A = \sqrt{(X - X_A)^2 + (Y - Y_A)^2 + (Z - Z_A)^2} \qquad (2)$$

$$R_B = \sqrt{(X - X_B)^2 + (Y - Y_B)^2 + (Z - Z_B)^2} \qquad (3)$$

$$R_C = \sqrt{(X - X_C)^2 + (Y - Y_C)^2 + (Z - Z_C)^2} \qquad (4)$$

where R_A, R_B, R_C = distances between the satellite and
                         the antennas of stations A, B, and C
        X, Y, Z = satellite coordinates
        X_i, Y_i, Z_i = coordinates of the antenna of
                         ranging station i, and i = A, B, or C.

An open-loop TDMA system thus involves satellite ranging by ranging stations, satellite coordinates determination by a central station, calculation of propagation delays of traffic stations by either a central station or traffic stations, calculation of transmit reference delays, and implementation of the transmit reference delays by traffic stations. It is assumed in this paper that all computations are performed at the central station, and traffic stations simply implement the proper transmit delays.

Burst position accuracy of open-loop systems

Each station must establish a transmit reference timing by delaying D_n symbols after the detection of the unique word of the down-link reference burst as depicted in Figure 1. With open-loop control, the value of D_n is calculated based on knowledge of the satellite and earth station positions. Theoretically, this procedure ensures that all traffic

bursts are perfectly aligned at the satellite; however, errors may occur in this operation and the resulting burst may not be exactly on the target position.

The error sources can be separated into two categories: errors in the value of D_n, and those occurring at the traffic stations. The former is caused by measurement errors at ranging stations and computation errors at the central station; the result is an erroneous D_n value transmitted to traffic stations. The latter is the implementation error introduced at traffic stations executing the transmit reference delay, D_n. In this paper, errors such as burst position and range measurement will be expressed in terms of the symbol period unit rather than in units of time.

The fundamental clock frequency in the digital ranging system is assumed to be 60 MHz, $i.e.$, the TDMA symbol rate. Since there is no higher frequency clock in either the ranging unit or the TDMA terminal, the timing resolution is determined by the symbol period, which is 16.7 ns. The symbol period is the basic unit in data distribution. The number of binary digits allocated in the control part of the reference burst for the distribution of synchronization data does not allow a fraction of one symbol to be transmitted. Hence, the maximum error in the data distribution process is ±0.5 symbol.

Range measurement errors

Range measurement errors may occur at ranging stations because of the five causes discussed below.

RANGE COUNTER TIMING ERROR

The range counter measures the round-trip propagation delay as shown in Figure 2. The transmission of the range burst at time t_1 starts the range counter, and the detection of a range burst unique word stops it at time t_2. The counter thus registers a time interval τ, which is less than one frame period; then satellite range R can be calculated as follows:

$$R = \frac{nT_f + \tau}{2} c \qquad (5)$$

where T_f = frame period
         n = integer
         c = velocity of light.
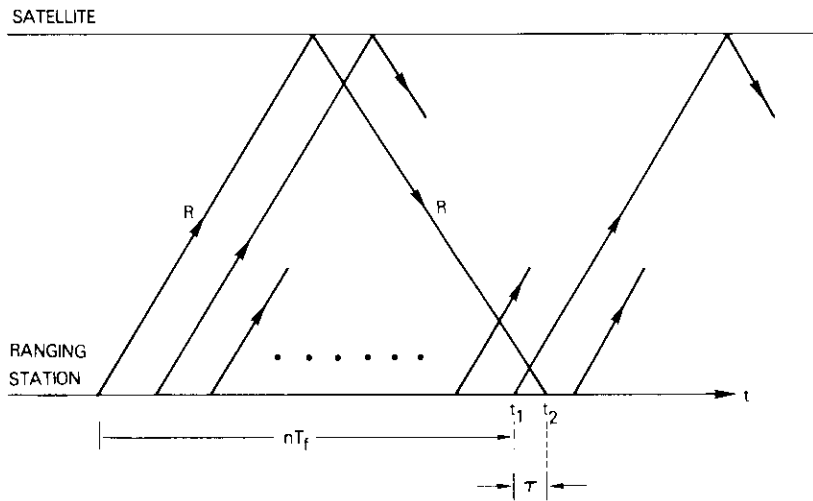
Figure 2. *Global Beam Digital Satellite Ranging*

The value n can be measured with a coarse frame counter, or estimated using the current satellite position. The typical satellite round-trip range variation is 1.1 ms; so n can be estimated easily if the frame period is longer than 1.1 ms. If the frame period is short, a simple calibration procedure is required.

During measurements of τ, a reclocking error will result, as shown in Figure 3. This error is evenly distributed between 0 and 1 symbols; hence, $0 \leq \hat{\tau} - \tau < 1$. In equation (5), the factor ½ results in a range measurement error, e_r:

$$0 \leq e_r < 0.5 \quad .$$

QUANTIZATION ERROR AT TRANSMISSION

The measured range will be transmitted to a central station in symbol units. Since $nT_f + \tau$ may not always yield an even number, division by 2 may result in a truncation error, e_q:

$$-0.5 < e_q \leq 0 \quad .$$

DOPPLER SHIFT IN THE RECEIVED FRAME REFERENCE RATE

A round-trip propagation delay takes about 300 ms. During this time, the received frame reference rate varies because of Doppler shift. For orbits with 0.1° inclination, this may be as much as ±20 ns/s. Hence,
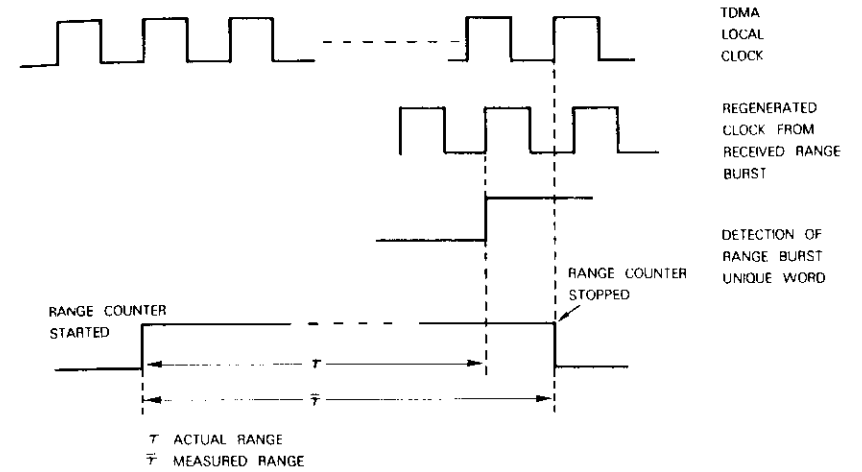
Figure 3. *Range Counter Clock Resolution Error*

over a 300-ms time interval, the accumulated Doppler shift error is of the order of

$$\frac{\pm 20 \text{ ns}}{\text{s}} \times 300 \text{ ms} = \pm 6 \text{ ns} = \pm 0.4 \text{ symbol}$$

giving an additional range measurement error, e_d,

$$-0.2 \leq e_d \leq 0.2 \quad .$$

This error can be reduced or eliminated if the Doppler shift is predicted using satellite ephemerides or a highly stable clock at the ranging station. If the ranging station is also the reference station, this error will not exist.

ERROR INDUCED BY THE MEDIUM

The propagation velocity of microwaves in a medium other than free space is less than the speed of light. On the average, the ionosphere will add 15 ns at 6/4 GHz into satellite round-trip propagation delay. The troposphere will introduce additional delays, as shown in Table 1 [4].

These delays can be compensated for in the process of range measurement. However, propagation velocity fluctuations due to

atmospheric humidity, barometric pressure, wind, and rainfall will cause the tropospheric propagation delay to fluctuate about the average value. At a 20° elevation angle, for example, the propagation delay to the satellite could fluctuate as much as ± 5 ns, or approximately ± 0.3 symbol [5].

TABLE 1. ADDITIONAL ROUND-TRIP
PROPAGATION DELAY IN
TROPOSPHERE

Antenna Elevation Angle (°)	Additional Propagation Delay (ns)
90	20
20	53
10	100
5	165

CALIBRATION ERROR

Calibration error will generate a permanent offset in TDMA synchronization. Although frequent recalibration limits the amount of this error, a small calibration error may remain in the system at any given time. The calibration error of ranging stations which consists of antenna site location error and electric path length calibration error can be treated as a form of range measurement error. The electric path length calibration error is an offset in range measurement, and the problem of antenna site location error can be approached by considering that the antenna location is correct but the range measurement is in error by an amount corresponding to the displacement of antenna location. It is reasonable to assume that the location of ranging stations is accurate to within ± 0.5 s of an arc, which is equivalent to ± 15 m at the equator. In the vicinity of 45° latitude, where ranging stations are most likely to be found, 0.5 second of an arc in longitude is equivalent to a distance of about 10 m. For such a location error, the maximum equivalent range measurement error for stations at 27° of antenna elevation (*e.g.*, Andover), operating at a system clock of 60 MHz, is about ± 3 symbols. Since the electric path length calibration error caused by HPA, LNA, and satellite transponder switchover and redundant modem changeover is about ± 1.5 symbol, the total calibration error is

$$-4.5 \leq e_c \leq 4.5 \quad .$$

The total range measurement error at a ranging station is the sum of all above errors:

$$e = e_r + e_q + e_d + e_v + e_c$$

For the worst case, when every contribution is at its maximum, the total maximum range measurement error would be approximately ± 6 symbols.

Resulting Satellite Positional Error

In a global beam triangulation ranging system, the errors ΔX, ΔY, and ΔZ in satellite coordinates as a result of range measurement errors are

$$\Delta X = \frac{\partial X}{\partial R_A} \Delta R_A + \frac{\partial X}{\partial R_B} \Delta R_B + \frac{\partial X}{\partial R_C} \Delta R_C$$

$$\Delta Y = \frac{\partial Y}{\partial R_A} \Delta R_A + \frac{\partial Y}{\partial R_B} \Delta R_B + \frac{\partial Y}{\partial R_C} \Delta R_C$$

$$\Delta Z = \frac{\partial Z}{\partial R_A} \Delta R_A + \frac{\partial Z}{\partial R_B} \Delta R_B + \frac{\partial Z}{\partial R_C} \Delta R_C \quad . \tag{6}$$

where ΔR_A, ΔR_B, and ΔR_C are the range measurement errors. To specify the partial derivative terms, the relationships between X, Y, and Z and R_A, R_B, and R_C must be found from equations (2)–(4). Use of the first-order approximation and Cramer's rule yields

$$\Delta X = \frac{\begin{vmatrix} \Delta R_A & K_{AY} & K_{AZ} \\ \Delta R_B & K_{BY} & K_{BZ} \\ \Delta R_C & K_{CY} & K_{CZ} \end{vmatrix}}{D}$$

$$\Delta Y = \frac{\begin{vmatrix} K_{AX} & \Delta R_A & K_{AZ} \\ K_{BX} & \Delta R_B & K_{BZ} \\ K_{CX} & \Delta R_C & K_{CZ} \end{vmatrix}}{D}$$

$$\Delta Z = \frac{\begin{vmatrix} K_{AX} & K_{AY} & \Delta R_A \\ K_{BX} & K_{BY} & \Delta R_B \\ K_{CX} & K_{CY} & \Delta R_C \end{vmatrix}}{D}$$

where

$$D \triangleq \begin{vmatrix} K_{AX} & K_{AY} & K_{AZ} \\ K_{BX} & K_{BY} & K_{BZ} \\ K_{CX} & K_{CY} & K_{CZ} \end{vmatrix}$$

$$K_{AX} = \frac{X - X_A}{R_A}$$

and other elements in the determinants are similarly defined. If the measurement error is small, the following approximation can be used:

$$\frac{\partial X}{\partial R_A} = \frac{\Delta X}{\Delta R_A} \quad .$$

Hence, for example,

$$\frac{\Delta X}{\Delta R_A} = \frac{\begin{vmatrix} K_{BY} & K_{BZ} \\ K_{CY} & K_{CZ} \end{vmatrix}}{D} \quad .$$

After the remaining partial derivative terms have been determined, the following equations are obtained:

$$\Delta X = \frac{1}{D} \left\{ \begin{vmatrix} K_{BY} & K_{BZ} \\ K_{CY} & K_{CZ} \end{vmatrix} \Delta R_A + \begin{vmatrix} K_{AY} & K_{AZ} \\ K_{CY} & K_{CZ} \end{vmatrix} \Delta R_B \right.$$
$$\left. + \begin{vmatrix} K_{AY} & K_{AZ} \\ K_{BY} & K_{BZ} \end{vmatrix} \Delta R_C \right\} \quad (7)$$

$$\Delta Y = \frac{1}{D} \left\{ \begin{vmatrix} K_{BX} & K_{BZ} \\ K_{CX} & K_{CZ} \end{vmatrix} \Delta R_A + \begin{vmatrix} K_{AX} & K_{AZ} \\ K_{CX} & K_{CZ} \end{vmatrix} \Delta R_B \right.$$
$$\left. + \begin{vmatrix} K_{AX} & K_{AZ} \\ K_{BX} & K_{BZ} \end{vmatrix} \Delta R_C \right\} \quad (8)$$

and

$$\Delta Z = \frac{1}{D} \left\{ \begin{vmatrix} K_{BX} & K_{BY} \\ K_{CX} & K_{CY} \end{vmatrix} \Delta R_A + \begin{vmatrix} K_{AX} & K_{AY} \\ K_{CX} & K_{CY} \end{vmatrix} \Delta R_B \right.$$
$$\left. + \begin{vmatrix} K_{AX} & K_{AY} \\ K_{BX} & K_{BY} \end{vmatrix} \Delta R_C \right\} \quad . \quad (9)$$

The above equations give the errors in calculated satellite coordinates as a result of range measurement errors; the computational and processing delay errors are neglected. It can be shown that the computational error is negligible if the computer at the central station has the required resolution, and also if the time interval between successive range measurements is not much longer than 1 minute. The processing delay error is caused by the motion of the satellite while the central station is holding previously measured satellite ranges. Extrapolation algorithms can be employed to obtain a more accurate estimated current satellite position.

Resulting error in propagation delay of traffic stations

The transmit delay of each traffic station is calculated based on the currently estimated propagation delay between the satellite and traffic stations. Incorrect estimates of satellite position will result in erroneous propagation delays. The effect of erroneous satellite coordinates on the range calculations of traffic stations is given by the following equation:

$$\Delta d_n = \frac{\Delta R_N}{c} = \frac{1}{c} \left(\frac{X - X_N}{R_N} \Delta X + \frac{Y - Y_N}{R_N} \Delta Y + \frac{Z - Z_N}{R_N} \Delta Z \right) \quad (10)$$

where R_N = calculated satellite range for traffic station n
X_N, Y_N, Z_N = antenna site coordinates of station n.

Equation (10) is derived from range equations similar to equation (2); it can be combined with equations (7)–(9) to obtain the error in the estimated propagation delay of traffic stations caused by range measurement errors:

$$\Delta d_n = \frac{\Delta R_N}{c} = \frac{1}{c \cdot D} \left[\begin{vmatrix} K_{NX} & K_{NY} & K_{NZ} \\ K_{BX} & K_{BY} & K_{BZ} \\ K_{CX} & K_{CY} & K_{CZ} \end{vmatrix} \Delta R_A \right.$$
$$\left. + \begin{vmatrix} K_{AX} & K_{AY} & K_{AZ} \\ K_{NX} & K_{NY} & K_{NZ} \\ K_{CX} & K_{CY} & K_{CZ} \end{vmatrix} \Delta R_B + \begin{vmatrix} K_{AX} & K_{AY} & K_{AZ} \\ K_{BX} & K_{BY} & K_{BZ} \\ K_{NX} & K_{NY} & K_{NZ} \end{vmatrix} \Delta R_C \right] \quad . \quad (11)$$

ERROR IN D_n

The value of D_n is calculated from equation (1), in which three possible error sources existed: an error in the estimated satellite distance R_n, the assumption of constant propagation velocity in the path, and the assumption of constant frame rate, T_f, at the satellite without considering the Doppler effect. However, the second and third errors are very small, on the order of 10^{-6} symbols and 0.2 symbol, respectively. The error in D_n results primarily from the error in the estimated satellite propagation delay; thus,

$$\Delta D_n = 2\Delta d_n \qquad (12)$$

where Δd_n is given in equation (11).

Implementation errors

The transmit reference delay, D_n, is calculated by a central station with an error given by equations (11) and (12). More errors will be added by the traffic station during implementation of the transmit delay. The four error sources are discussed below.

QUANTIZATION ERROR IN D_n

The value of D_n must be quantized into integer multiples of the symbol period before being executed by the TDMA terminal. The quantization error is thus

$$-0.5 \le e_{qn} \le 0.5 \quad .$$

RECLOCKING ERROR

If the clock frequency at the local TDMA terminal is not synchronized to that of the reference station, the unique word detection pulse of the reference burst cannot immediately trigger the transmit delay counter at the local TDMA terminal; thus, a reclocking error of up to 1 symbol may occur. This error is evenly distributed between 0 and 1 symbol. To minimize the peak error, the transmit delay, D_n, can be offset by -0.5 symbol; hence, the reclocking error becomes

$$-0.5 \le e_m \le 0.5 \quad .$$

SATELLITE-MOTION-INDUCED ERROR

Ranging stations constantly measure satellite ranges in terms of

which satellite position can be calculated. The central station also constantly updates the values of transmit delay for traffic stations; however, traffic stations may be unable to implement immediately the "new" transmit delay because of a special superframe structure of a particular TDMA system. The local station may fail to receive or calculate a new transmit delay at a particular instant and will be required to use the previous value until a new value is obtained or the station ceases transmission. During these intervals, if the satellite position has changed, the continued use of previous transmit delays would cause errors in burst position. Since the burst position is measured with respect to the reference burst, and both the reference and traffic bursts are affected by satellite Doppler, the differential Doppler would affect the traffic burst position error.

With reference to Figure 4, if the time duration from the instant that a new transmit delay is calculated until it is executed and seen by the
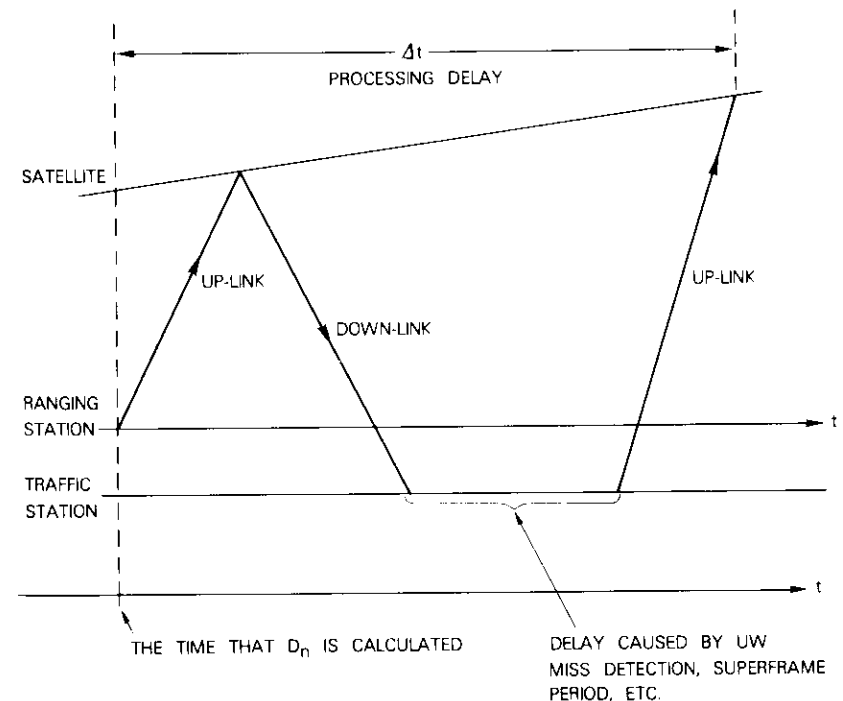
Figure 4. *Processing Delay*

satellite is Δt, the burst position error caused by satellite Doppler is

$$|e_{dn}| = (d_r - d_n) \Delta t$$

where d_r = satellite Doppler experienced by the
                    reference station
             d_n = satellite Doppler experienced by a
                    traffic station.

The maximum Doppler shift for a satellite with 0.0005 eccentricity and
$\pm 0.1°$ E/W, $\pm 0.1°$ N/S stationkeeping is about ± 8.7 ns/s or ± 0.5
symbol/s; if Δt is assumed to be 2 s, the burst position error caused
by satellite Doppler can be as much as ± 2 symbols. However, this
type of error can be reduced by employing extrapolation techniques
at traffic terminals.

TRAFFIC STATION CALIBRATION ERROR

A TDMA terminal can be several hundred meters from the earth
station antenna feed. The equivalent electric path length of the cables
and the propagation delay in electronic devices must be calibrated and
added to the calculated satellite range. Redundant terminal switchover
or HPA changeover often disturbs the calibration. With a ± 1 symbol
calibration error, the complete path of the receiving reference burst
and transmitting traffic burst may cause a ± 2 symbol error in the burst
position.

The antenna site location error of a traffic station would introduce
a ± 3 symbol error in range calculation or a ± 6 symbol error in burst
position [equation (12)] if a calibration accuracy of ± 0.5 s of an arc
in geographic location is assumed. The total amount of calibration
error is thus

$$-8 \le e_{cn} \le 8 \quad .$$

TDMA burst position error

The sum of the implementation error and the error in the estimated
D_n yields the total error in a TDMA burst controlled by the open-loop
method; that is, $e_b = 2\Delta d_n + e_{qn} + e_{rn} + e_{dn} + e_{cn}$.

The worst-case burst position error in a global beam open-loop TDMA
system is

$$e_b = \pm (2\Delta d_n + 11) \quad . \tag{13}$$

This equation assumes that an antenna site location error of ± 0.5 s of
an arc in both longitude and latitude exists at all earth stations. It is
valid at the beginning of open-loop TDMA operation while stations are
not yet precisely calibrated. Figures 5 and 6 show the worst-case burst
position errors on traffic stations in the Atlantic Ocean region, if each
ranging station experiences a maximum range measurement error of
± 6 symbols. The values in Figure 5 are much smaller than those of
Figure 6 because the ranging stations are geographically well separated;
thus, Δd_n is less sensitive to range measurement errors.

It has been pointed out that antenna site location error can, in
principle, be eliminated [6] while satellite Doppler can be predicted by
using extrapolation methods. For an open-loop TDMA system in which
the antenna site locations are precisely calibrated and extrapolation
algorithms can be employed to eliminate the error caused by satellite
motion, the result is a range measurement error of ± 3 symbols and a
traffic station implementation error of about ± 3 symbols. Figures 7
and 8 show the open-loop burst position error of this improved case.
The actual worst-case TDMA burst position accuracy, however, should
fall in between these two extremes.
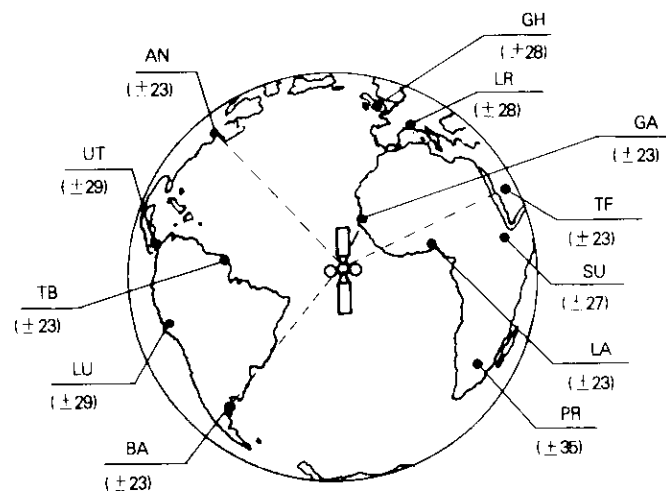
Figure 5. *Synchronization Accuracy of Open-Loop TDMA System
(Ranging Stations AN, BA, and TF)*
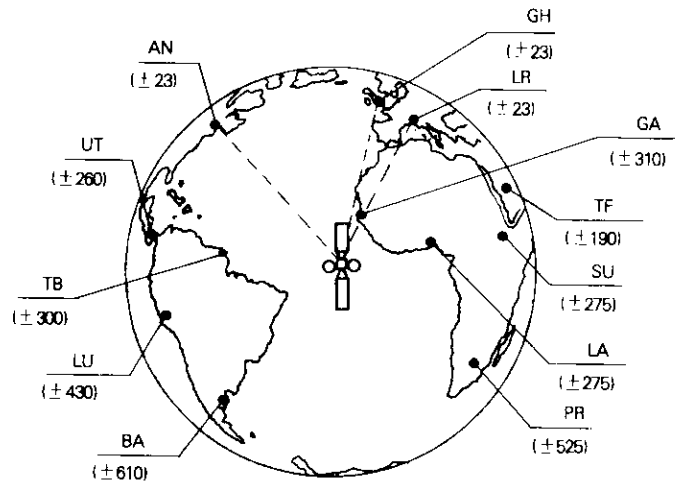
Figure 6. *Synchronization Accuracy of Open-Loop TDMA System
(Ranging Stations AN, GH, and LR)*

Figure 7. *Synchronization Accuracy of the Improved Open-Loop
TDMA System
(Ranging Stations AN, BA, and TF)*

Figure 8. *Synchronization Accuracy of the Improved Open-Loop
TDMA System
(Ranging Stations AN, GH, and LR)*

Conclusions

TDMA open-loop control performs acquisition and synchronization
based on knowledge of the estimated satellite position. The most
attractive feature of the open-loop system is the simplified acquisition
process, because the transmit delays of individual stations are always
available from the central station via the satellite link.

The errors entering the open-loop synchronization processes of a
TDMA system have been analyzed. Various error sources have been
discussed and their relative importance assessed. In a properly designed
open-loop system, TDMA frame synchronization can be maintained to
a reasonable accuracy if ranging stations are widely dispersed. If all
the station locations are properly calibrated, and satellite Doppler
extrapolated, the open-loop synchronization accuracy is expected to
be comparable to and, in some cases, better than that of a closed-loop
system.

Acknowledgment

The author wishes to thank Roger Colby for his valuable comments on this paper.

References

[1] S. J. Campanella and K. Hodson, "Open-Loop TDMA Frame Acquisition and Synchronization," *COMSAT Technical Review*, Vol. 9, No. 2A, Fall 1979, pp. 341–385.

[2] J. Deal, "Open-Loop Acquisition and Synchronization," Joint Automatic Control Conference, San Francisco, June 1974, *Proc.*, Vol. 2, pp. 1163–1169.

[3] A. Jefferies and K. Hodson, "New Synchronization Scheme for Communications Satellite Multiple Access TDM Systems," *Electronics Letters*, Vol. 9, No. 24, November 1973.

[4] J. J. Spilker, *Digital Communications by Satellite*, New York: Prentice-Hall, 1977.

[5] D. A. Gray, "Transit-Time Variations in Line-of-Sight Tropospheric Propagation Paths," *Bell System Technical Journal*, July–August 1970.

[6] T. A. Stansell, Jr., "Transit, The Navy Navigation Satellite System," *Navigation: Journal of the Institute of Navigation*, Vol. 18, No. 1, Spring 1971.

Tsu-Leun R. Lei received a B.S. from Fu-Jen Catholic University in Taiwan in 1968, an M.E.E. from North Carolina State University in 1972, and a Ph.D. in electrical engineering from the City University of New York in 1978. After joining COMSAT in February 1978, he participated in the INTELSAT TDMA field trial, in the development of new modem design concepts, and in the development and implementation of a global beam open-loop synchronization TDMA system. He recently joined the INTELSAT Communications R&D Section. Dr. Lei is a member of IEEE and Eta Kappa Nu.

Onboard clock correction for SS/TDMA and baseband processing satellites*

T. INUKAI AND S.J. CAMPANELLA

(Manuscript received December 16, 1980)

Abstract

Future communications satellites will embody advanced techniques such as SS/TDMA multibeam antennas, scanning beams, and baseband processing to provide high communications capacity with efficient utilization of available frequency and power resources. Flexibility to serve high and low traffic density areas will also be achieved. These new developments will eventually require the interconnection of satellite networks and of terrestrial and satellite networks. In terms of current technology, the onboard clock which supplies the timing for onboard switching and processing functions does not meet the clock accuracy required for synchronous network interconnection over the satellite lifetime; therefore, some corrective means must be provided.

This paper proposes a method of correcting the onboard clock drift from a ground station. A description is given of the proposed clock correction scheme and worst-case estimates of the correction error and required buffer size at traffic stations. The effects of secondary factors such as Doppler shift, range measurement error, quantization error of correction data, and delay incurred in transferring correction data to the satellite will also be discussed. Special consideration is given for a sidereal day clock correction.

Introduction

The onboard clock in an SS/TDMA system employing a synchronization window approach supplies the reference timing for all earth stations in the system. Without periodic frequency corrections, the onboard clock may drift as much as one part in 10^6 over the 7-year satellite lifetime. Therefore, serious problems would arise in the use of SS/TDMA in a plesiochronous telecommunications network, which may require a clock drift no greater than one part in 10^{11}. A number of schemes for correcting the onboard clock drift have been proposed; however, no analysis has been performed to ensure proper performance [1], [2].

This paper presents a clock correction scheme that employs a predictor to achieve stability. A linear discrete system model is used to analyze the worst-case timing error, clock correction rate, and buffer size requirement for traffic stations. The effects of timing errors caused by range measurement errors, Doppler shift, quantization noise, and delay incurred in transferring clock correction information to the satellite are also included. A numerical example provides system parameter values for typical SS/TDMA performance requirements. Finally, it is demonstrated that the analysis and discussion presented for an SS/TDMA system may be extended to a baseband processing satellite in which the master clock for onboard processing is controlled by a ground station.

Onboard clock correction scheme for SS/TDMA system

A basic scheme to correct onboard clock drift is shown in Figure 1. The clock drift is corrected periodically with period T; the subscript n represents the nth interval correction values. The choice of the correction period, which can range from several minutes to several days or longer, depends on the performance requirements of a particular system. The function of each building block of the clock correction scheme is described below.

Onboard clock

The onboard clock generates the timing for periodically altering switch states of a microwave switch matrix according to the pattern stored in the onboard memory. Its nominal frequency, f_0, is the same as that of the reference station clock, and the drift rate is denoted by

Figure 1. *Onboard Clock Correction Diagram for SS/TDMA System*

$\rho_s(t)$. The instantaneous clock frequency is then $f_0[1 + \rho_s(t)]$. Since the onboard clock is adjusted (or corrected) at the rate of w_n s/s in the nth correction interval, its instantaneous frequency is

$$f_s(t) = f_0[1 + \rho_s(t)](1 - w_n) \qquad (1)$$

$$\cong f_0[1 + \rho_s(t) - w_n] \quad .$$

Accordingly, the sync window timing and hence the reference frame timing are determined by this corrected clock frequency.

Phase error measurement

The acquisition and synchronization unit (ASU) of the reference station transmits a short burst called a metering burst to the sync window in every frame and determines the trailing edge of the window by multiple measurements of return bursts [3]–[5]. From 32 to 64 measurements are required to locate the sync window position with an error probability ranging from 10^{-9} to 10^{-16} for a channel error rate of 10^{-2}. The departure of the measured trailing edge position from its nominal position is the short-term phase error denoted by x_i. The phase error measurement may be repeated once every 0.5 to 1 s over the clock correction interval. The accumulation of short-term phase errors leads to a long-term phase error, s_n, in the nth interval.

The quantity s_n, which contains not only the onboard clock drift term but also the effect of the up-link Doppler shift, $\rho_u(t)$, can be written as

$$s_n = [(\rho_s)_n - (\rho_u)_n - w_n]T \qquad (2)$$

where $(\rho_s)_n$ and $(\rho_u)_n$ are the average clock drift rate and the long-term Doppler shift of the nth correction interval, respectively (see Appendix A).*

Transmit timing generator

This unit generates the metering burst (also reference burst) transmit timing from the reference clock, which has a timing inaccuracy as small as 10^{-11}. The transmit timing is adjusted by the amount of short-term phase error x_i to compensate for onboard clock drift and up-link Doppler shift. Since a large jitter in the reference burst timing is not desirable, a practical circuit may employ a smoothing algorithm which predicts the drift between corrections.

Incremental clock correction

A long-term phase error, s_n, is integrated in accumulator Σ_1 and also added to the integrator output, y_n. This yields the phase correction needed to minimize the mean departure of the clock from the reference frequency, f_0, during the next interval of duration T. The summed value is then averaged over the length T of one correction interval to obtain an incremental clock frequency correction datum, u_n; this value is quantized and then transmitted to the satellite at the end of the nth interval. The digital integrator is important in the ASU because it detects and subsequently corrects undesirable timing errors caused by a biased frequency offset (nonzero long-term drift) in the onboard clock that degrades plesiochronous services.

Onboard clock correction

The correction rate w_n is obtained by integrating the incremental clock corrections, u_n, in accumulator Σ_2. The value w_n is incremented at the beginning of the nth correction interval by the amount u_{n-1}. The

---

*The effect of satellite Doppler becomes quite small when the correction interval is equal to a sidereal day.

clock correction error of the nth interval is then $(\rho_s)_n - w_n$.

Accumulator Σ_2 may be located on board the satellite so that the incremental values u_n are sent over the command link, as shown in Figure 1. The accumulator may also be located in the ASU, in which case the total correction rate w_n is transmitted to the satellite.

Analysis

A discrete system model of the onboard clock correction scheme is shown in Figure 2, where e_n is the quantization error of u_n and the symbol z^{-1} denotes one sample (or one correction interval) delay.
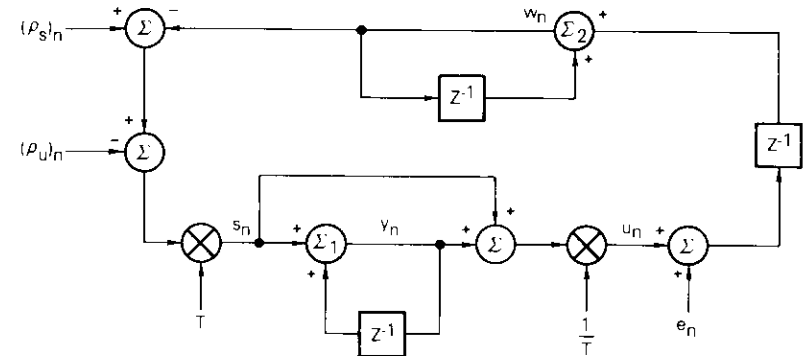
Figure 2. *Discrete System Model for Onboard Clock Correction*

Figure 3 illustrates the behavior of the clock correction loop for a ramp, a step, and a typical clock drift function without Doppler shift and quantization. The loop exhibits a transient response with a duration of two sample intervals. This is clearly seen for the responses to the ramp and step clock drift functions.

This model contains three external sources (inputs) which characterize system performance: $(\rho_s)_n$, $(\rho_u)_n$, and e_n. Since the system is linear, the effect of each timing error source can be analyzed independently.

Onboard clock drift

Variables s_n, y_n, u_n, and w_n dictate system performance. To estimate these values under the worst-case conditions, let $(\rho_u)_n = e_n = 0$ in

Figure 2. A detailed analysis is shown in Appendix B, and the results are summarized as follows:

$$s_n = [(\rho_s)_n - 2(\rho_s)_{n-1} + (\rho_s)_{n-2}]T \tag{3a}$$

$$y_n = [(\rho_s)_n - (\rho_s)_{n-1}]T \tag{3b}$$

$$u_n = 2(\rho_s)_n - 3(\rho_s)_{n-1} + (\rho_s)_{n-2} \tag{3c}$$

$$w_n = 2(\rho_s)_{n-1} - (\rho_s)_{n-2} \tag{3d}$$

The clock correction error is given by

$$(\rho_s)_n - w_n = (\rho_s)_n - 2(\rho_s)_{n-1} + (\rho_s)_{n-2} \quad . \tag{3e}$$

Let $\Delta\rho_s$ be the worst-case onboard clock inaccuracy per correction interval T; that is, the clock frequency departure is no greater than $f_0\Delta\rho_s$ during interval T. The inequality

$$|(\rho_s)_n - (\rho_s)_{n-1}| \leq \Delta\rho_s \tag{4}$$

which is proved in Appendix C, is used to compute the following system parameter bounds:

long-term phase error: $|s_n| \leq 2\Delta\rho_s T \tag{5a}$

cumulative phase error: $|y_n| \leq \Delta\rho_s T \tag{5b}$

incremental clock correction: $|u_n| \leq 3\Delta\rho_s \tag{5c}$

clock correction error: $|(\rho_s)_n - w_n| \leq 2\Delta\rho_s \quad . \tag{5d}$

Another important quantity is the reference burst timing inaccuracy at a traffic station, which must provide enough buffer to absorb the worst-case timing error due to the proposed clock correction scheme. Since the cumulative timing error y_n is bounded, the long-term clock drift at a traffic station is zero relative to the reference station clock. If a traffic station possesses a sufficient buffer for a Doppler shift, the additional buffer requirement is determined by the worst-case clock correction error (Appendix D) and is given by the quantity

buffer size: $6\Delta\rho_s T \quad . \tag{5e}$

f(t) – ONBOARD CLOCK FREQUENCY
$\hat{f}(t)$ – CORRECTED ONBOARD CLOCK FREQUENCY
f_0 – ASU REFERENCE CLOCK FREQUENCY
T – CLOCK CORRECTION INTERVAL
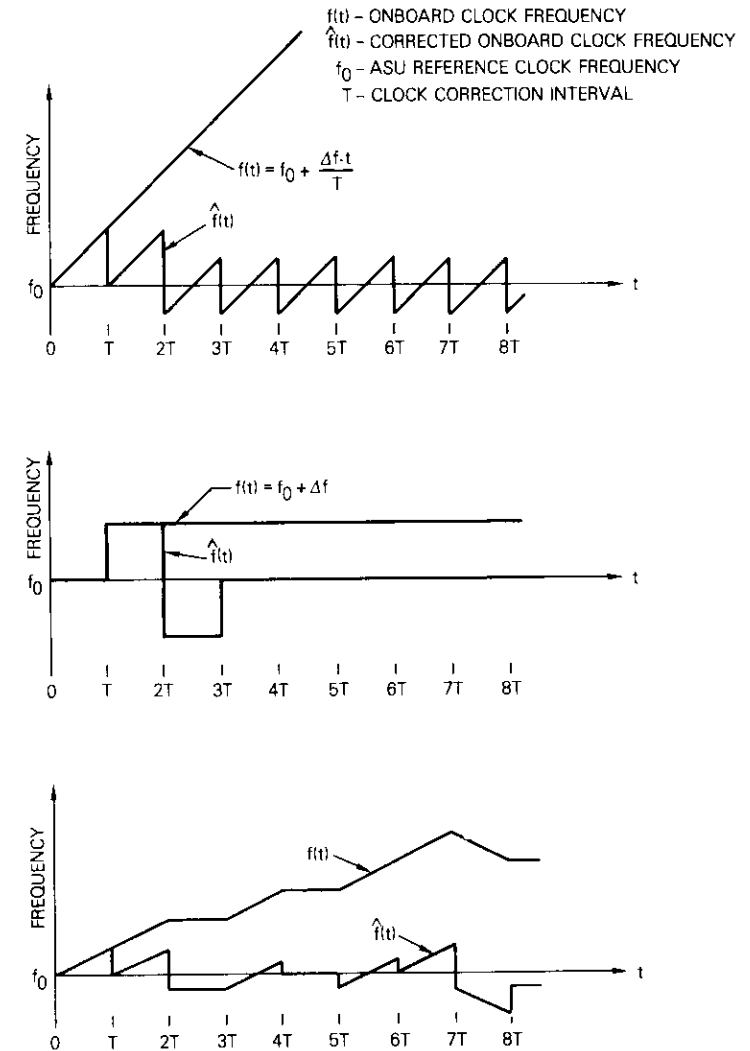
Figure 3. *Examples of Clock Correction*

The parameter bounds given above may apply for any clock drift rate that does not exceed $\Delta\rho_s$ over any T second interval. However, a clock drifts almost linearly with time over a short period, *i.e.*, several hours. In this case, better upper bounds may be obtained on the system

parameters. According to Appendix E, the parameter bounds for a piecewise linear clock drift rate are given by

long-term phase error: $|s_n| \leq \Delta\rho_s T$ (6a)

cumulative phase error: $|y_n| \leq \Delta\rho_s T$ (6b)

incremental clock correction: $|u_n| \leq 2\Delta\rho_s$ (6c)

clock correction error: $|(\rho_s)_n - w_n| \leq \Delta\rho_s$ (6d)

buffer size: $4\Delta\rho_s T$ (6e)

The next examples will illustrate typical buffer size requirements. The worst-case clock drift is specified as one part in $10^{10}/10$ min, and the correction period is $T = 3$ hr. Since a drift rate may be regarded as a linear function of time over 3 hr, $\Delta\rho_s = 1.8 \times 10^{-9}$ and the buffer size is $4\Delta\rho_s T = 78$ μs. The second example assumes a timing inaccuracy of $\Delta\rho_s = 10^{-9}$ for a sidereal day of 86,160 s. If the clock correction interval is every sidereal day, the buffer size requirement will be $6\Delta\rho_s T = 517$ μs for the worst case. If the drift is at a constant rate, then the buffer size becomes 345 μs.

Doppler shift

The measured phase error s_n contains not only the clock drift but also the term due to Doppler shift. Since the discrete system model shown in Figure 2 is linear, the effects of Doppler shift can be expressed by equations (5a) through (5e), with $\Delta\rho_s$ being replaced by $\Delta\rho_u$, where $\Delta\rho_u$ is the worst-case Doppler shift averaged over a correction period T. Typical values of $\Delta\rho_u$ which illustrate Doppler effects are discussed below.

The INTELSAT V stationkeeping maintains satellite position within $\pm0.1°$ longitude, and $\pm0.1°$ inclination for the first several years and $\pm0.5°$ thereafter. The eccentricity of the orbit is no greater than 0.0005. With these orbital parameter accuracies, the short-term (instantaneous) Doppler shift is 2×10^{-8} in the worst case, and $\Delta\rho_u$ is approximately equal to this value for a small T. However, $\Delta\rho_u$ can be made quite small if a sidereal day clock correction is chosen.

The Doppler shift averaged over a sidereal day would be zero if the satellite motion were perfectly periodic with a sidereal day period. Thus, sidereal day corrections would result in a constant onboard clock frequency. However, because the satellite exhibits a long-term

east-west drift and inclination change, it does not return to the same point each sidereal day. For instance, the worst-case longitudinal acceleration is about $0.002°/\text{day}^2$, which results in a drift rate of $0.028°/\text{day}$ for the east-west stationkeeping of $\pm0.1°$. The effect of this longitudinal drift on the range variation is 3.12 km/day, or equivalently, an average Doppler shift of 1.2×10^{-10}. On the other hand, the orbital inclination changes $0.005°/\text{day}$, which contributes to the satellite range variation of 0.557 km/day or an average Doppler shift of 2.2×10^{-11}. The combined effect of the two orbital components produces a long-term Doppler shift no greater than 1.5×10^{-10}. Thus, $\Delta\rho_u = 1.5 \times 10^{-10}$ for $T = 86,160$ s.

Stationkeeping maneuvers introduce relatively large Doppler effects. The north-south position correction reverses the inclination angle from one extreme to the other over a 5-day period. Since the maximum range variation due to orbital inclination is ±55.7 km for the inclination angle of $\pm0.5°$, a maneuver causes an average daily range change of 22.3 km. Considering longitudinal drift, the total range variation becomes 25.4 km, with a corresponding Doppler shift of 9.8×10^{-10}.

The east-west stationkeeping maneuver simultaneously corrects the longitudinal drift and eccentricity, and a maneuver requires only a few minutes. This orbit correction does not increase the daily range variation of 3.12 km in the east-west motion. However, the eccentricity may vanish as a result of longitudinal maneuvers. This implies a change in eccentricity from 0.0005 to 0, causing a range variation of 21.8 km in an extreme case. The combined effect in the range variation is then 25.5 km/day and $\Delta\rho_u = 9.9 \times 10^{-10}$.

From the above discussion, the contribution of Doppler shift to the clock correction accuracy is approximately $\Delta\rho_u = 10^{-9}$ in the worst case, and can be compensated by a traffic station buffer requirement of $6\Delta\rho_u T$ (517 μs).

Another means of removing the influence of long-term Doppler on the onboard clock involves periodic range measurement. Suppose that $r(t)$ denotes the range measured by the ASU at time t. The one-way signal propagation time to the satellite is then $r(t)/c$, where c is the velocity of light. The up-link Doppler shift is the change in propagation time measured over the incremental time Δt:

$$\rho_u(t) = \lim_{\Delta t \to 0} \frac{1}{\Delta t} \left[\frac{r(t + \Delta t)}{c} - \frac{r(t)}{c} \right] = \frac{1}{c} \frac{dr(t)}{dt} \quad .   (7)$$

The long-term Doppler shift of the nth correction interval is the average value of $\rho_u(t)$:

$$
\begin{aligned}
(\rho_u)_n &= \frac{1}{T} \int_{(n-1)T}^{nT} \rho_u(t)\, dt \\
&= \frac{1}{Tc}\{r(nT) - r[(n-1)T]\} \qquad (8) \\
&= \frac{1}{Tc} \times (\text{range variation}) \quad .
\end{aligned}
$$

Therefore, the long-term Doppler shift can be calculated from periodic range measurements. Subtracting this term from s_n eliminates the Doppler effect from the clock correction scheme. The range measurement can easily be performed using metering bursts which, incidentally, must be transmitted to the satellite for onboard clock synchronization.

The error resulting from a range measurement can be as large as ± 10 symbols at a symbol rate of 60 Mbaud. However, any fixed-error term, such as a calibration error, vanishes in the range variation calculation, which results in a measurement error not exceeding ± 3 symbols or ± 50 ns. The effect on the onboard clock correction is quite small, an equivalent clock drift rate of 5.8×10^{-13} for $T = 86,160$ s.

Quantization error

The incremental clock correction u_n is quantized into a finite level and sent to the satellite as a binary number. The quantization step size, denoted by e, causes an inherent inaccuracy of the onboard clock correction. The quantization error is $e/2$ or e depending upon whether rounded or truncated numbers are used. (Assume the former value in the following calculation since it yields a smaller error.) Appendix F analyzes the quantization effect, and the results are shown below:

$$\text{long-term phase error: } |s_n| \leq eT \qquad (9a)$$

$$\text{cumulative phase error: } |y_n| \leq \tfrac{1}{2}eT \qquad (9b)$$

$$\text{incremental clock correction: } |u_n| \leq \frac{3e}{2} \qquad (9c)$$

$$\text{clock correction error: } |w_n| \leq e \qquad (9d)$$

$$\text{buffer size: } 4eT \quad . \qquad (9e)$$

These errors result from the quantization process and should be added to the quantities discussed previously.

Delayed incremental clock correction

The incremental clock correction u_n is likely to be transmitted to the satellite via the telemetry, tracking, and command (TT&C) station. If the information transfer is in real time, the correction datum, u_n, may experience a few seconds of transmission delay to reach the satellite. In this case, there will be negligible performance degradation due to the clock correction updating delay. However, a problem may arise if this delay exceeds a few minutes because of the unavailability of the command link. Appendix G analyzes the effect caused by a fixed updating delay.

The system remains stable as long as each clock correction is made within $\Delta T = 0.382T$ after a long-term phase error measurement and becomes unstable when it exceeds this value in every correction interval. Based on the analysis in Appendix G, the increase in parameter bound is plotted as a function of $\Delta T/T$ in Figure 4, where ΔT is the delay incurred in transferring incremental clock correction data. This figure also shows the simulation results performed on 6,000 correction intervals. The theoretical bound may be regarded as the worst-case parameter value increase.

To illustrate, let $T = 1$ sidereal day. If every clock correction is made within 5 min after a phase error measurement ($\Delta T/T = 0.0035$), the parameter bound increase will be about 2.1 percent; that is, a traffic station requires 2.1 percent more buffer due to the clock correction updating delay of 5 min. Other parameter bounds are also increased by the same amount. This increase is almost linear for a delay of less than 2.4 hr and accelerates as the delay approaches 9.14 hr.

Numerical example

The clock accuracy requirement for the INTELSAT plesiochronous system does not allow the worst-case drift to exceed one part in 10^{11}. However, the onboard clock may drift up to one part in 10^9 per day and have a total departure of one part in 10^6 at the end of satellite life. An incremental clock correction datum is quantized into an integer number with a quantizing step of 10^{-10} and sent to the satellite once every sidereal day. The maximum allowable delay of the correction datum is 5 min. Table 1 is tabulated under these assumptions; the
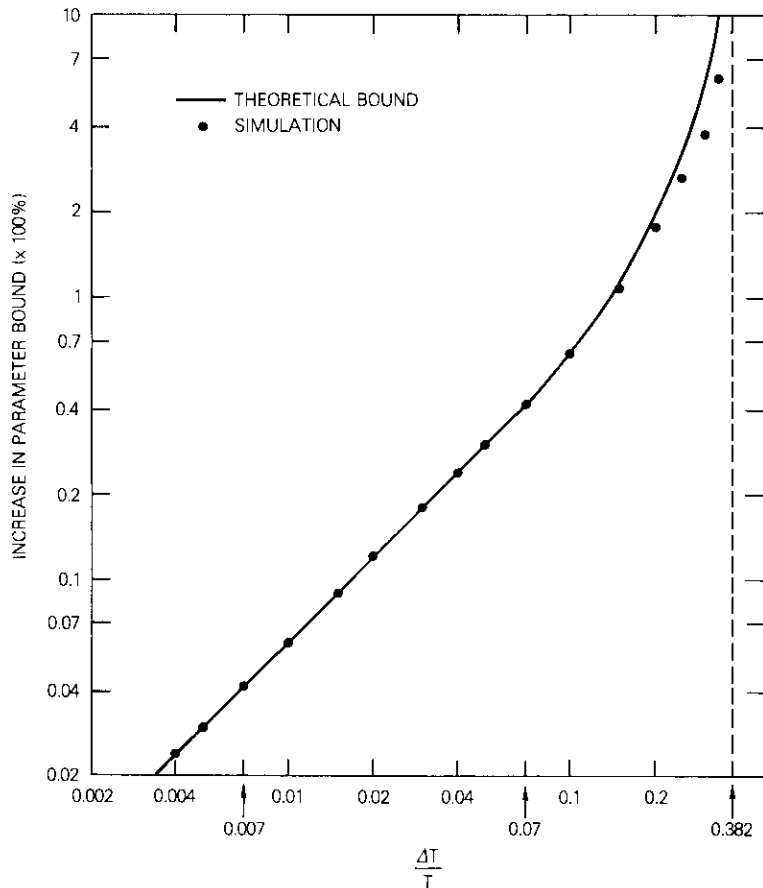
Figure 4. *Increase in Parameter Bound for Delayed Clock Correction*

parameter values do not contain a Doppler effect. A 5-min delay in the incremental clock correction increases the worst-case parameter values by about 2.1 percent. This increase applies not only to the basic error term but also to the quantization error term, since a quantization error results in an additional clock correction error. The required buffer size at a traffic station is 563 μs for this example.

The long-term (1 sidereal day) Doppler shift is 10^{-9} in the worst case. If the Doppler component is not eliminated from the long-term

TABLE 1. TIMING ERROR SOURCES AND PARAMETER BOUNDS

Timing Error Source	$|x_n|$ (μs)	$|y_n|$ (μs)	$|u_n|$	$w_n - (\rho_s)_n|$	Buffer Size (μs)
Basic Error Term	173	86	3×10^{-9}	2×10^{-9}	517
Quantization Error	9	4	1.5×10^{-10}	1×10^{-10}	34
Delayed Clock Correction (up to 5 min)	4	2	6.6×10^{-11}	4.4×10^{-11}	12
Worst-Case Value	186	92	3.2×10^{-9}	2.1×10^{-9}	563

phase error measurement, the required buffer size will be about 1,126 μs, although this value is worst case and may be conservative.

Clock correction for baseband processing satellite

In a baseband processing satellite, the onboard clock also provides the timing for the baseband processing functions such as burst processing, data demultiplexing, filtering, and remultiplexing for retransmission to the designated down-link beams. Figure 5 is a diagram of
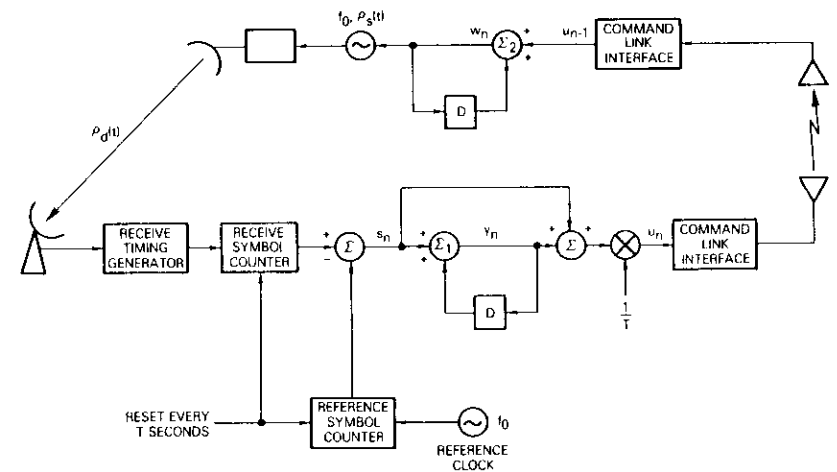
Figure 5. *Onboard Clock Correction Diagram for Baseband Processing Satellite*

onboard clock correction for a baseband processing satellite, where the down-link beam is a continuous TDM signal. The long-term phase error s_n, which is the accumulated timing error of the recovered symbol clock over T seconds measured relative to the high-accuracy ground reference clock, contains a long-term down-link Doppler shift that may be eliminated by calculating the range variation, if necessary. The only difference between this clock correction scheme and the one for an ss/TDMA system is a type of Doppler shift, *i.e.*, down-link Doppler *vs* up-link Doppler. The previous analyses and discussions also may be applied to this case.

Conclusion

An onboard clock correction scheme for an SS/TDMA system is proposed and a detailed analysis is performed, including secondary timing error sources. The basic clock correction scheme may be used with minor modifications for other communications satellites, including baseband processing and scanning beam satellites, where the onboard clock provides the basic timing for switching and/or processing functions. The proposed scheme is particularly effective if the Doppler component is eliminated and the clock correction delay is minimized.

Special attention is focused on a sidereal day clock correction. Based on INTELSAT V stationkeeping accuracy, the buffer size needed to accommodate frequency changes due to the clock control is 563 µs with ranging compensation, and 1,126 µs without it. These values assume a maximum clock correction delay of 5 min.

References

[1] S. J. Campanella, "Synchronization of SS/TDMA Onboard Clocks," International Telemetry Conference, San Diego, California, October 1980.

[2] Private communication with R. Colby.

[3] R. A. Rapuano and N. Shimasaki, "Synchronization of Earth Stations to Satellite-Switched Sequences," AIAA 4th Communications Satellite Systems Conference, Washington, D.C., 1972.

[4] M. Asahara et al., "Synchronization and Acquisition in SDMA Satellite Communication System," ICC'74, Minneapolis, Minnesota, 1974.

[5] C. R. Carter, "Survey of Synchronization Techniques for a TDMA Satellite-Switched System," *IEEE Transactions on Communications*, Vol. COM-28, No. 8, pp. 1291–1301, August 1980.

Appendix A.   Long-term phase error

Let $t_{n-1} = (n-1)T$ and $t_n = nT$. Then

$$s_n = \int_{t_{n-1}}^{t_n} \frac{[f_s(t)[1 - \rho_u(t)] - f_0]}{f_0} \, dt$$

$$\cong \int_{t_{n-1}}^{t_n} [\rho_s(t) - \rho_u(t) - w_n] \, dt \qquad (\text{A-1})$$

$$= (\rho_s)_n T - (\rho_u)_n T - w_n T$$

where

$$(\rho_s)_n = \frac{1}{T} \int_{t_{n-1}}^{t_n} \rho_s(t) \, dt \qquad (\text{A-2})$$

and

$$(\rho_u)_n = \frac{1}{T} \int_{t_{n-1}}^{t_n} \rho_u(t) \, dt \quad . \qquad (\text{A-3})$$

Appendix B.   Analysis of onboard clock drift

Let $S(z)$, $Y(z)$, $U(z)$, $W(z)$, and $R(z)$ denote the Z-transforms of s_n, y_n, u_n, w_n, and $(\rho_s)_n$, respectively. From Figure 2,

$$S(z) = T\left[R(z) - \left(\frac{1}{1 - z^{-1}} \right) \cdot z^{-1} \cdot \frac{1}{T} \cdot \left(1 + \frac{1}{1 - z^{-1}} \right) S(z) \right]$$

$$= T\left[R(z) - \frac{1}{T} \cdot \frac{z^{-1}(2 - z^{-1})}{(1 - z^{-1})^2} \cdot S(z) \right] \quad . \qquad (\text{B-1})$$

Thus,

$$S(z) = T(1 - z^{-1})^2 R(z) \qquad (\text{B-2a})$$

$$Y(z) = \left(\frac{1}{1 - z^{-1}} \right) S(z) = T(1 - z^{-1})R(z) \qquad (\text{B-2b})$$

$$U(z) = \frac{1}{T}\left(1 + \frac{1}{1 - z^{-1}} \right) S(z) = (2 - z^{-1})(1 - z^{-1})R(z) \qquad (\text{B-2c})$$

$$W(z) = \left(\frac{z^{-1}}{1 - z^{-1}} \right) U(z) = z^{-1}(2 - z^{-1})R(z) \quad . \qquad (\text{B-2d})$$

The corresponding time domain expressions are

$$s_n = [(\rho_s)_n - 2(\rho_s)_{n-1} + (\rho_s)_{n-2}]T \tag{B-3a}$$

$$y_n = [(\rho_s)_n - (\rho_s)_{n-1}]T \tag{B-3b}$$

$$u_n = 2(\rho_s)_n - 3(\rho_s)_{n-1} + (\rho_s)_{n-2} \tag{B-3c}$$

$$w_n = 2(\rho_s)_{n-1} - (\rho_s)_{n-2} \quad . \tag{B-3d}$$

Appendix C.   Calculation of $|(\rho_s)_n - (\rho_s)_{n-1}|$

Let $t_i = iT$, where i is an integer.

$$
\begin{aligned}
|(\rho_s)_n - (\rho_s)_{n-1}| &= \frac{1}{T}\left| \int_{t_{n-1}}^{t_n} \rho_s(t)\, dt - \int_{t_{n-2}}^{t_{n-1}} \rho_s(t)\, dt \right| \\
&= \frac{1}{T}\left| \int_{t_{n-2}}^{t_{n-1}} [\rho_s(t+T) - \rho_s(t)]\, dt \right| \tag{C-1} \\
&\leq \frac{1}{T} \int_{t_{n-2}}^{t_{n-1}} |\rho_s(t+T) - \rho_s(t)|\, dt \quad .
\end{aligned}
$$

Since $|\rho_s(t+T) - \rho_s(t)| \leq \Delta\rho_s$ for any t, the equation may be simplified as follows:

$$
\begin{aligned}
|(\rho_s)_n - (\rho_s)_{n-1}| &\leq \frac{1}{T} \int_{t_{n-2}}^{t_{n-1}} \Delta\rho_s\, dt \\
&= \Delta\rho_s \quad . \tag{C-2}
\end{aligned}
$$

Appendix D.   Calculation of buffer size

The instantaneous timing error of a reference burst received by a traffic station is the sum of the onboard clock correction error and the down-link Doppler shift, *i.e.*,

$$\rho(t) = \rho_s(t) - w_n - \rho_d(t) \tag{D-1}$$

where $\rho_d(t)$ is the Doppler shift of a signal traveling from the satellite to the traffic station at time t, where $t_{n-1} \leq t < t_n$. If the timing error at the traffic station is set to zero at $t = 0$, the accumulated timing error at time t is

$$
\begin{aligned}
\Delta t &= \int_0^t \rho(\tau)\, d\tau \\
&= \sum_{i=1}^{n-1} \int_{t_{i-1}}^{t_i} [\rho_s(\tau) - w_i]\, d\tau + \int_{t_{n-1}}^{t} [\rho_s(\tau) - w_n]\, d\tau \tag{D-2} \\
&\quad - \int_0^t \rho_d(\tau)\, d\tau \quad .
\end{aligned}
$$

The last term does not exceed one-half of the worst-case timing error resulting from a round-trip Doppler shift. Since traffic stations possess a Doppler buffer, this term may be deleted from the buffer size calculation caused by the clock correction error.

The first $n - 1$ terms can be simplified as follows:

$$
\begin{aligned}
\sum_{i=1}^{n-1} \int_{t_{i-1}}^{t_i} [\rho_s(\tau) - w_i]\, d\tau & \\
&= \sum_{i=1}^{n-1} [(\rho_s)_i - w_i]T \\
&= \sum_{i=1}^{n-1} [(\rho_s)_i - 2(\rho_s)_{i-1} + (\rho_s)_{i-2}]T \\
&= [(\rho_s)_{n-1} - (\rho_s)_{n-2}]T - [(\rho_s)_0 - (\rho_s)_{-1}]T \quad . \tag{D-3}
\end{aligned}
$$

The second term of the equation is a fixed timing error, which may be eliminated at the initialization stage of the traffic station operation. The ASU can calculate this timing offset at any given time by summing the long-term phase error s_n and cumulative phase error y_n, and subtracting a Doppler shift component if its contribution is not negligible.

Thus, equation (D-2) may be rewritten as follows:

$$\Delta t = [(\rho_s)_{n-1} - (\rho_s)_{n-2}]T + \int_{t_{n-1}}^{t} [\rho_s(\tau) - w_n]\, d\tau \quad . \tag{D-4}$$

If $\rho_s(\tau) - w_n$ is a nonnegative or nonpositive function in the interval $[t_{n-1}, t_n]$, then either

$$[(\rho_s)_{n-1} - (\rho_s)_{n-2}]T \leq \Delta t \leq [(\rho_s)_n - (\rho_s)_{n-1}]T \tag{D-5}$$

or

$$[(\rho_s)_n - (\rho_s)_{n-1}]T \leq \Delta t \leq [(\rho_s)_{n-1} - (\rho_s)_{n-2}]T \quad . \tag{D-6}$$

From Appendix C, $|\Delta t| \leq \Delta\rho_s T$ for either case. If the above is not true, then Δt becomes maximum or minimum at some $\tau_0 \epsilon [t_{n-1}, \ t_n]$ and $\rho_s(\tau_0) = w_n$. Therefore,

$$|\Delta t| \leq |(\rho_s)_{n-1} - (\rho_s)_{n-2}|T + \int_{t_{n-1}}^{\tau_0} |\rho_s(\tau) - w_n| \, d\tau \quad \text{(D-7)}$$

$$\leq \Delta\rho_s T + \int_{t_{n-1}}^{t_{n-1}+\Delta T} |\rho_s(\tau) - w_n| \, d\tau$$

where $\Delta T = \tau_0 - t_{n-1}$. Suppose that $\Delta T \leq T/2$. Since $|\rho_s(\tau) - w_n| \leq \Delta\rho_s$ for $t_{n-1} \leq \tau \leq \tau_0$, the equation is reduced to

$$|\Delta t| \leq \Delta\rho_s T + \Delta\rho_s \Delta T \leq \tfrac{3}{2} \Delta\rho_s T \quad . \quad \text{(D-8)}$$

Now, suppose that $T/2 < \Delta T < T$. Then,

$$\Delta t = [(\rho_s)_{n-1} - (\rho_s)_{n-2}]T + [(\rho_s)_n - w_n]T$$

$$- \int_{t_{n-1}+\Delta T}^{t_n} [\rho_s(\tau) - w_n] \, d\tau \quad \text{(D-9)}$$

$$= [(\rho_s)_n - (\rho_s)_{n-1}]T - \int_{t_{n-1}+\Delta T}^{t_n} [\rho_s(\tau) - w_n] \, d\tau \quad .$$

Since $|\rho_s(\tau) - w_n| \leq \Delta\rho_s$ for $t_{n-1} + \Delta T \leq \tau \leq t_n$, the same bound (equation D-8) is obtained:

$$|\Delta t| \leq \Delta\rho_s T + \Delta\rho_s (T - \Delta T) \leq \tfrac{3}{2} \Delta\rho_s T \quad . \quad \text{(D-10)}$$

Accordingly, the required receive buffer size at a traffic station is $3\Delta\rho_s T$, which is twice the worst-case timing error.

The transmit buffer size may be calculated similarly and is given by $3\Delta\rho_s T$, resulting in the total traffic station buffer size of $6\Delta\rho_s T$.

Appendix E.   Piecewise linear clock drift

A piecewise linear clock drift rate is characterized with the next equation:

$$\rho_s(t) = \rho_s(t_{n-1}) + \alpha_{n-1}(t - t_{n-1}) \quad \text{(E-1)}$$

where $t_{n-1} \leq t \leq t_n = t_{n-1} + T$ and $|\alpha_{n-1}| \leq \Delta\rho_s/T$. Then,

$$(\rho_s)_n = \frac{1}{T} \int_{t_{n-1}}^{t_n} \rho_s(t) \, dt \quad \text{(E-2)}$$

$$= \rho_s(t_{n-1}) + \tfrac{1}{2}\alpha_{n-1}T$$

and

$$\rho_s(t_n) = \rho_s(t_{n-1}) + \alpha_{n-1}T \quad . \quad \text{(E-3)}$$

Using these relations in the time domain expressions in Appendix B, the following worst-case values are obtained:

$$s_n = \tfrac{1}{2}(\alpha_{n-1} - \alpha_{n-3})T^2, \ |s_n| \leq \Delta\rho_s T \quad \text{(E-4a)}$$

$$y_n = \tfrac{1}{2}(\alpha_{n-1} + \alpha_{n-2})T^2, \ |y_n| \leq \Delta\rho_s T \quad \text{(E-4b)}$$

$$u_n = \tfrac{1}{2}(2\alpha_{n-1} + \alpha_{n-2} - \alpha_{n-3})T, \ |u_n| \leq 2\Delta\rho_s \quad \text{(E-4c)}$$

$$(\rho_s)_n - w_n = \tfrac{1}{2}(\alpha_{n-1} - \alpha_{n-3})T, \ |(\rho_s)_n - w_n| \leq \Delta\rho_s \quad . \quad \text{(E-4d)}$$

The timing error (or buffer size) calculation follows easily from equation (D-4). Let $t = t_{n-1} + \Delta T$, where $0 \leq \Delta T \leq T$:

$$\Delta t = T[(\rho_s)_{n-1} - (\rho_s)_{n-2}] + \int_{t_{n-1}}^{t_{n-1}+\Delta T} [\rho_s(\tau) - w_n] \, d\tau$$

$$= \Delta T(T + \tfrac{1}{2}\Delta T)\alpha_{n-1} + \tfrac{1}{2}T^2 \alpha_{n-2} + \tfrac{1}{2}T(T - 3\Delta T)\alpha_{n-3} \quad . \quad \text{(E-5)}$$

The worst-case value is then

$$|\Delta t| \leq \Delta T(T + \tfrac{1}{2}\Delta T)\frac{\Delta\rho_s}{T} + \tfrac{1}{2}T\Delta\rho_s + \tfrac{1}{2}(T - 3\Delta T)\Delta\rho_s$$

$$= \left(T + \frac{\Delta T^2}{2T} - \frac{\Delta T}{2} \right)\Delta\rho_s \quad \text{(E-6)}$$

$$\leq \Delta\rho_s T \quad .$$

Accordingly, the required buffer size is $4\Delta\rho_s T$ for a piecewise linear clock drift, i.e., $2\Delta\rho_s T$ for transmit and receive sides.

Appendix F.   Quantization error analysis

Let $(\rho_s)_n = (\rho_u)_n = 0$ in Figure 2. Then,

$$S(z) = -T\left(\frac{z^{-1}}{1 - z^{-1}}\right)\left[E(z) + \frac{1}{T}\left(1 + \frac{1}{1 - z^{-1}}\right)S(z)\right]$$

$$= -T\left(\frac{z^{-1}}{1 - z^{-1}}\right)\left[E(z) + \frac{1}{T}\left(\frac{2 - z^{-1}}{1 - z^{-1}}\right)S(z)\right]$$

(F-1)

where $E(z)$ is the Z-transform of e_n. Solving this equation for $S(z)$ yields the following solutions:

$$S(z) = -Tz^{-1}(1 - z^{-1})E(z)$$ (F-2a)

$$Y(z) = -Tz^{-1}E(z)$$ (F-2b)

$$U(z) = -z^{-1}(2 - z^{-1})E(z)$$ (F-2c)

$$W(z) = z^{-1}(1 - z^{-1})E(z)$$ (F-2d)

The quantization error is $|e_n| \leq e/2$ for a rounded number. The time domain expressions and their worst-case values are given in the following:

$$s_n = -T(e_{n-1} - e_{n-2}), \quad |s_n| \leq eT$$ (F-3a)

$$y_n = -Te_{n-1}, \quad |y_n| \leq \tfrac{1}{2}eT$$ (F-3b)

$$u_n = -2e_{n-1} + e_{n-2}, \quad |u_n| \leq \frac{3e}{2}$$ (F-3c)

$$w_n = e_{n-1} - e_{n-2}, \quad |w_n| \leq e \quad .$$ (F-3d)

The buffer requirement due to the quantization error can be calculated from the equation in Appendix D:

$$4|\Delta t| = 4\left|T\sum_{i=1}^{n}(-w_i)\right|$$

$$= 4T\left|\sum_{i=1}^{n}(-e_{i-1} + e_{i-2})\right|$$

$$= 4T\left|-e_{n-1} + e_{-1}\right|$$

$$\leq 4eT \quad .$$

(F-4)

Appendix G.   Effect of delayed clock correction

Let ΔT be the delay incurred in transferring an incremental clock correction to the satellite. (Assume that $0 \leq \Delta T < T$.) The clock correction in the nth interval is characterized by the following function:

$$w_n'(t) = \begin{cases} w_{n-1}, & t_{n-1} \leq t < t_{n-1} + \Delta T \\ w_n, & t_{n-1} + \Delta T \leq t \leq t_n \end{cases}$$ (G-1)

where $w_n = w_{n-1} + u_{n-1}$ and $t_i = iT$. The new long-term phase error then becomes

$$s_n = \int_{t_{n-1}}^{t_n} [\rho_s(t) - w_n'(t)]\, dt$$

$$= T\left[(\rho_s)_n - \left(\frac{\Delta T}{T}\right)w_{n-1} - \left(\frac{T - \Delta T}{T}\right)w_n\right]$$ (G-2)

$$= T[(\rho_s)_n - dw_{n-1} - (1 - d)w_n]$$

where $d = \Delta T/T$ is a normalized delay. The discrete system model shown in Figure G-1 is used to obtain the Z-domain expressions:

$$S(z) = \frac{T(1 - z^{-1})^2}{D(z)}R(z)$$ (G-3a)

$$Y(z) = \frac{T(1 - z^{-1})}{D(z)}R(z)$$ (G-3b)

$$U(z) = \frac{(2 - z^{-1})(1 - z^{-1})}{D(z)}R(z)$$ (G-3c)

$$W(z) = \frac{z^{-1}(2 - z^{-1})}{D(z)}R(z)$$ (G-3d)

where $D(z) = 1 - dz^{-1}(1 - z^{-1})(2 - z^{-1})$. Before the corresponding time domain expressions are derived, the stability analysis is performed.

The poles of the transfer functions are the roots of the following equation:

$$D(z) = 1 - dz^{-1}(1 - z^{-1})(2 - z^{-1}) = 0 \quad .$$ (G-4)

Equation (G-4) can be rewritten as follows:

$$z^3 - 2dz^2 + 3dz - d = 0 \quad .$$ (G-5)

Figure G-1. *Discrete System Model for Delayed Clock Correction*

This third-order polynomial equation has the following roots:

$$z_1 = \frac{1}{1 + p^{1/3} + q^{1/3}} \qquad \text{(G-6a)}$$

$$z_2 = \frac{1}{1 - \frac{1}{2}p^{1/3} - \frac{1}{2}q^{1/3} + i\frac{\sqrt{3}}{2}(p^{1/3} - q^{1/3})} \qquad \text{(G-6b)}$$

$$z_3 = \frac{1}{1 - \frac{1}{2}p^{1/3} - \frac{1}{2}q^{1/3} - i\frac{\sqrt{3}}{2}(p^{1/3} - q^{1/3})} \qquad \text{(G-6c)}$$

where $i = \sqrt{-1}$ and

$$p = \frac{1}{2}\left(\frac{1}{d} + \sqrt{\frac{1}{d^2} - \frac{4}{27}}\right)$$

$$q = \frac{1}{2}\left(\frac{1}{d} - \sqrt{\frac{1}{d^2} - \frac{4}{27}}\right) \quad .$$

For a stable system, $|z_k| \le 1$ for $1 \le k \le 3$. It is obvious that $|z_1| < 1$ for $0 < d < 1$. The stability conditions for the other two poles are

$$|z_2|^2 = |z_3|^2 \le 1$$

or

$$p^{2/3} + q^{2/3} \ge p^{1/3} + q^{1/3} + (pq)^{1/3} \quad .$$

The solution to this inequality is

$$d \le \frac{4}{(1 + \sqrt{5})^2} \cong 0.38197 \quad . \qquad \text{(G-7)}$$

Thus, the clock correction scheme becomes unstable if the updating delay exceeds $\Delta T = 0.38197T$, which is 9 hr, 8 min, and 31 s for $T = 86,160$ s (1 sidereal day).

To derive the time domain expressions, let $a = p^{1/3} + q^{1/3}$ and $b = p^{1/3} - q^{1/3}$. First, term $1/D(z)$ is calculated as follows:

$$\frac{1}{D(z)} = \frac{1}{(1 - z_1z^{-1})(1 - z_2z^{-1})(1 - z_3z^{-1})}$$

$$= \frac{A}{1 - z_1z^{-1}} + \frac{B}{1 - z_2z^{-1}} + \frac{C}{1 - z_3z^{-1}}$$

where

$$A = \frac{1}{(1 - z_2z_1^{-1})(1 - z_3z_1^{-1})} = \frac{(2 - a)^2 + 3b^2}{3(3a^2 + b^2)}$$

$$B = \frac{1}{(1 - z_1z_2^{-1})(1 - z_3z_2^{-1})}$$

$$= \frac{a + 1}{3b(3a^2 + b^2)}[2b(2a - 1) + i\sqrt{3}(-a^2 + 2a + b^2)]$$

$$C = \text{complex conjugate of B} \quad .$$

A series expansion of the above equation results in the following form:

$$\frac{R(z)}{D(z)} = \sum_{n=0}^{\infty} (Az_1^n + Bz_2^n + Cz_3^n)z^{-n} \sum_{k=0}^{\infty}(\rho_s)_k z^{-k} \qquad \text{(G-8)}$$

$$= \sum_{n=0}^{\infty} \beta_n z^{-n}$$

where β_n is given by

$$\beta_n = \sum_{k=0}^{n} (Az_1^{n-k} + Bz_2^{n-k} + Cz_3^{n-k})(\rho_s)_k \quad .$$

The parameter values are now expressed in terms of β_n:

$$s_n = (\beta_n - 2\beta_{n-1} + \beta_{n-2})T \tag{G-9a}$$

$$y_n = (\beta_n - \beta_{n-1})T \tag{G-9b}$$

$$u_n = 2\beta_n - 3\beta_{n-1} + \beta_{n-2} \tag{G-9c}$$

$$w_n = 2\beta_{n-1} - \beta_{n-2} \quad . \tag{G-9d}$$

These solutions are similar to those obtained earlier for nondelayed clock correction, and the parameter bounds are determined by the worst-case value of $|\beta_n - \beta_{n-1}|$, which is estimated in the following:

$$\begin{aligned}
\beta_n - \beta_{n-1} &= \sum_{k=0}^{n} (Az_1^{n-k} + Bz_2^{n-k} + Cz_3^{n-k})(\rho_s)_k \\
&\quad - \sum_{k=0}^{n-1} (Az_1^{n-k-1} + Bz_2^{n-k-1} + Cz_3^{n-k-1})(\rho_s)_k \\
&= \sum_{k=1}^{n} (Az_1^{n-k} + Bz_2^{n-k} + Cz_3^{n-k})[(\rho_s)_k - (\rho_s)_{k-1}] \\
&\quad + (Az_1^n + Bz_2^n + Cz_3^n)(\rho_s)_0 \quad .
\end{aligned} \tag{G-10}$$

If $d < 0.38197$ (or $|z_1|, |z_2|, |z_3| < 1$), the last term vanishes in the steady state. Since $A + B + C = 1$, an upper bound of $|\beta_n - \beta_{n-1}|$ is given by

$$|\beta_n - \beta_{n-1}| \le \left[1 + \sum_{k=1}^{n-1} |Az_1^{n-k} + Bz_2^{n-k} + Cz_3^{n-k}| \right] \Delta\rho_s \quad .$$

The first term $\Delta\rho_s$ is the basic error component resulting from the differential clock drift rate, $(\rho_s)_n - (\rho_s)_{n-1}$, of the nth interval. The second term is the increase in timing inaccuracy due to the delayed incremental clock correction. The worst-case parameter values will be increased by the amount determined by this term relative to the nondelayed clock correction. Let ϵ_n denote the normalized parameter increase, i.e.,

$$\epsilon_n = \sum_{k=1}^{n-1} |Az_1^{n-k} + Bz_2^{n-k} + Cz_3^{n-k}| \quad . \tag{G-11}$$

Let $B = R_1 \exp(i\theta_1)$ and $z_2 = R_2 \exp(i\theta_2)$, where

$$R_1 = \frac{a+1}{3b(3a^2 + b^2)} [4b^2(2a-1)^2 + 3(-a^2 + 2a + b^2)^2]^{1/2} \tag{G-12a}$$

$$\theta_1 = \tan^{-1} \left[\frac{\sqrt{3}(-a^2 + 2a + b^2)}{2b(2a-1)} \right] \tag{G-12b}$$

$$R_2 = \frac{2}{[(2-a)^2 + 3b^2]^{1/2}} \tag{G-12c}$$

$$\theta_2 = \tan^{-1} \left(\frac{-\sqrt{3}b}{2-a} \right) \quad . \tag{G-12d}$$

Since Cz_3^{n-k} is the complex conjugate of Bz_2^{n-k}, the equation may be written as follows:

$$\begin{aligned}
\epsilon_n &= \sum_{k=1}^{n-1} |Az_1^k + 2R_1R_2^k \cos(k\theta_2 + \theta_1)| \\
&\le \sum_{k=1}^{\infty} |Az_1^k + 2R_1R_2^k \cos(k\theta_2 + \theta_1)| = \epsilon \quad .
\end{aligned} \tag{G-13}$$

The increase in parameter bound, ϵ, is plotted in Figure 4 as a function of normalized delay, d, along with simulation results.

Thomas Inukai received B.S. and M.S. degrees in communications engineering from the Tokyo Electrical Engineering College, and a Ph.D. degree in electrical engineering from the City University of New York, in 1967, 1970, and 1975, respectively. Prior to joining COMSAT in 1979, he was with Western Union Telegraph Company where he was involved in SS-TDMA systems studies, and with North Electric Company where he was responsible for the development of digital signal processing software. Currently, he is a member of the technical staff in the Multiple Access Department at COMSAT Laboratories, where he is engaged in research and development activities for future INTELSAT and domestic satellite communications systems. Dr. Inukai is a member of IEEE, the American Mathematical Society, and Sigma Xi.

S. J. Campanella received a B.S.E.E. from the Catholic University of America, an M.S.E.E. from the University of Maryland, and a Ph.D. in electrical engineering from the Catholic University of America. Before joining COMSAT, he was Manager of the Electronics Research Center at Melpar, Inc. and prior to Melpar, Inc. an Electronic Scientist at the Naval Research Laboratories.

He is presently Executive Director of Communications Technology at COMSAT Laboratories. He has recently been responsible for the technical direction of the INTELSAT TDMA field trials in the Atlantic Coast Region.

Dr. Campanella is a Member of AIAA, Sigma Xi, Phi Eta Sigma, and a Fellow of the IEEE and AAAS. He is the Chairman of the Board of Directors of EASCON.

A 120-Mbit/s 14-GHz regenerative receiver for spacecraft applications

W. H. CHILDS, P. A. CARLTON, R. EGRI, C. E. MAHLE, AND A. E. WILLIAMS

(Manuscript received December 3, 1980)

Abstract

An integrated 120-Mbit/s 14-GHz QPSK receiver, which is differentially coherent, and its associated 14-GHz channel filter and FET amplifier are described. The weight, size, power requirements, and reliability of these elements are consistent with those required for spacecraft applications. The FET amplifier provides 65 dB of gain and establishes the required RF power level and signal-to-noise ratio. The channel filter provides in-band amplitude shaping and adjacent channel rejection. Differentially coherent detection is performed directly at 14 GHz. The DQPSK receiver uses all integrated construction and has 12 MICs and 6 hybrid ICs in one enclosure. The required phase-stable time-delay element is realized by using MIC bandpass filters on silica substrates. The necessary temperature compensation is provided by a transmission line in the undelayed path.

The measured bit-error rates (BERs) agree well with computer models of differentially coherent QPSK detection. The results of this project demonstrate the feasibility of onboard data regeneration in a digital satellite communications system.

Introduction

Onboard data regeneration in a digital satellite communications system is an attractive and rapidly developing option for future ss-

TDMA systems. Application of a hard decision regenerative receiver on the satellite isolates up- and down-link impairments [1] and allows the individual optimization of these two segments. These impairments include up-link noise, co-channel and adjacent channel interference (up-link), and satellite band-limiting effects with resulting TWTA distortion. As is well known [1], [2], onboard data regeneration causes the addition of up- and down-link BERs, whereas a conventional transponder causes up-link noise, interference, and distortion to be passed to the down-link signal. For a given BER, onboard data regeneration allows a significant reduction of the required up- and down-link energy per bit to noise density ratios (E_b/N_o) relative to those required when a conventional transponder is employed in the satellite.

Finally, an SS-TDMA system with onboard regeneration will perform the required switching at baseband [3] instead of at microwave frequencies. The baseband processor will function similarly to a high-speed computer and could build down-link data streams with great flexibility. It is believed that the ability to switch and route the original data implies a system architecture which is significantly more flexible than that provided by present SS-TDMA systems.

Spacecraft hardware must be reliable and lightweight, with minimum power consumption. Coherent QPSK (CQPSK) receivers have complex implementations, and their space application has always appeared formidable. For this reason, interest has focused on DQPSK receivers [4]-[9], in which the RF waveform is delayed one symbol time and correlated with the present waveform. This approach eliminates the need for carrier recovery and, if accomplished at RF, the requirement for local oscillators and mixers. It is also compatible with SS-TDMA, since only clock acquisition is required. The simplicity of DQPSK detection in comparison to CQPSK detection is balanced by a performance penalty of approximately 2.5 dB. Nevertheless, analysis [1], [2] of a satellite system that employs a DQPSK up-link and a CQPSK down-link shows a significant performance advantage over a CQPSK link using a conventional transponder.

Early efforts [4], [5], [7] were directed toward achieving a temperature-stable RF time delay. Since there are many 360° phase shifts stored in the RF time-delay element, the phase shift at the input of the QPSK demodulator can exhibit undesirable temperature sensitivity, which in turn degrades the BER. (It is estimated that a 7° phase error requires a 1-dB increase in E_b/N_o to maintain a constant BER.) Two delay technologies were developed: MIC filters on fused silica [4], [5], [10] and transmission lines on high dielectric substrates [7], [11]. Two

methods of temperature compensation have been reported: passive compensation with different substrate materials (Reference 7 with refinements in Reference 12) and active compensation with a temperature-controlled electronic phase shifter [4]. A new temperature-compensated time-delay technique is reported in which time delay is provided by MIC filters on silica substrates and phase shift is compensated by the substrate material in the undelayed path. This approach is believed to combine the best features of the earlier approaches: that is, the MIC filters on silica provide less loss in a small area and the passive substrate compensation is considered to be sufficiently reliable for spacecraft applications.

Unlike conventional QPSK receivers in which signal filtering is performed at an intermediate frequency, usually UHF, these concepts necessitate filtering at 14 GHz. The channel bandwidth should be as narrow as possible to maximize the transmission rate over the entire band. Computer simulations and experiments at COMSAT Labs have shown that bandwidth-symbol time (BT) products of 1.1 are practical, if the channel filters are group delay equalized. (Reference 13 notes the case of nonequalized filters.) The filter described provides flat group delay, in-band amplitude shaping, and adjacent channel rejection. The RF DQPSK detection described requires RF power levels of approximately +10 dBm. Depending on the particular link, this implies RF gains of 50 to 70 dB at the front end of the transponder. The amplifier demonstrates the capability of packaging large amounts of gain in relatively small volumes.

It should be noted that this hardware is not flight qualified; however, the reported realizations are feasibility models which would benefit from additional development work. The major issues originally formulated and resolved are as follows: realization of a temperature-stable RF delay element, implementation of DQPSK detection in a large MIC assembly, realization of the filtering function directly at 14 GHz, and the realization of high gain amplification at 14 GHz. During initial hardware development, it would have been impractical to achieve immediate flight-worthy status; instead parameters that are significant for actual spacecraft applications were determined in terms of weight reduction, minimum power consumption, packaging, and reliability.

Regenerative transponder configuration

Figure 1 shows a possible configuration of a 6-channel regenerative transponder. The amount and distribution of 14-GHz gain depends
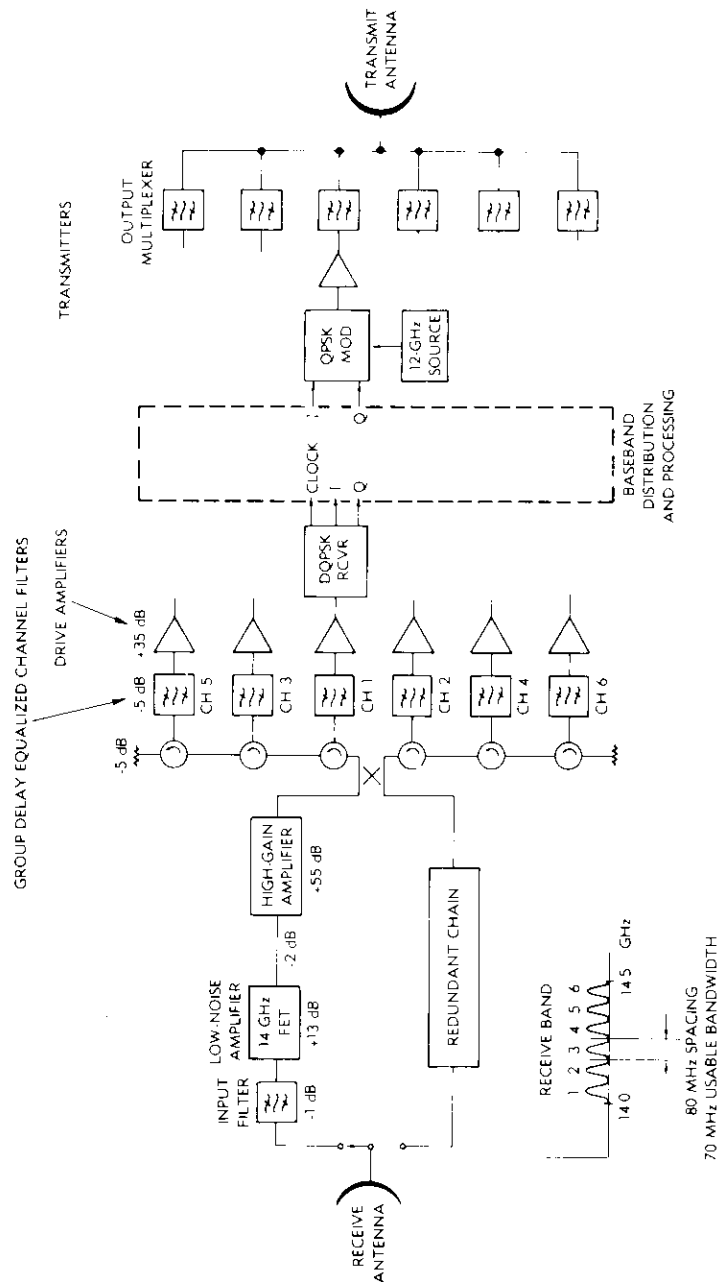
Figure 1. *Block Diagram of a Regenerative Transponder*

upon the details of the link, the power requirements of the DQPSK demodulator, and the anticipated link fades which determine the dynamic range. The major elements of this regenerative transponder are the DQPSK receiver, the channel filter, the FET amplifier, and the baseband processor. This paper is concerned with the microwave elements (*i.e.*, the DQPSK receiver, channel filter, and FET amplifier). The baseband processor is described in Reference 3. An advanced system would employ many spot beams, resulting in a large number of channel filters and DQPSK demodulators.

14-GHz DQPSK filter

Narrowband channel filters for regenerative receivers must combine sharp out-of-band frequency selectivity with a rounded in-band response to minimize adjacent channel and intersymbol interference, respectively. These specifications generate conflicting design requirements, and conventional elementary prototype filters cannot simultaneously achieve both specifications. To overcome these limitations, a compound filter type was developed by using Bessel and elliptic type bandpass filters in cascade. The rounded in-band amplitude response and flat group delay are developed by the Bessel filter, and the sharp out-of-band frequency selectivity by the elliptic filter.

A computer simulation program termed X-Champ [14] was used to "measure" channel degradation as the compound filter parameters were adjusted within the constraints of the amplitude and group delay specifications. It was found that a 4-pole 72-MHz bandpass Bessel filter in cascade with a 6-pole 78-MHz bandpass elliptic filter caused less than 0.4-dB degradation in the 4-phase 120-Mbit/s transmission at a BER of 10 [4]. Both filters were made by using fundamental circular waveguide dual-mode TE_{111} technology [15], [16]; a ferrite waveguide circulator was used between the filters to ensure a return loss better than 20.0 dB. The measured transmission response is shown in Figure 2 and the measured group delay in Figure 3. The filter has physical dimensions of 20 × 4 × 5 cm.

The current filter development was concluded at the breadboard level. Well-known techniques for reducing weight and loss in these filters could be applied in the future. Additional work could explore the realization of the desired function in a single filter.

The communications characteristics of the up-link are determined by the baseband filters, the nonlinearities of the transmit tube, the
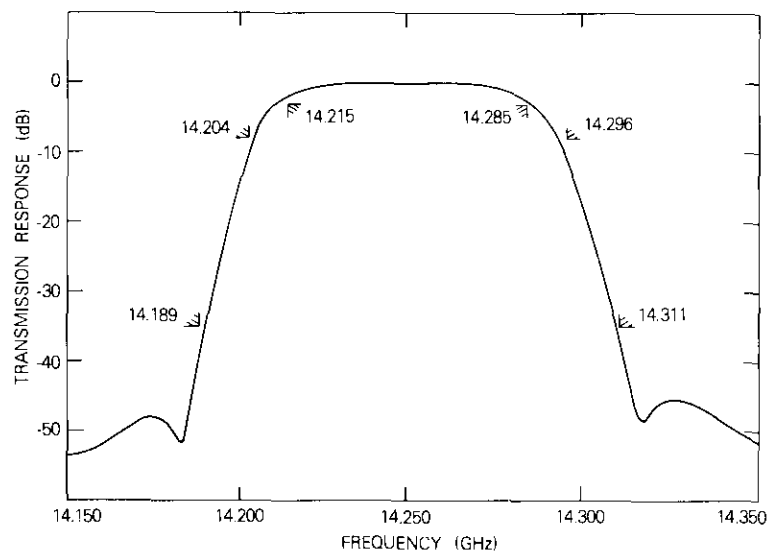
Figure 2. *Measured Transmission Response of the Channel Filter*
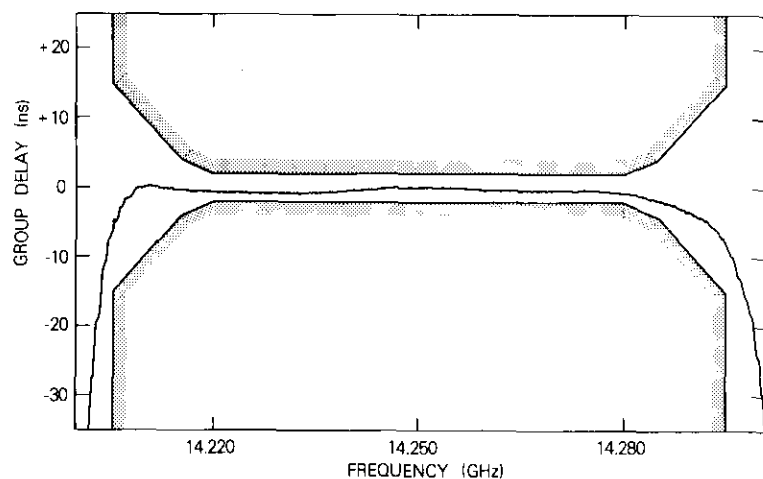
Figure 3. *Measured Group Delay for the Channel Filter*

high-power transmit filter (if any), and the receive filter. This effort was not concerned with a complete optimization of the link, which was believed to be premature relative to the required hardware developments and the existing understanding of DQPSK detection. Initially, it was known that nongroup delay equalized filters would

cause excessive degradations for the channel bandwidths of interest (see Reference 13). Therefore, the primary consideration of the initial filter modeling was to determine a practical filter realization for narrow channel bandwidths (bandwidth-baud time product of 1.1) when DQPSK detection was used rather than CQPSK detection.

The initial work was carried out with only the receive filter as the band-limiting element. Later, a 4-pole Butterworth filter with a band-width-baud time product of 1.5 was added as the transmit filter. The results obtained in theory and in practice are not necessarily optimum but are within a few tenths of a dB. More importantly, the ability to achieve DQPSK detection in a channel bandwidth consistent with commercial requirements was found to be realizable; link optimization can be pursued later.

FET amplifier

Figure 4 is a photograph of the high-gain 14-GHz FET amplifier (11.4-cm length and 6.4-cm width). A 2-stage unit amplifier with low input/output VSWRS and flat gain was developed. The techniques used in this amplifier design are described in References 17 and 18. The characteristics of this amplifier were developed sufficiently so that four of these units could be cascaded as shown. The in-band amplitude response shown in Figure 5 indicates that, over the 14.0- to 14.5-GHz band, the gain is approximately 65 ± 0.5 dB. The out-of-band response shown in Figure 6 evidences that the amplifier exhibits an extremely well-behaved bandpass characteristic. The amplifier requires 3 W of power (0.2 A at 15 V).

DQPSK receiver

A block diagram of the DQPSK receiver is shown in Figure 7. The 14-GHz 120-Mbit/s waveform is divided into delayed and undelayed paths by the second directional coupler. The delayed and the undelayed waveforms are processed and mixed in the QPSK demodulator, thereby recovering the original data. The temperature in the undelayed path compensates for the temperature-induced phase changes in the delayed path. The phase shifter is required to set the relative phase of the delayed and undelayed waveforms at the input of the QPSK demodulator.

The narrow channel filter ($BT \sim 1.1$) causes a significant envelope variation in the QPSK waveform, which is detected by the directional coupler/detector combination (Figure 7). Since the power spectrum of
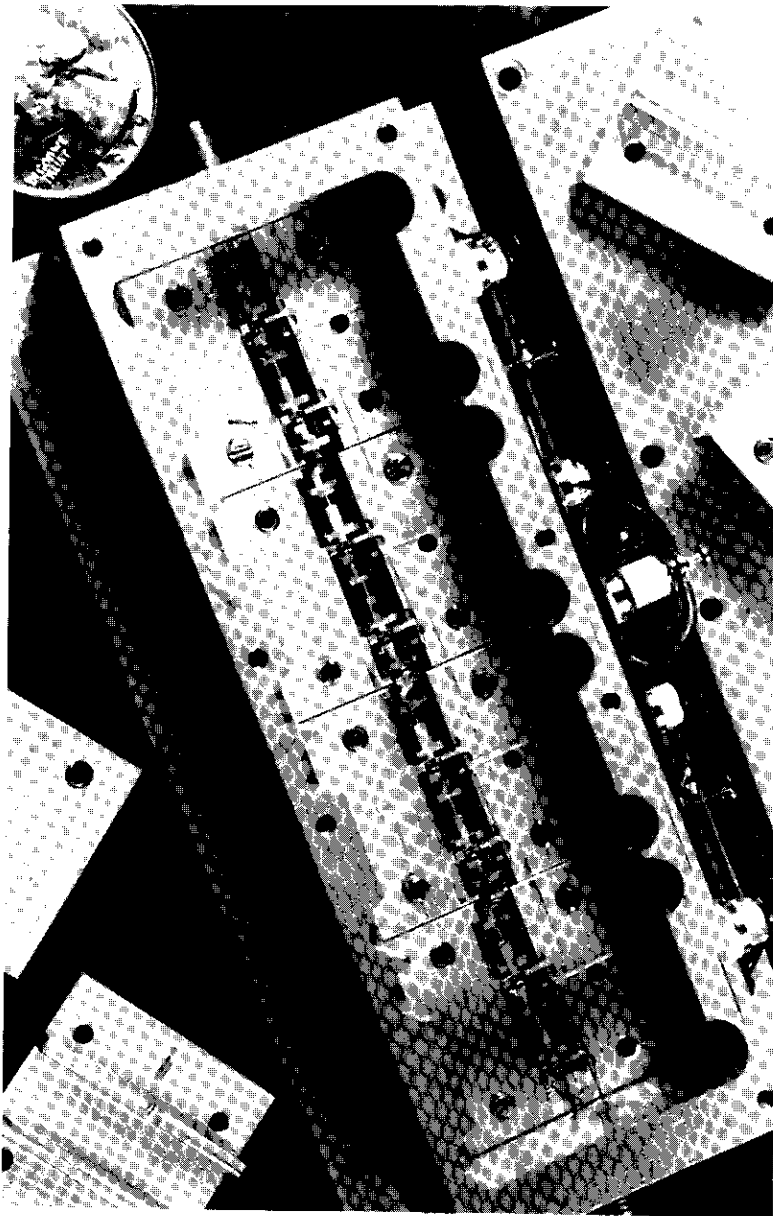
Figure 4. *High-Gain 14-GHz FET Amplifier*
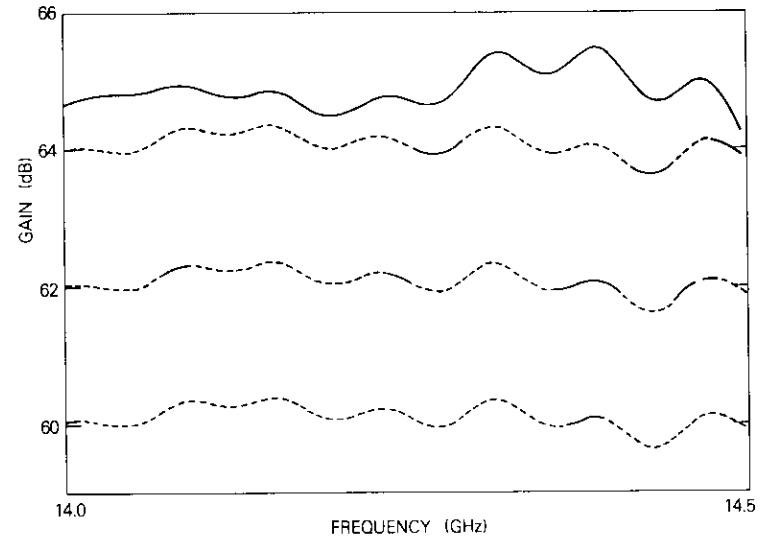
Figure 5. *Measured In-Band Response of the 14-GHz FET Amplifier*
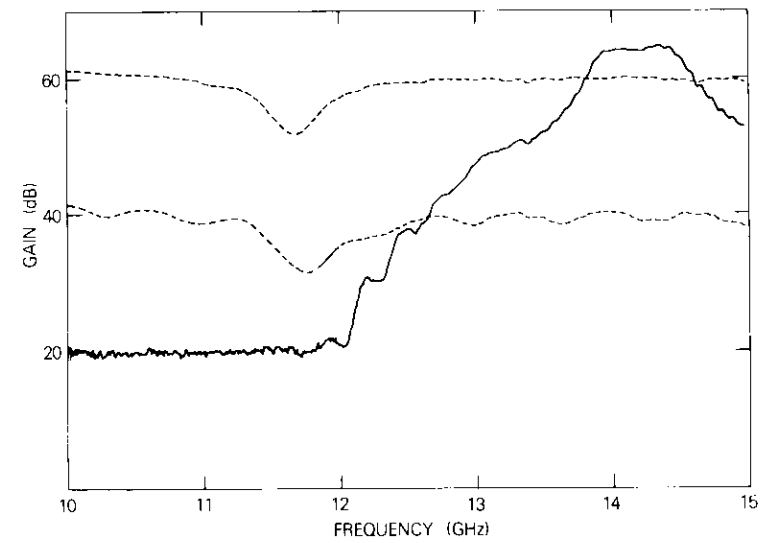
Figure 6. *Measured Out-of-Band Response of the 14-GHz FET Amplifier*
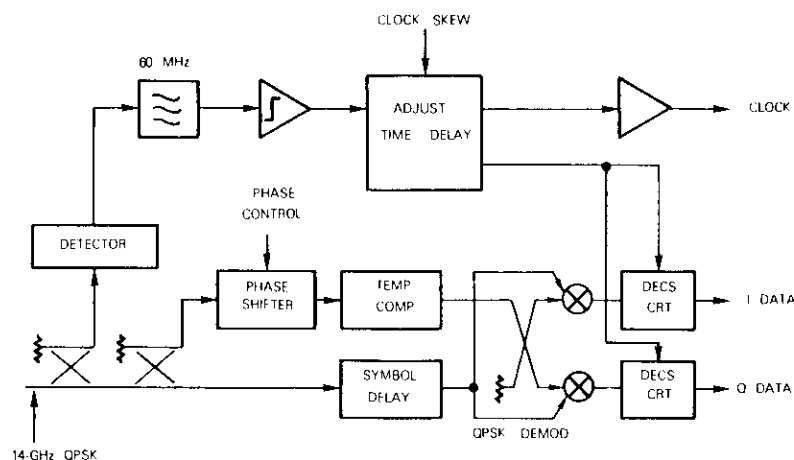
Figure 7. *Block Diagram of the DQPSK Receiver*

this signal contains lines every 60 MHz [19], a 60-MHz bandpass filter selects the waveform; the signal is then limited and phased for a mid-bit timing decision. The hard-limited-data waveforms and the recovered clock signal are combined in the decision circuits where hard decisions on the value of the data are performed. The two in-phase and quadrature data waveforms and the clock are the output of the DQPSK receiver.

QPSK modulation causes the RF waveform to assume one of four orthogonal phase values during the signaling interval. In differentially coherent detection, the four information levels are recovered by comparing the RF phase of the present interval to the RF phase of the past interval. For the received data to be equivalent to the original data, the original data must be differentially encoded using the algorithm

$$R_k = d_k + R_{k-1}$$

where subscript k refers to the signaling interval. The position of the RF vector is described by R_k, and d_k is the value of the original data where

$$R_k, d_k = 0, 1, 2, 3 \quad .$$

The symbol, $+$, indicates modulo 4 addition. Differential encoding is also commonly employed in coherent QPSK detection for ambiguity resolution. It can be implemented quite simply in the modulator with not more than two integrated circuits [20].

Time-delay element

A new method of time delay was developed for the integrated receiver. The application of MIC bandpass filters on fused silica substrates, which are used as the time-delay element, is attractive, since RF time delay is obtained in a small area with relatively low losses. In addition, the silica material is quite stable, and compensating for temperature is relatively easy. Temperature compensation is achieved in the reference path with a simple microstrip line on alumina. The temperature coefficient of the phase response characteristic is much greater in alumina than in silica (approximately by a factor of 9). Therefore, the time delay of the microstrip line on alumina can be several times less than the time delay through the bandpass filters of the delayed path, and still compensate for the temperature-induced phase shifts of the delayed path. As a result, the net phase shift at the QPSK demodulator is nearly temperature independent.

The design process leads to the selection of delay times through the delayed and reference paths. The delay times that cause the net phase shift to be independent of temperature are prescribed as follows:

$$T_D = \frac{T_R}{[1 - (\alpha_D V_{PU}/\alpha_U V_{GU})]}$$

$$T_U = \frac{T_R (\alpha_D V_{PU}/\alpha_U V_{GU})}{[1 - (\alpha_D V_{PU}/\alpha_U V_{GU})]}$$

$$T_R = T_D - T_U$$

where T_D = time delay in the delayed path

T_U = time delay in the undelayed (reference) path

T_R = required net time delay (16.7 ns for a 120-Mbit/s system).

α_D = temperature coefficient of phase change in the delayed path (which must be measured)

α_U = temperature coefficient of phase change in the reference path (which must be measured)

V_{PU} = phase velocity in the reference path

V_{GU} = group velocity in the reference path.

The above equations are obtained similarly to the derivations shown in References 7 and 12.

For the 14-GHz 120-Mbit/s case, the delayed path should have a
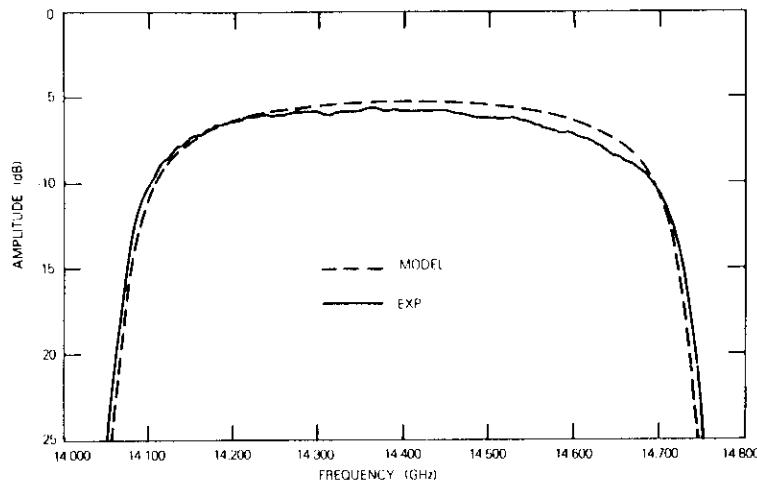
Figure 8. *Measured Transmission Response of a Time-Delay Filter*

19.0-ns delay and the reference path a 2.3-ns delay. Partitioning this delay among four filters indicated a required delay of 4.7 ns per filter. The time delay of a prototype filter can be estimated in terms of its element values and fractional bandwidth [21]. However, losses, dispersion, different odd/even phase velocities, and end-effect capacitances cause the actual time delay to differ from the simple theoretical estimate. An accurate computer model of these effects is required to realize a satisfactory design within a reasonable period of time.

Earlier computer models for edge-coupled microstrip lines have been extended to include the effects of dispersion [10], [19], [22]. The filter design is started using the simple time-delay estimate. Computer simulations then indicate an initial time-delay correction of 5 to 10 percent. The bandwidth (or the number of poles) is adjusted accordingly and the filter redesigned. The proper time delay, as predicted by computer simulation, is normally obtained in two or three trials. The resulting correlation between measured and simulated response is very good. Representative results for a 13-pole MIC filter on 0.4-mm-thick silica are shown in Figures 8 (transmission response) and 9 (time delay). The length of the microstrip line on alumina (the undelayed path) is properly estimated using group velocity [7], [23].

The time-delay unit is shown in Figure 10. The delayed path is realized with a cascade of four 12-pole MIC filters on 0.4-mm-thick silica. The transmission response of the delayed path is shown in Figure 11 and the time delay in Figure 12. It can be seen that the 19-
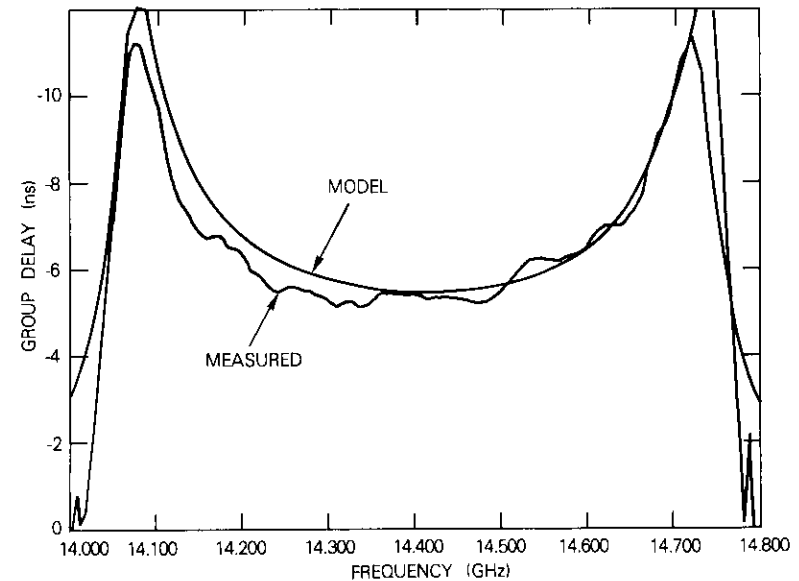
Figure 9. *Measured Time Delay of a Time-Delay Filter*

ns delayed path time delay is compensated by the 2.3-ns delay of the reference path so that the net delay is approximately 16.7 ns. Also, the time delay has a nominal ± 5-percent variation over approximately a 400-MHz bandwidth. Although two separate time-delay assembly designs would be more than sufficient to cover the whole 500-MHz bandwidth, a single design may also achieve this coverage.

Extensive computer simulations and laboratory experiments have shown that losses through the filters are determined by the required delay time, the dielectric constant of the substrate material, and the substrate thickness. Within certain bounds, losses are reduced by selecting materials with low dielectric constants and thick dimensions. Given the substrate choice, the loss is fixed by the delay time. Thus, a certain number of poles and bandwidth will give approximately the same loss as a different number of poles and bandwidth adjusted to the same time delay. Generally, the best procedure is to increase the number of poles so that the working bandwidth of the complete assembly will exceed 250 MHz.

Figure 11 indicates that the loss of the reported time-delay assembly is 19 dB at the center of the band (14.250 GHz). This loss is consistent with the available input powers (0 to +10 dBm) and the low power requirements of the QPSK demodulator (−20 to −25 dBm). For longer
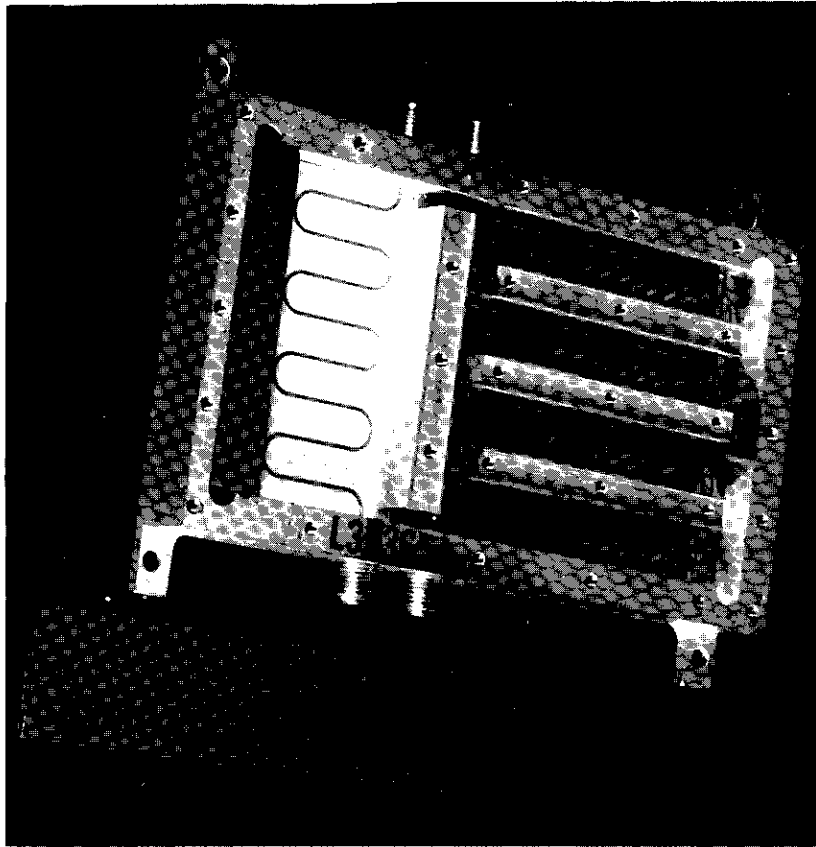
Figure 10. *Time-Delay Assembly*

time delays or for lower input powers, this loss can be reduced by using thicker substrates.

The required phase stability was achieved by mounting the silica substrates in an Invar box (or carrier at the receiver level). The unit shown in Figure 8 was subjected to repeated temperature cycles from 0°C to +40°C with no more than 1.0 electrical degree net phase variation.

QPSK demodulator

The QPSK demodulator is a key component for achieving theoretical performance in a DQPSK receiver. The assembly performs orthogonal
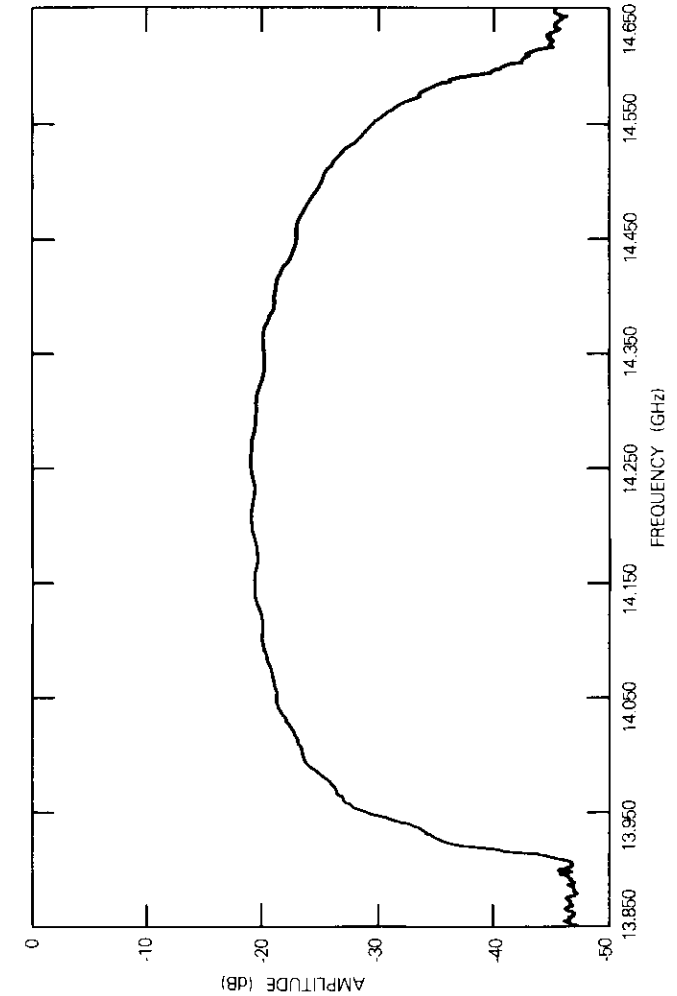
Figure 11. *Measured Transmission Response of a Time-Delay Assembly*
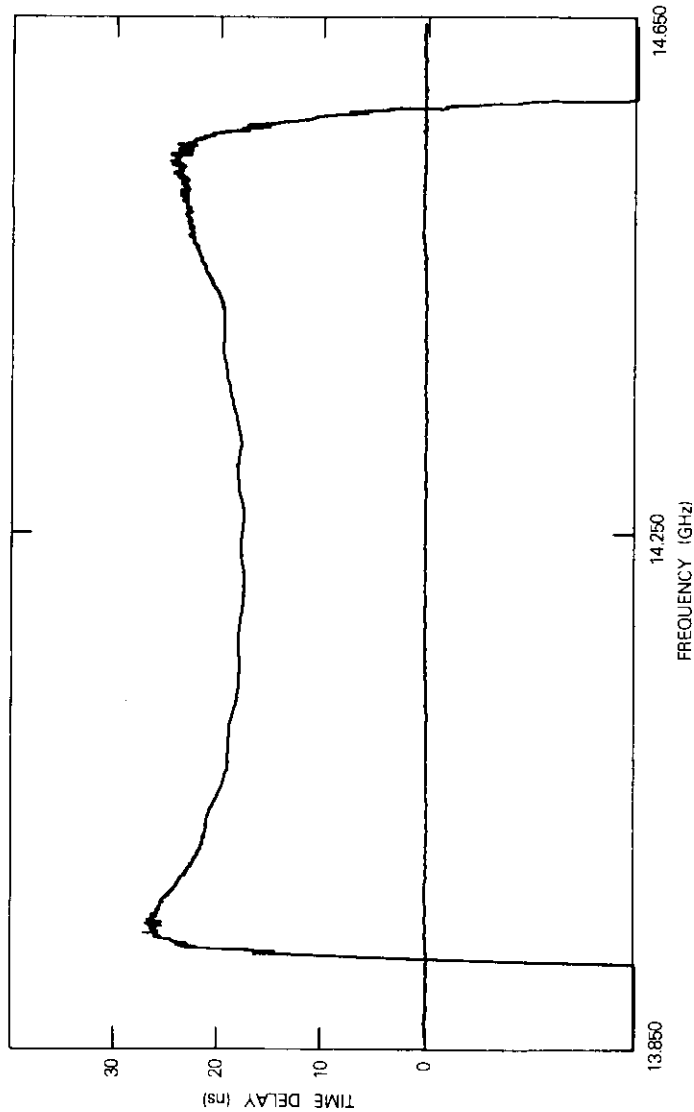
Figure 12. *Measured Time Delay of a Time-Delay Assembly*

phase detection, hard limiting of the two resulting analog waveforms, and a hard decision (using the recovered clock) of the waveforms. The output is the original data in two 60-Mbit/s waveforms. Differential detection at microwave frequencies creates novel phase detection problems, since the RF power levels at the input lines of the QPSK demodulator have a fixed ratio and are linearly related to the receiver input power level. Since a limiting amplifier will further impair the detection process (due to bandwidth restrictions prior to amplitude limiting), the design goal was to achieve a receiver without limiting amplifiers. To provide a sufficient dynamic range, the phase detectors must function with varying power levels at both inputs. This is in contrast to normal phase detector applications in which the power level is fixed at one input and allowed to vary at the other arm. The phase detectors were designed to function at low power levels (−25 to −10 dBm) and to provide a minimum 15-dB dynamic range.

For reasons of weight, size, and reliability, realization of the DQPSK receiver as a super-MIC assembly was considered mandatory. Conventional MIC QPSK demodulators have alternating RF inputs and IF outputs that complicate the planar realization of a DQPSK receiver. A novel QPSK demodulator that provides adjacent RF inputs and adjacent IF outputs was invented for this application [24]. The two RF inputs are shown on the left side of Figure 13. The RF processing circuits then provide the proper power splitting and phasing to achieve the desired orthogonal phase detection. This topology is realized by using two cascaded 3-dB interdigitated couplers [25] to effect crossover of the two RF signals. Figure 13 shows that the RF processing network is symmetrical which facilitates orthogonal detection.

The hybrid integrated circuit on the middle substrate provides signal processing and a limited output; the remaining hybrid integrated circuit (on the right of Figure 13) accepts two clock inputs and performs a hard decision on the limited data. The QPSK demodulator as a unit is topologically consistent with the requirements of a planar DQPSK receiver.

Detected output versus input RF phase is shown in Figure 14. The horizontal coordinate is the RF phase difference at the input of the QPSK demodulator. The two vertical outputs are the ECL outputs of the I and Q channels. These data were acquired for an RF power level of −15 dBm into each input of the demodulator and for a carrier frequency of 14.250 GHz. These same characteristics can be achieved for input RF power levels of −25 to −10 dBm.
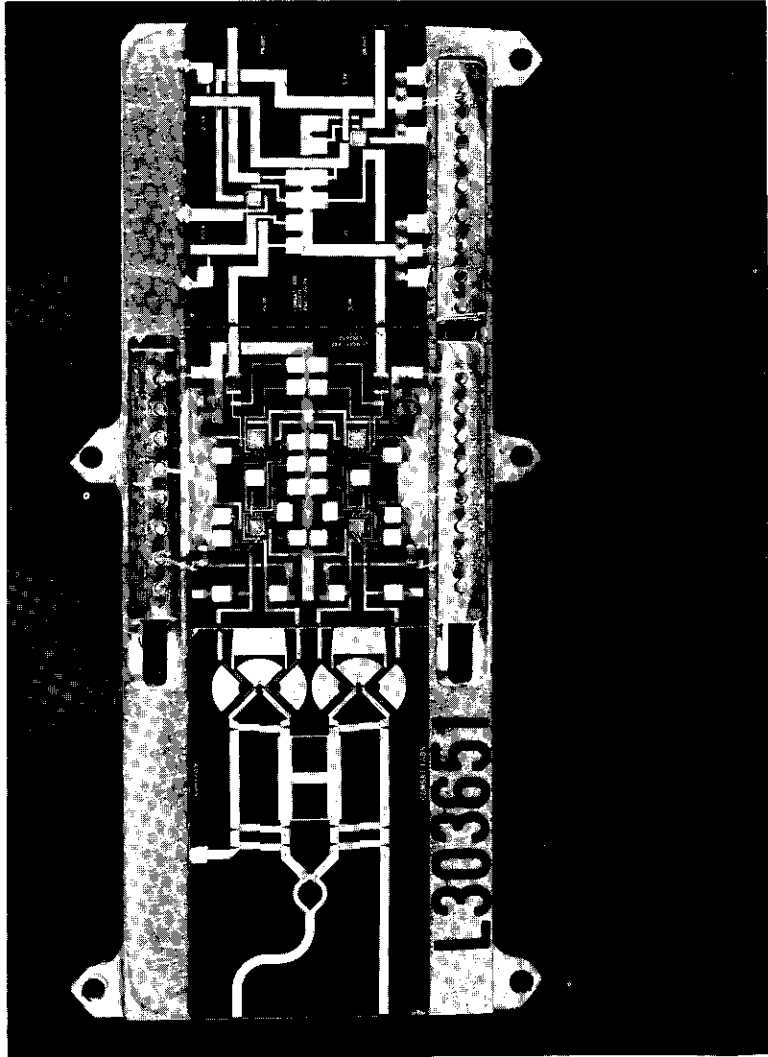
Figure 13. *QPSK Demodulator Subassembly*
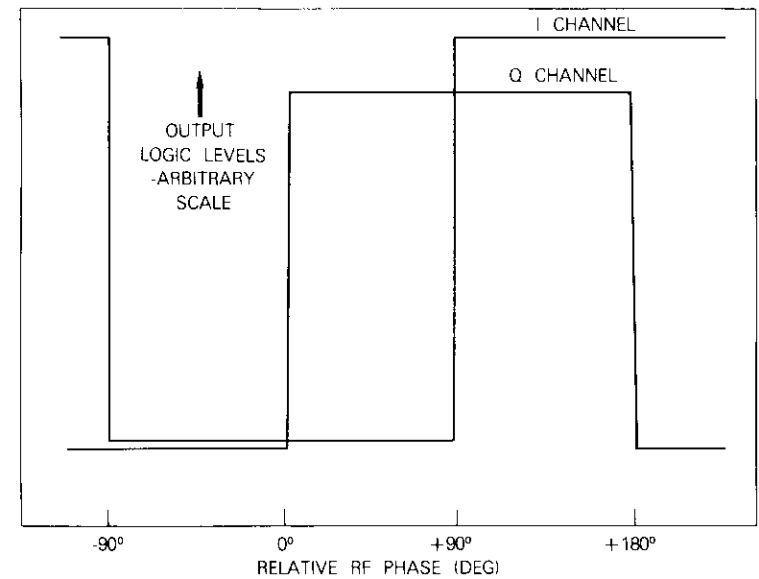
Figure 14. *Measured Phase Response of the QPSK Demodulator Showing Output Logic Levels*

Electronic phase shifter

The receiver utilizes an electronic phase shifter which provides the proper phase difference value at the input of the QPSK demodulator. This approach was found to be extremely convenient for laboratory development. However, the flight hardware will probably require a fixed-tuned unit which is under development.

The electronic phase shifter is a simple reflection type using varactor diodes. Impedance matching causes a linear relationship between the phase shift and the bias voltage (Reference 4 should be consulted for details). Figure 15 shows the input carrier of the DQPSK receiver. The electronic phase shifter is the upper right substrate.

Clock recovery

Clock recovery is achieved by filtering the detected envelope of the 14-GHz QPSK waveform. Envelope detection is accomplished with the MIC shown on the left of Figure 15. A directional-coupler balanced-detector combination detects the envelope which, after buffering, is
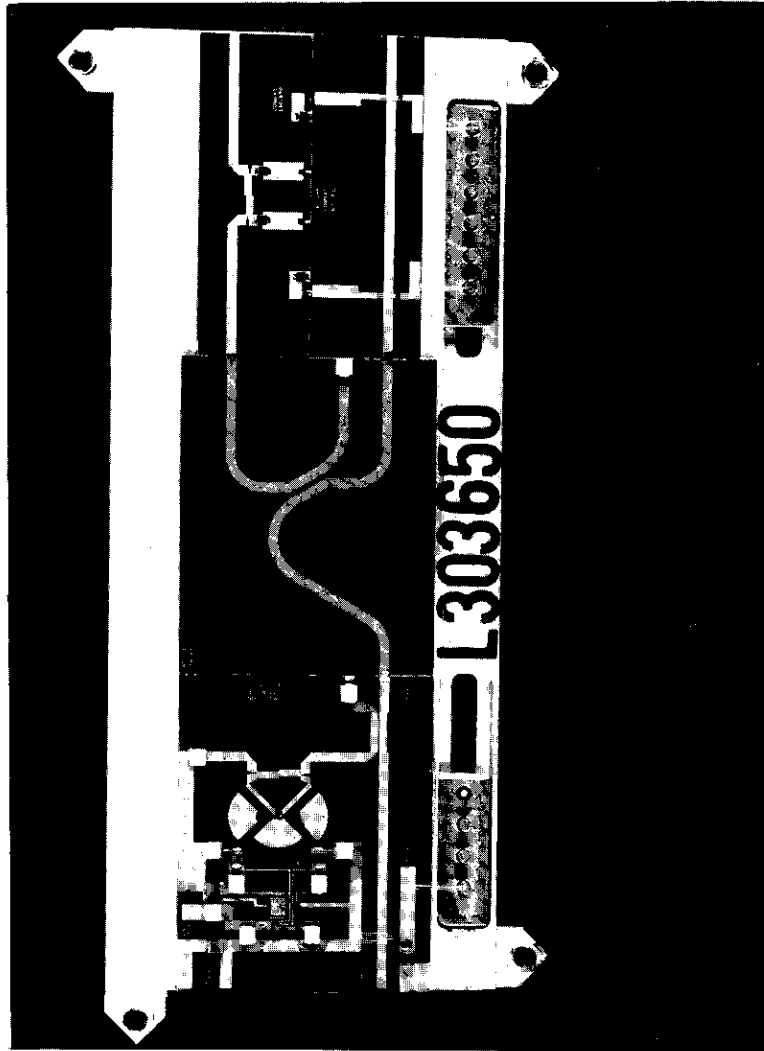
Figure 15. *Front End Subassembly*

provided as an output. After filtering with a 2-percent, 5-pole, 60-MHz filter, the signal is limited in the clock recovery module shown in Figure 16 by the first hybrid IC on the left.

The time delay of the limited waveform can then be adjusted with the middle two substrates of the module (Figure 16). This electronic delay line is realized by placing seven ECL gates in cascade. A multiplexer, which is set by a 3-bit code, then routes the signal through the gates providing approximately 8 ns of delay in 1-ns steps. This circuit was subjected to extreme temperature variations with negligible variations in the delay times.

The final circuit in the clock recovery module (on the right of Figure 16) buffers the clock for external output and for transfer to the decision circuit.

DQPSK receiver construction

Figure 17 shows the integrated DQPSK receiver with dimensions of $23 \times 15 \times 2.3$ cm. The four major subassemblies shown in Figures 10, 13, 15, and 16 are located in a single box with one input connector (14 GHz) and three output connectors (two data outputs and clock).

A high level of integration is achieved in the following manner. After fabrication, the MICs and hybrid ICs are permanently attached to their carriers. The four major subassemblies are temporarily installed in test fixtures. The time-delay element is tested for time delay, transmission response, and return loss. The QPSK demodulator assembly is tested for proper functioning of the hybrid ICs and for orthogonality in the QPSK phase detection. The input carrier is tested for phase control, power split, and envelope detection. The limiting feature and the clock skew 6-bit control of clock recovery module are also tested.

After unit testing is successful, a preliminary DQPSK receiver is assembled by interconnecting the subassemblies in their test fixtures. Initially, the clock is "hard-wired," and the first BER data are obtained. If this step is satisfactory, then the recovered clock is substituted for the hard-wired clock and the clock skew is properly set. The measured BER with recovered clock is expected to be equivalent to the BER testing with the hard-wired clock.

Following successful preliminary integration, the subassemblies are removed from their test fixtures and installed in the integrated enclosure. The substrates are interconnected with gold ribbon. Conventional wiring is performed in the understory of the box.
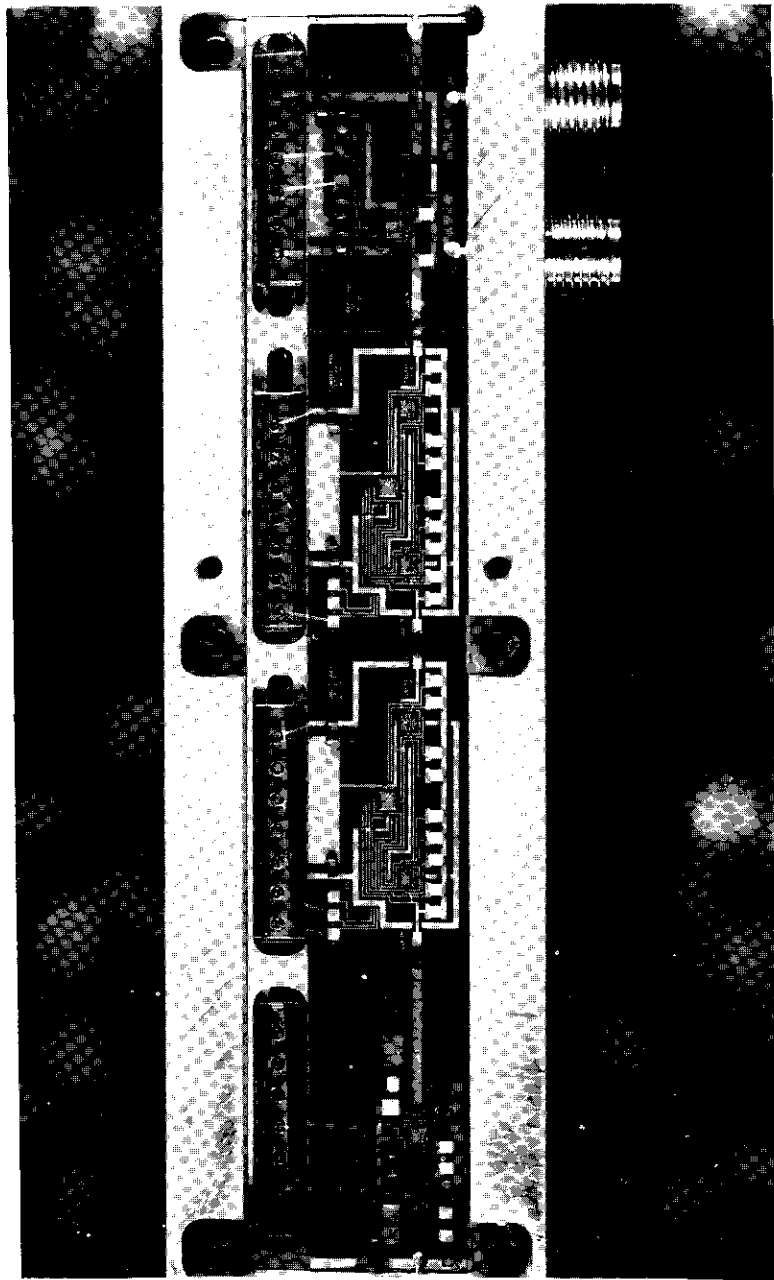
Figure 16. *Clock Recovery Module Subassembly*
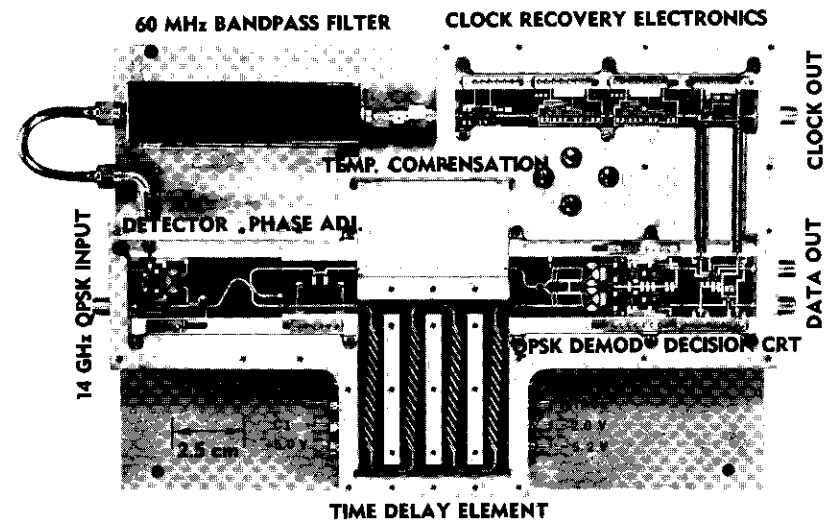
Figure 17. *DQPSK Receiver*

Measured bit-error rates

The measured BER data for the integrated DQPSK receiver shown in Figure 18 were obtained for a 120-Mbit/s rate at 14.255 GHz and for an RF power level of approximately +10 dBm. Figure 18 shows BER versus E_b/N_o for ideal CQPSK, ideal DQPSK, as well as for a computer simulation [2] and the measured case. The computer simulation uses the measured characteristics of the baseband and the channel filters.

Conclusions

The integrated DQPSK receiver and channel filter demonstrates the ability to achieve good performance in a hardware form suitable for possible large-scale applications on board commercial communications satellites. The measured and simulated BERs are in good agreement, demonstrating that band-limiting effects for DQPSK detection can be modeled with confidence. The realization of the DQPSK receiver as a super-MIC assembly is achieved without bench alignment or tuning; this "as printed" performance is due to superior unit performance and integration techniques. The realization of the FET amplifier demon-
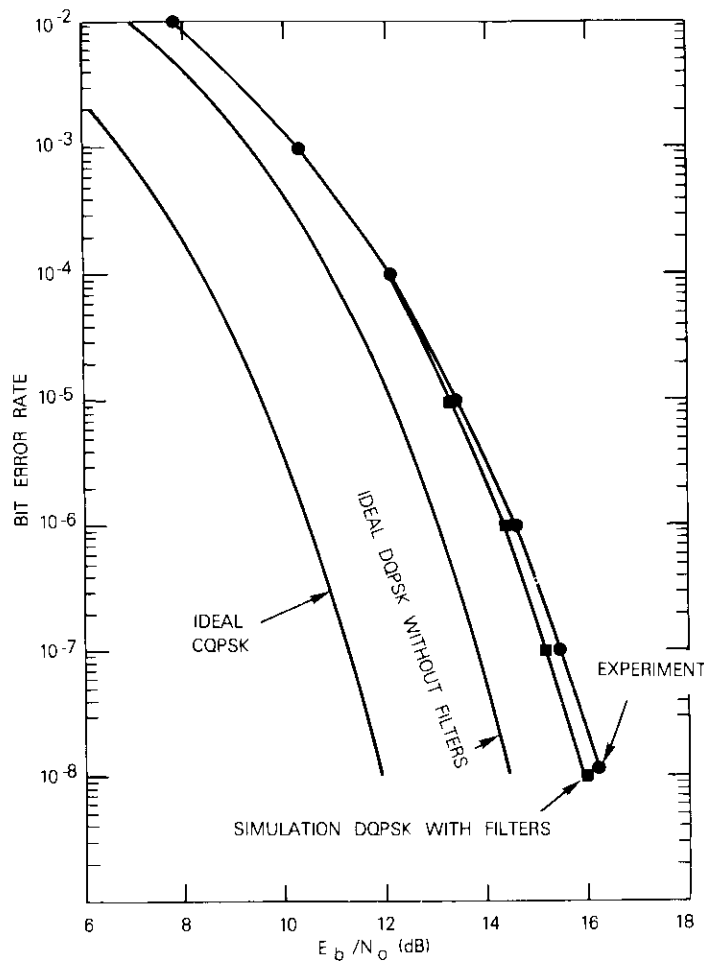
Figure 18. *Measured Bit-Error Rate of the DQPSK Receiver*

strates that the required 14-GHz gains (of the order of 60 dB) can be achieved in small volumes. This hardware will be developed to the prototype level which will include additional efforts in the following areas: weight reduction and mechanical design, minimization of required power, and reliability studies.

References

[1] S. J. Campanella, F. Assal, and A. Berman, "On-Board Regenerative Repeater," *ICC'77 Conference Record*, Vol. 1, pp. 6.2-121–6.2-125.

[2] Y. S. Lee, "Simulation Analysis for Differentially Coherent Quaternary PSK Regenerative Repeater," *COMSAT Technical Review*, Vol. 7, No. 2, Fall 1977, pp. 447–474.

[3] J. H. Apple, "An On-Board Baseband Switch Matrix for SS-TDMA," Fifth International Conference on Digital Satellite Communications, Genoa, Italy, March 1981.

[4] W. H. Childs, C. E. Mahle, and J. Potukuchi, "An Integrated DQPSK Demodulator for 14-GHz Satellite Communications," *1978 IEEE International Microwave Symposium Digest*, pp. 64–66.

[5] Y. S. Lee, "14 GHz MIC 16-ns Delay Filter for Differentially Coherent QPSK Regenerative Repeater," *1978 IEEE International Microwave Symposium Digest*, pp. 37–40.

[6] C. E. Mahle, W. H. Childs, and A. L. Berman, "A DQPSK Satellite Transponder Using 14-GHz MIC Technology," *IEEE EASCON Record*, 1978, pp. 411–416.

[7] Y. S. Lee and W. H. Childs, "Temperature-Compensated BaTi₄O₉ Microstrip Delay Line," *1979 IEEE International Microwave Symposium Digest*, pp. 419–421.

[8] M. Lopriore, "Communications Satellite Payloads: A Review of Past, Present, and Future ESA Developments," *1980 IEEE International Microwave Symposium Digest*, pp. 189–191.

[9] M. Massani, "Microwave Technology Developments in Italian Space Programs," *1980 IEEE International Microwave Symposium Digest*, pp. 193–194.

[10] W. H. Childs, "Design Techniques for Bandpass Filters Using Edge-Coupled Microstrip Lines on Fused Silica," *1976 IEEE International Microwave Symposium Digest*, pp. 194–196.

[11] Y. S. Lee, W. J. Getsinger, and L. R. Sparrow, "Barium Tetratitanate MIC Technology," *IEEE Transactions on Microwave Theory and Techniques,* MTT-27, July 1979, pp. 655–660.

[12] P. De Santis, "On the Design of Temperature Stabilized Delay Lines," *IEEE Transactions on Microwave Theory and Techniques,* MTT-28, September 1980, pp. 1028–1029.

[13] C. L. Cuccia, "Digital Satellite Communications—Systems, Components, and Limitations," *1978 IEEE International Microwave Symposium Digest,* pp. 463–465.

[14] L. C. Palmer and S. Lebowitz, "Including Synchronization in Time-Domain Channel Simulation," *COMSAT Technical Review,* Vol. 7, 1977, pp. 475–525.

[15] A. E. Atia and A. E. Williams, "Narrow-Bandpass Waveguide Filters," *IEEE Transactions on Microwave Theory and Techniques,* MTT-20, 1972, pp. 258–265.

[16] A. E. Atia, A. E. Williams, and R. W. Newcomb, "Narrow-Band Multiple-Coupled Cavity Synthesis," *IEEE Transactions on Circuits and Systems,* CAS-21, 1974.

[17] H. L. Hung, R. E. Stegens, and M. Dressler, "Low-Temperature Performance of GaAs MESFET Amplifiers at 14.256 GHz," *Proceedings of the Sixth Biennial Cornell Electrical Engineering Conference,* August, 1977, pp. 331–336.

[18] P. Estabrook, C. M. Krowne, E. J. Crescenzi, Jr., and R. E. Stegens, "A Low Noise Single-Ended GaAs Schottky FET Amplifier for a 14 GHz Satellite Communication Application," *1978 IEEE MTT-S International Symposium Digest,* pp. 129–131.

[19] J. J. Spilker, *Digital Communications by Satellite,* Englewood Cliffs, New Jersey: Prentice Hall Inc., 1977.

[20] C. Wolejsza, Private Communication.

[21] G. L. Matthaei, L. Young, and E. M. T. Jones, *Microwave Filters, Impedance-Matching Networks, and Coupling Structures,* New York: McGraw Hill, 1964.

[22] W. J. Getsinger, "Dispersion of Parallel-Coupled Microstrip," *IEEE Transactions on Microwave Theory and Techniques,* MTT-21, March 1973, pp. 144–145.

[23] W. J. Getsinger, "Microstrip Dispersion Model," *IEEE Transactions on Microwave Theory and Techniques,* MTT-21, January 1973, pp. 34–38.

[24] W. H. Childs and C. E. Mahle, Patent Application, "Planar QPSK Demodulator."

[25] W. H. Childs and P. A. Carlton, "A 3-dB Interdigitated Coupler on Fused Silica," *1977 IEEE International Microwave Symposium Digest,* pp. 370–372.

William H. Childs received a B.S. in electrical engineering from M.I.T. and an M.S. and a Ph.D. (both in electrical engineering) from Iowa State University. Prior to joining COMSAT Laboratories in 1974, he worked on microwave integrated circuit design at the Naval Weapons Center, China Lake, California. At COMSAT Laboratories, his research interests centered on microwave integrated circuit design and CAD modeling of microwave circuits; his responsibilities included project management of the SBS Regenerative Receiver Project. Prior to leaving COMSAT Laboratories, he was the Assistant Manager of the Transponder Department. Presently, Dr. Childs is the Northeast Regional Manager for COMPACT Engineer, a division of COMSAT General Integrated Systems, where he is primarily involved in the development of new microwave CAD products.

Peter A. Carlton is an Assistant Engineer in the Microwave Communications Laboratory. Prior to joining COMSAT *Laboratories in March 1971, he served in the Army Microwave, Troposcatter Branch where he was assigned for the first troposcatter communication links in Viet Nam. He has been responsible for new circuit design and fabrication such as 3-dB interdigitated couplers on fused silica, integrated 14/4-GHz mixers, and the 14.5-GHz regenerative receiver. He has the following patents pending: periodic lid for integrated circuits and a temperature-compensated time delay element for application in a differentially coherent digital receiver. He has attended Montgomery College, Rockville, Maryland.*
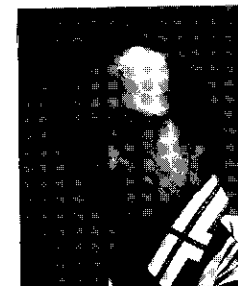
Robert Egri received the Dipl. Ing. from the Budapest Technical University. In 1976, he joined the Research Institute for Telecommunications in Budapest and worked for two years as a microwave engineer. Dr. Egri entered the Johns Hopkins University in Baltimore in 1977. After receiving his Ph.D. in 1978, he joined COMSAT Laboratories where he has been involved in the design of various microwave components for digital satellite applications.

Christoph Mahle received the Dipl. Ing. and Dr. S. C. Tech. degrees from the Swiss Federal Institute of Technology in 1961 and 1966, respectively. As Director of the Microwave Communications Laboratory at COMSAT Laboratories, he is responsible for directing research and development in such areas as high-technology microwave circuits and subsystems, analysis and laboratory verification of communications system performance of satellite transponders, and state-of-the-art of satellite communications transponders. He has participated in systems design and evaluation of the communications transponder design of the INTELSAT IV, IV-A, V, and COMSTAR programs. He has been responsible for the design, development, and testing of the transponder orbited on ATS-6 as part of the COMSAT Millimeter Wave Propagation Experiment. In addition, he advanced the state of the art of automated satellite in-orbit measurements. He is a member of IEEE.

Albert E. Williams received a B.E. in electrical engineering from the University of Western Australia, Perth, in 1962, and a Ph.D. from University College, London, England, in 1966. He is currently a Senior Staff Scientist, Microwave Technology, at COMSAT Laboratories, developing advanced microwave technology applicable to satellite communications systems. He was a joint recipient of the Institute (London) Sylvanus P. Thompson Premium award in 1966, and is currently a member of the IEEE and a senior member of the IEE.

Optimum feed locus for beam scanning in the symmetry plane of offset Cassegrain antennas: two-dimensional case*

V. KRICHEVSKY AND D. F. DIFONZO

Abstract

The paper presents analytical first- and second-order solutions describing the locus of feed positions in an offset Cassegrain antenna that produces best focusing for an *a priori* scanned beam direction. While the analysis is confined to beam scanning in the symmetry plane, the method is applicable to scanning in any direction as well as to other dual reflector antennas such as the offset Gregorian. First, the locus of feed positions that yields a chosen beam direction is determined. Then, the optimum position along this locus is found by minimizing the phase error with respect to the beam direction. The solutions can be represented in closed form in terms of the geometrical parameters of the antenna.

The first-order solution yields an optimum straight line along which the feeds should be located; the second-order solution yields a curved locus which was found to be a hyperbola for all of the cases considered. Computer analysis of several specific offset Cassegrain configurations confirms that the described

solutions provide better scanned beam performance as compared, for example, with the more conventional approach of transversely displacing the feed normal to the axis of a cone subtending the subreflector.

Introduction

The conventional offset-fed parabola has been the mainstay of frequency reuse communications satellite antennas because it provides a relatively simple means of producing multiple shaped beams with low sidelobes by using a number of feeds in the focal region and because its aperture can be made largely free of blockage [1]–[4]. The trend in such antenna systems is toward larger apertures and more closely spaced, isolated beams. For example, the 4-GHz offset parabola of the INTELSAT IV-A satellites [2] has an aperture of 1.34 m; it is expected that the diameter for the planned INTELSAT VI 4-GHz antenna will be greater than 3 m. To minimize the degradation of the scanned beams distributed over the $\pm 9°$ field of view of the earth as seen from geostationary orbit, the scanning limitations [5] of a single offset reflector require the focal length and the size of the feed array to increase with the aperture diameter.

Offset dual reflector antennas are receiving increased attention for multiple-beam applications because their folded geometry may offer packaging advantages. Also, the additional degree of freedom implied by the use of a second reflector surface may permit improved beam forming and polarization properties compared with those of single offset reflectors [6]–[9].

The offset Cassegrain antenna, consisting of offset sections of a paraboloidal main reflector and a hyperboloidal subreflector, is a candidate for spacecraft applications. It also has potential application as an earth station antenna which can access several satellites in geostationary orbit with a single aperture.

To assess the beam scanning performance limitations of this type of antenna, it is first necessary to determine the optimum location of the feed as it is displaced from the focus to produce a given off-axis beam direction. Unfortunately, the problem of the optimum feed position has not received extensive attention in the literature. For a single symmetrical paraboloid, it has been shown [10] that the feed should be located on the so-called Petzval surface, which is a paraboloidal surface tangent to the focal plane and having a focal length which is

one-half that of the reflector. Large lateral feed displacements in a symmetrical parabolic reflector have been studied [11] and Mrstik [12] has used numerical methods to investigate the optimum feed positions for the symmetrical paraboloid antenna. The optimum plane of the feed displacement for the offset paraboloid antenna is discussed in Reference 5. Ohm [13], using numerical analysis, implies that the feed locus for a particular offset Cassegrain antenna should be a spherical surface but provides no justification for this choice and no general results applicable to other antenna parameters. Wong [14] suggests that the equivalent parabola technique can be used to evaluate the beam scanning performance of a Cassegrain antenna for up to four beamwidths of scan. However, this technique loses its validity for large scan angles and specifically does not apply to other offset dual reflectors such as the offset Gregorian design [15]. In fact, it has been pointed out [16] that dual reflector antennas tend to be limited in absolute angle of scan rather than in scan expressed in units of the beamwidth.

This paper provides an analytical solution describing the optimum feed locus for the 2-dimensional case of beam scanning in an offset Cassegrain antenna. The 2-dimensional case assumes beam scanning in the plane of symmetry, which is also the plane of offset, and minimizes phase error only in the plane of symmetry. The analysis method can be extended to arbitrary scan directions as well as to other dual reflector geometries [17–18]. The solution to be described involves the assumptions of ray optics, beam scanning in the plane of symmetry, and small feed displacement.

Description of the problem

The geometry of an offset Cassegrain antenna is shown in Figure 1. The focal point F_1 is common for both reflectors and the origin of the cartesian coordinates coincides with the second hyperboloid focus F_2. A point source feed is assumed, which implies that all rays are radiated from a point. The source is located in the vicinity of the coordinate origin in the yz-plane, which is the plane of symmetry of both reflectors and also the plane of offset. The boundary of the subreflector is formed by the intersection of a hyperboloid and a cone with the vertex at the origin. The axis of the cone makes an angle θ_1 with the z-axis, and θ_2 is the half-angle of the cone (as shown in Figure 1). It is easy to show that the projection of the contour on the xy-plane is an ellipse. If the
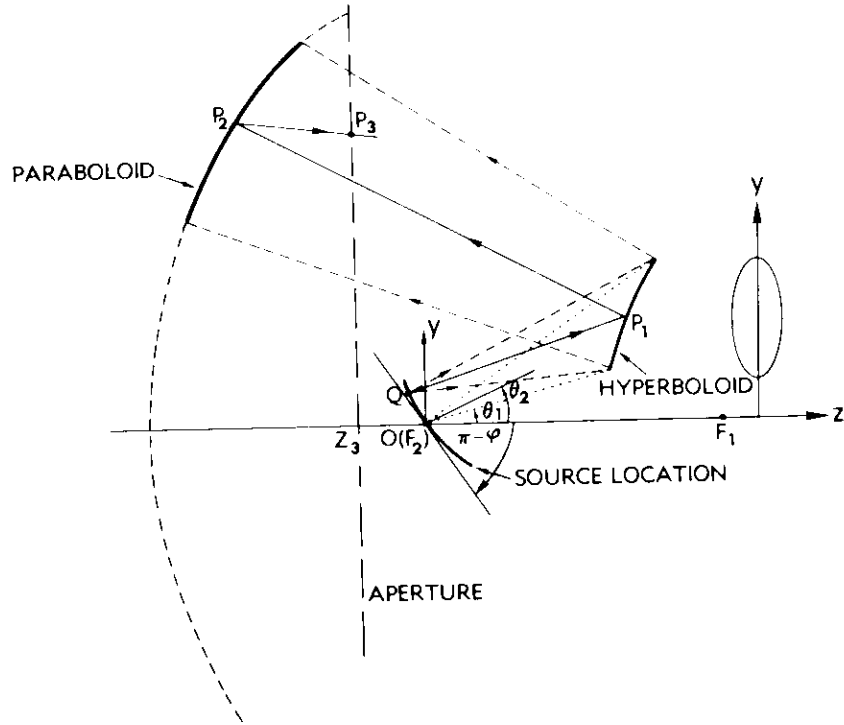
Figure 1. *Antenna Geometry*

cone vertex is shifted from the focus of the reflector, the projection of the contour on the *xy*-plane in the general case will be pear-shaped. The geometric size of the main reflector is not restricted, since it depends on the source location. It can be selected last with due consideration of all possible source locations. It is assumed that all rays reflected by the subreflector are intercepted by the main reflector.

Solution of the problem

The solution of the problem consists of finding

  a. the loci of feed positions that yield specific beam directions,
  b. the locus that yields minimum aperture phase error.

The intersection of these two loci is the optimum feed position for a specified beam direction.

The rays can be traced in the symmetry plane to find the locus giving a specified beam direction. Consider any ray which is radiated by a point source at $Q(0, y_0, z_0)$ (see Figure 1) and in the *yz*-plane. Assume that it strikes the hyperboloid at point $P_1(0, y_1, z_1)$. The direction of the ray is given by the unit vector

$$\hat{z}_1 = \frac{\hat{y}(y_1 - y_0) + \hat{z}(z_1 - z_0)}{L_1} \tag{1}$$

where L_1 is the distance between Q and P_1:

$$L_1 = \sqrt{(y_1 - y_0)^2 + (z_1 - z_0)^2} \quad . \tag{2}$$

In accordance with the laws of geometrical optics, the ray is reflected by the subreflector surface, strikes the main reflector at point $P_2(0, y_2, z_2)$, crosses over and intersects the aperture plane at some point $P_3(0, y_3, z_3)$. The total path length of the ray between the source point and the aperture point is

$$L = \sum_{i=1}^{3} L_i \tag{3}$$

where $\quad L_i = \sqrt{(y_i - y_{i-1})^2 + (z_i - z_{i-1})^2} \quad , \quad i = 1, 2, 3 \quad . \tag{4}$

The total path lengths of rays which strike the upper and lower points of the primary reflector are L_u and L_l, respectively; the *y*-coordinates of the points where they intersect the aperture plane are y_u and y_l; and $L_{u,l}$ and $y_{u,l}$ are functions of the antenna parameters and also of the feed position. If the feed is located at the focus, the upper and lower rays arrive at the aperture plane with equal path lengths. If the source is located away from the focus, the path lengths are different. For a small beam scan angle, produced by small feed displacement, it is possible to write approximately

$$\alpha \approx \frac{L_u - L_l}{y_u - y_l} \tag{5}$$

(see Figure 2). For small feed displacement, the following series expansions hold:
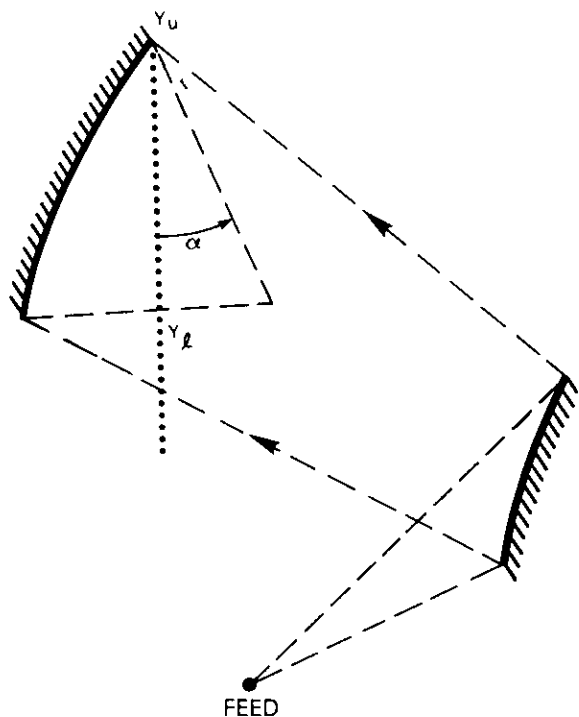
Figure 2. *Definition of the Beam Scan Angle*

$$L = L^{(0)} \sum_{m=0}^{\nu} \sum_{k=0}^{m} C_{m,k} \, y_0^k \, z_0^{m-k} \tag{6}$$

$$y = y^{(0)} \sum_{m=0}^{\nu} \sum_{k=0}^{m} T_{m,k} \, y_0^k z_0^{m-k} \tag{7}$$

where $L^{(0)}$, $y^{(0)}$ are the values of L and y when the feed is positioned at the focus. Now, consider two cases:

  a. $\nu = 1$ for the first-order approximation, corresponding to $R/F_H \ll 1$;

  b. $\nu = 2$ for the second-order approximation, corresponding to $(R/F_H)^2 \ll 1$;

where $R = \sqrt{y_0^2 + z_0^2}$ = feed displacement from focus

F_H = focal length of the hyperboloid.

Introducing equations (6) and (7) into equation (5) for the upper and lower rays yields the feed locus for a constant beam scan angle

$$\alpha = \sum_{m=1}^{\nu} \sum_{k=0}^{m} A_{m,k} \, y_0^k \, z_0^{m-k} \quad . \tag{8}$$

The coefficients $A_{m,k}$ have been found in closed form directly in terms of the parameters of the offset reflector and are represented explicitly in Appendix A. Equation (8) can be easily solved for y_0 in terms of z_0, α, and $A_{m,k}$, and the equation for the constant beam direction feed locus can be written as

$$y_0 = f_\nu(z_0, \alpha, A_{m,k}) \quad . \tag{9}$$

For the first-order approximation ($\nu = 1$), the locus is a straight line.

Figures 3 and 4 show loci of the constant beam direction for a few beam scan angles and the same set of antenna parameters but with two different paraboloid focal lengths: $F_p = 140\lambda$ and $F_p = 100\lambda$. All antenna parameters are displayed on Figures 3 and 4. The first approximation is shown by a dotted line, and the second approximation by a solid line. Both lines intersect at some point, and the angle between them diverges with increasing absolute value of scan angle. Comparing these loci indicates that, to achieve the same scan angle, the feed should be moved farther from the focus for the larger paraboloid focal length.

Figures 5 and 6 illustrate the accuracy of the constant beam scan angle loci for both approximations as verified by computer pattern analysis of the specific offset reflector geometries. The feed is moving along the y-axis, and the figures represent the accuracy in beam pointing vs scan beam angle. For example, for $F_p = 140\lambda$ and a $-5°$ scan beam angle, the first-order approximation gives an error of about $1.4°$, while the error for the second-order approximation is only $0.06°$.

To derive the optimum feed locus in the 2-dimensional case, the arc of the angle subtended by the subreflector from the focus ($2\theta_s$) is divided into n increments. On the arc in the yz-plane, there are $n - 1$ points. Straight lines through these points and the focal point
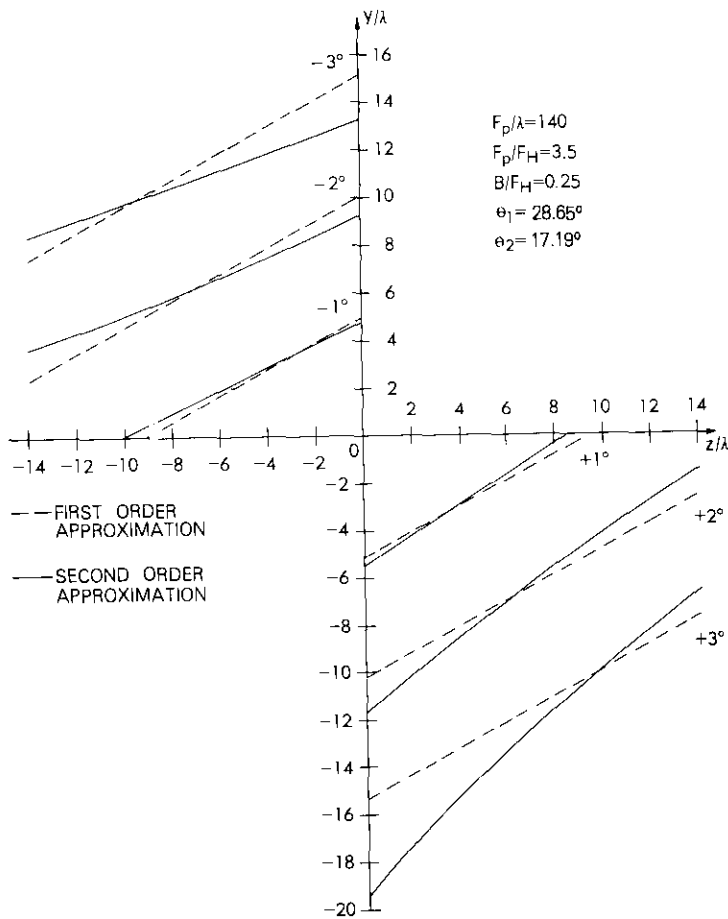
Figure 3. *Constant Beam Direction Loci for $F_p = 140\lambda$*

would intersect the subreflector in $n - 1$ points. The rays can be traced from the feed to those points, and then to the main reflector and aperture plane. Consider the antenna under investigation as the sum of n small antennas, each separated by any two adjacent rays. The rays which are reflected from the upper and lower points of the subreflector are also included. The results obtained in the first step of the solution can be used for every small antenna after the following substitutions:
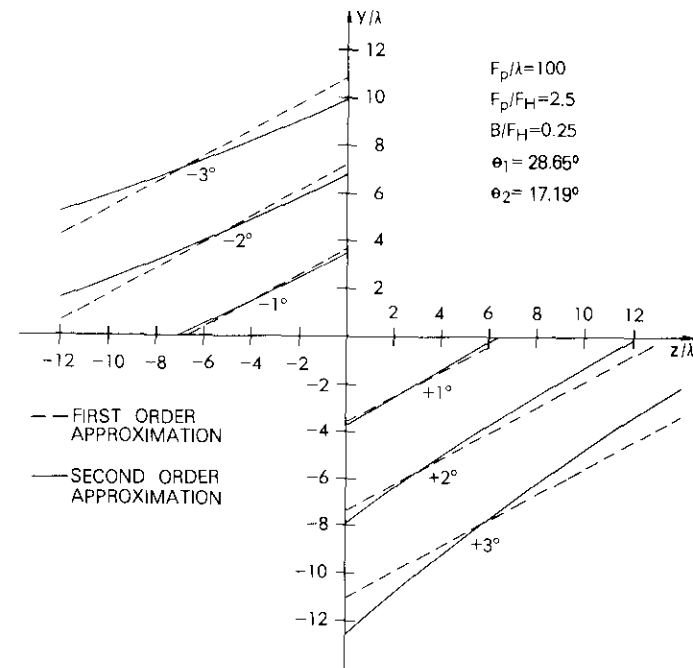
Figure 4. *Constant Beam Direction Loci for $F_p = 100\lambda$*

$$\theta_{2,n} = \frac{\theta_2}{n} \to \theta_2$$

$$\theta_{1,m,n} = \frac{\theta_2}{n}(2m - 1) + \theta_1 - \theta_2 \to \theta_1 \tag{10}$$

where m is the number of the ray ($1 \le m \le n$).

The directions produced by each small antenna are generally different, but it is possible, for any beam pointing direction, to find the feed position which minimizes their difference. That is, the scan angle for every small antenna is denoted by $\alpha_{m,n}$, where m indicates the number of the subsequent antenna, and the constraint is

$$G(y_0, z_0) = \lim_{n \to \infty} \left\{ \frac{1}{n} \sum_{m=1}^{n} (\alpha_{m,n} - \alpha)^2 \right\} \tag{11}$$
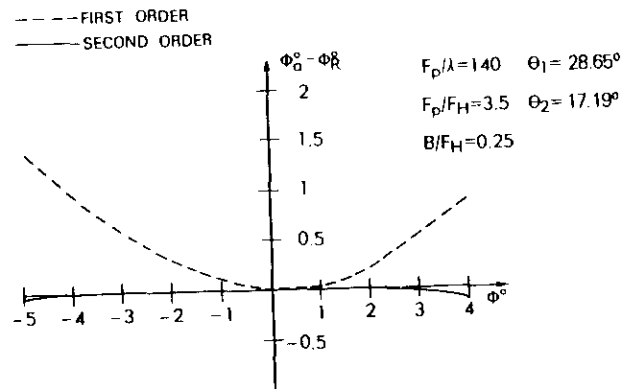
Figure 5. *Accuracy Comparison for the Constant Beam Scan Angle Loci for Both Approximations, $F_p = 140\lambda$*
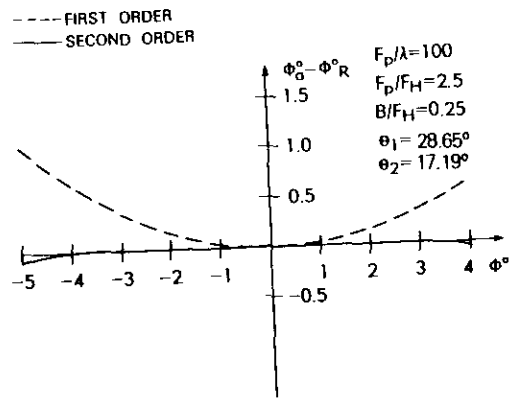
Figure 6. *Accuracy Comparison for the Constant Beam Scan Angle Loci for Both Approximations, $F_p = 100\lambda$*

where α is given by equation (8). The solution of the problem is subject to the restriction that the feed is also located on the locus of the constant beam direction [equation (9)]; therefore, the function which is to be minimized is

$$I(y_0, z_0, \mu) = G(y_0, z_0) + \mu[y_0 - f_i(z_0, \alpha, A_m, k)] \tag{12}$$

where μ is a Lagrangian multiplier.

The constraint $G(y_0, z_0)$ consists of simple trigonometric and algebraic functions, and the summation in equation (11) can be performed so that $G(y_0, z_0)$ can be easily written in closed form [19]. The optimum feed position of the feed satisfies the conditions

$$\frac{\partial I(y_0, z_0, \mu)}{\partial y_0} = Q_1(y_0, z_0, \mu) = 0 \tag{13a}$$

$$\frac{\partial I(y_0, z_0, \mu)}{\partial z_0} = Q_2(y_0, z_0, \mu) = 0 \ . \tag{13b}$$

Elimination of μ in equations (13a) and (13b) leads immediately to an analytical form of the optimum locus for the feed position

$$\sum_{m-1}^{v} \sum_{k-0}^{m} l_{m,k} Y_0^k Z_0^{m-k} = 0, \qquad v = 1, 2 \tag{14}$$

where the coefficients $l_{m,k}$ are found in closed form (see Appendix B).

As previously stated, $v = 1$ corresponds to the first-order approximation, which is a straight line, and $v = 2$ corresponds to the second-order approximation. Figure 7 represents both approximations of the optimum locus and constant beam direction loci for a few angles for the set of parameters $F_p = 100\lambda$, $F_p = 2.5F_H$, $B = 0.25F_H$, $\theta_1 = 28.65°$, $\theta_2 = 17.19°$, where F_p is the focal length of the main reflector, F_H is the focal length of the subreflector, and B is half the distance between two vertices of the hyperboloid.

There is also a straight line which is normal to the axis of the cone subtended by the subreflector as seen from the focus (dotted line). Figures 8–11 compare the patterns in the plane of symmetry for several feed positions on the constant beam direction loci and a few specific values of scan angle ($\pm 4°$ and $\pm 6°$). It can be seen that positioning the feed at the optimum (second order) locus results in the narrowest main beam, the lowest sidelobes, and the deepest nulls. A dual mode circular waveguide (Potter horn) with radius $a = 2.3\lambda$ is used as the feed. To minimize spillover, the waveguide axis is chosen to bisect the angle subtended by the subreflector as seen from the feed position. The feed aperture polarization is oriented along the x-axis. The first-order "optimum" locus position is not as good as the second-order approximation, but is better than other positions that give the same beam pointing.

$F_p = 100\lambda$ $\theta_1 = 28.65°$
$F_p/F_H = 2.5$ $\theta_2 = 17.19°$
$B/F_H = 0.25$

BLOCKAGE LIMIT

－－－ FIRST ORDER

─── OPTIMUM
SECOND ORDER

······· NORMAL TO
AXIS OF CONE
SUBTENDING
SUBREFLECTOR
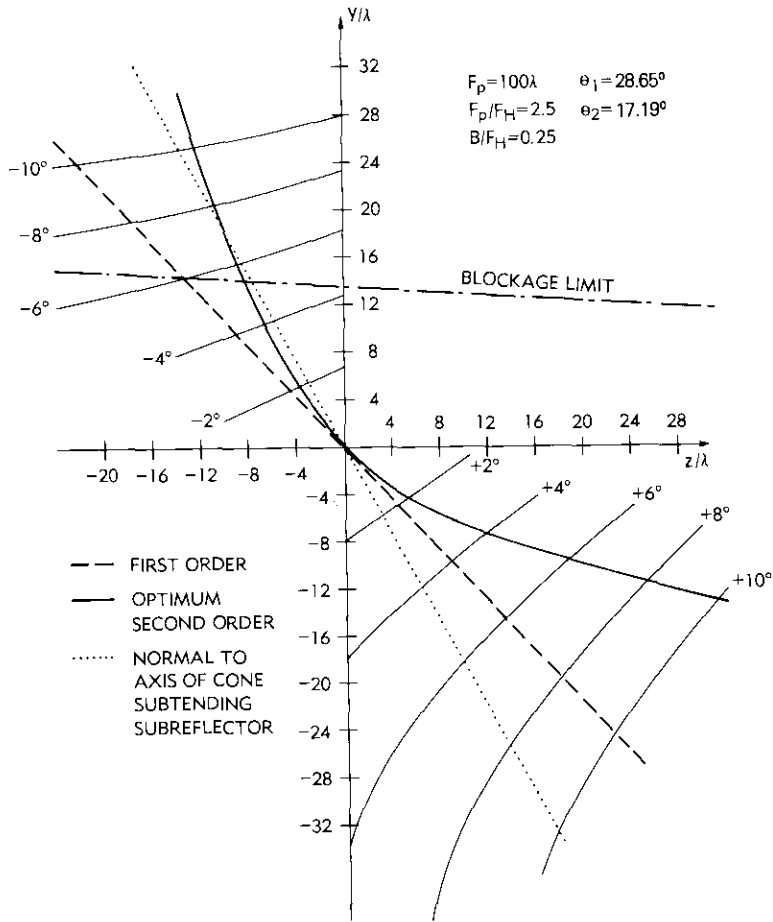
Figure 7. *Optimum Locus and Constant Beam Direction Loci for a Few Angles (Both Approximations)*

Figure 12 depicts the scanned beams for the feed displaced along the optimum locus of the second-order approximation. Figure 13 shows the scanned beams for the feed displaced along the optimum locus of the first-order approximation, and Figure 14 shows the effect of moving the feed along a line normal to the axis of the cone subtending
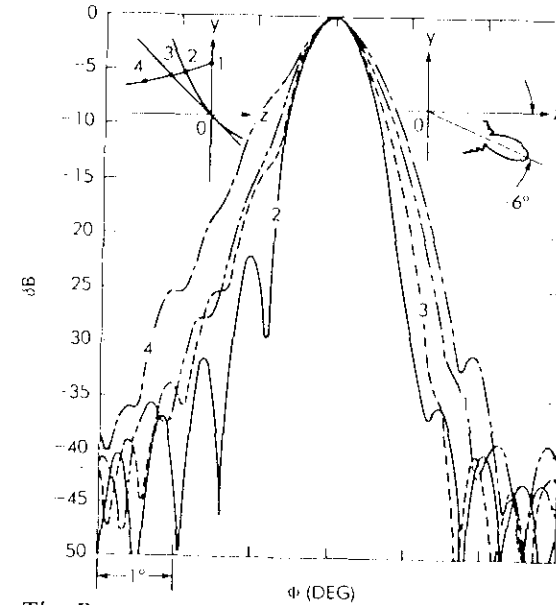
Figure 8. *The Pattern in the Plane of Symmetry for the Feed at Several Positions, Scan Angle $= -6°$*
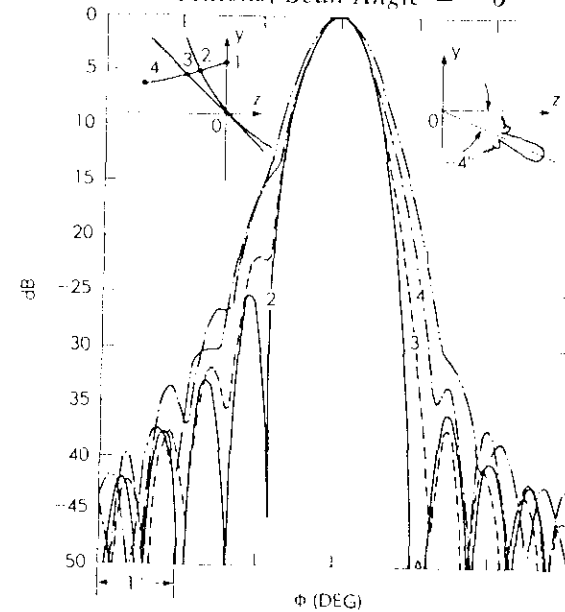
Figure 9. *The Pattern in the Plane of Symmetry for the Feed at Several Positions, Scan Angle $= -4°$*
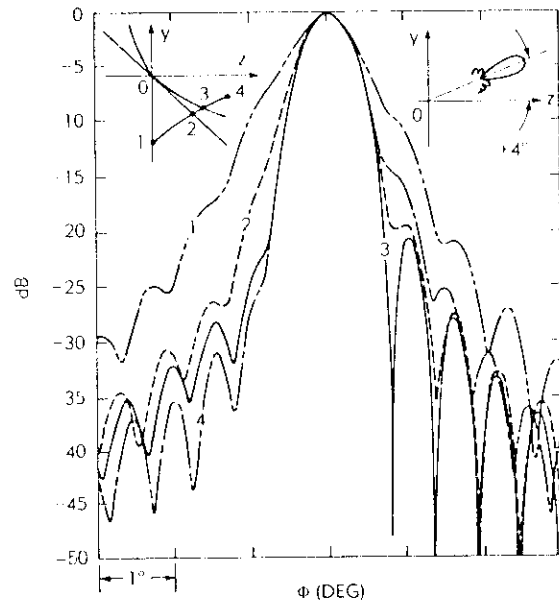
Figure 10. *The Pattern in the Plane of Symmetry for the Feed at Several Positions, Scan Angle = +4°*
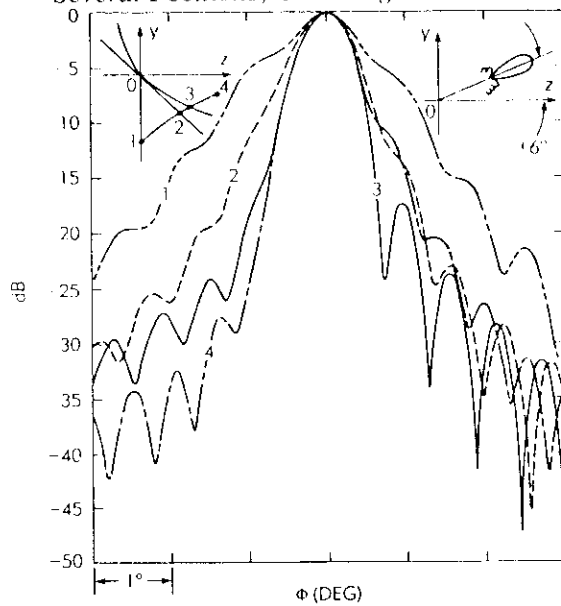
Figure 11. *The Pattern in the Plane of Symmetry for the Feed at Several Positions, Scan Angle = +6°*
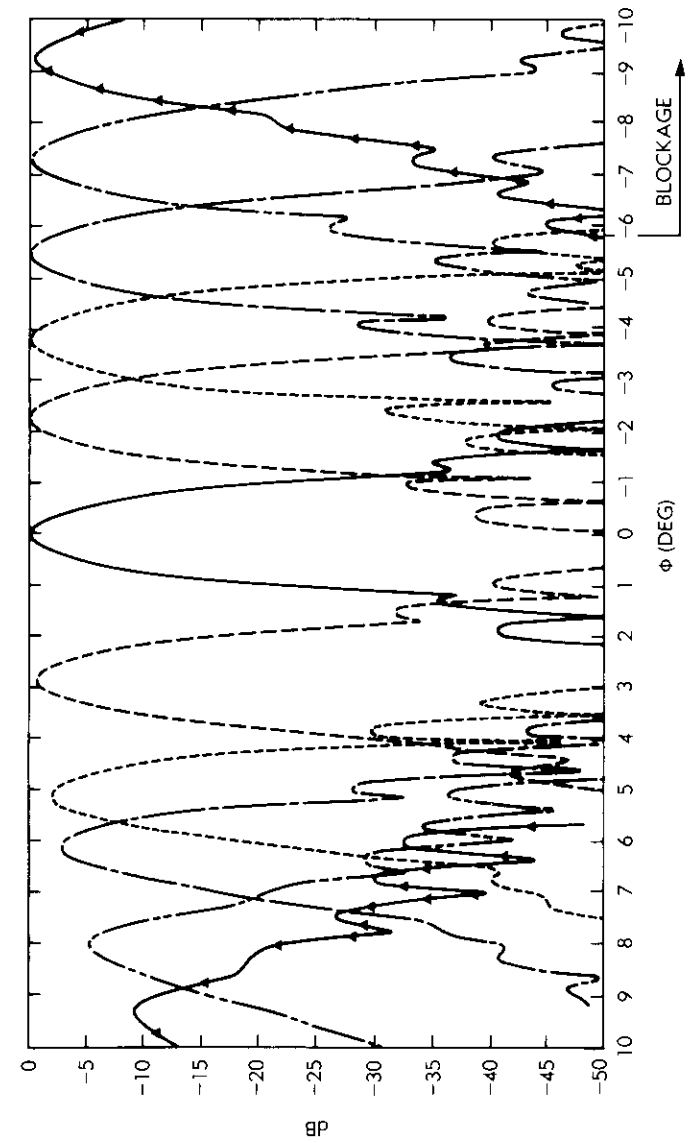
Figure 12. *Scanned Beams for Offset Cassegrain with Feed Displaced Along the Second-Order Approximation Optimum Locus (hyperbola)*
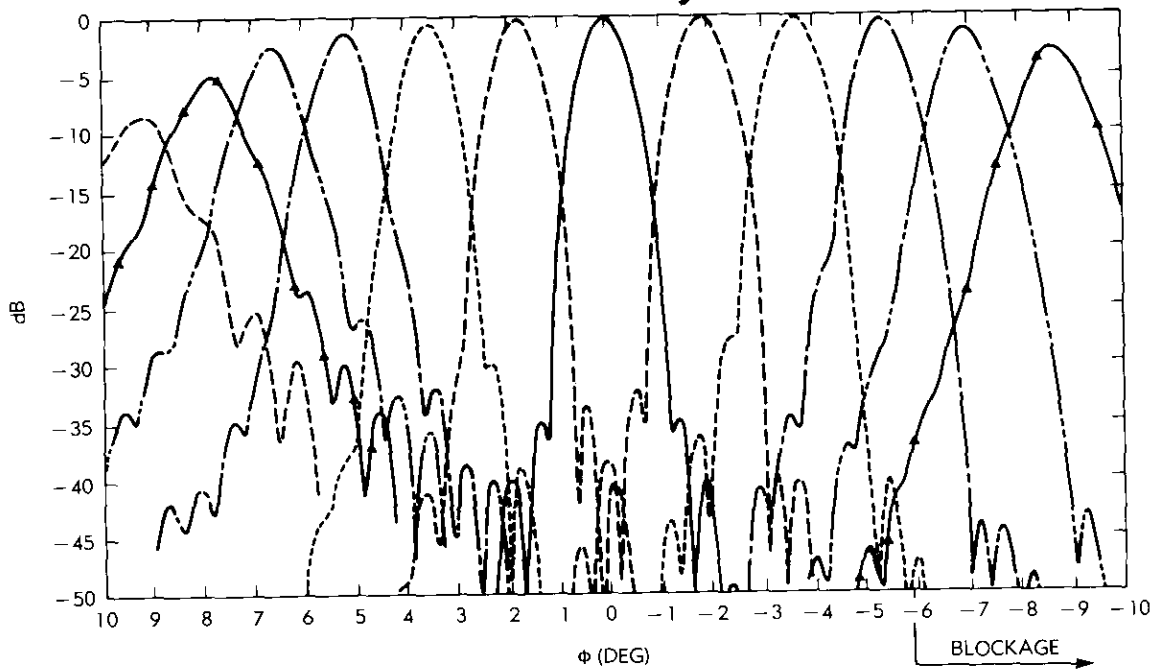
Figure 13. *Scanned Beams for Offset Cassegrain with Feed Displaced Along First-Order Approximation Optimum Locus (straight line)*
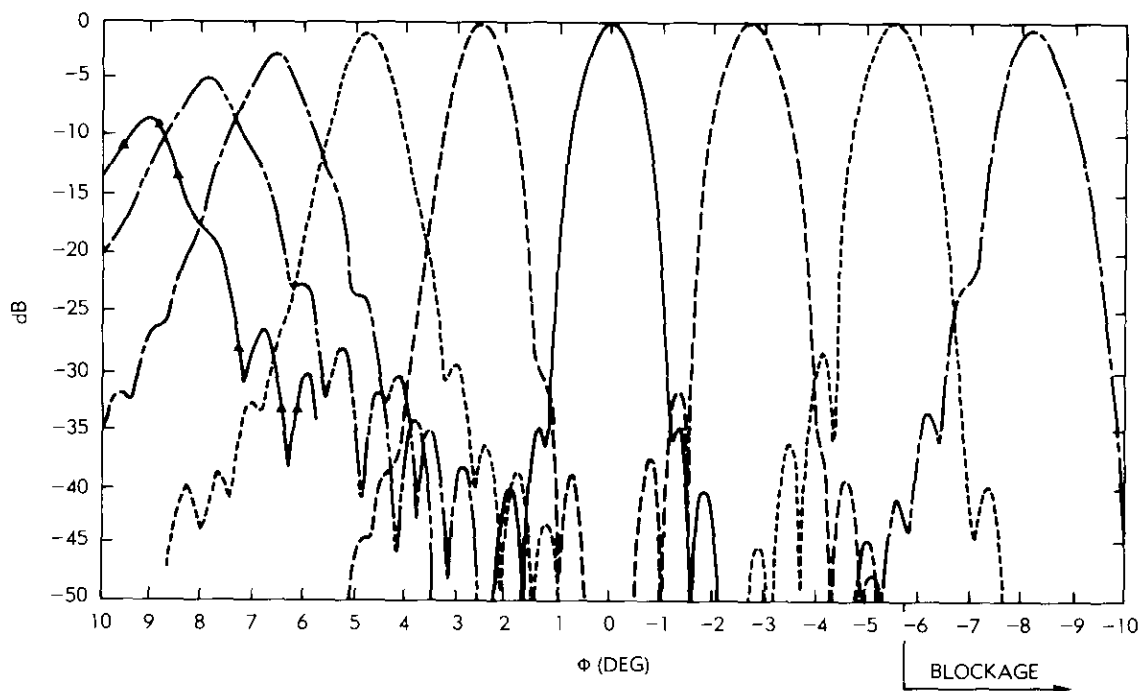
Figure 14. *Scanned Beams for Offset Cassegrain with Feed Displaced Along Normal to Axis of Cone Subtending the Subreflector* $(\theta_1 + \pi/2)$

the subreflector. The feed is a Potter horn with radius $a = 3.1\lambda$. Figure 15 compares the beam performance in the scan plane for the Cassegrain antenna with parameters given by Ohm [13]. A Potter horn with radius $a = 2.3\lambda$ was used as the feed. While the gains and cross-polarization levels of the two beams are similar, it can be seen that the optimum feed position produces a sharper beam (deeper nulls) than the feed position implied in Reference 13.

Canonical form of the second-order approximation of optimum locus

A new coordinate system will be introduced which is formed by rotating the old system around the x-axis at an angle

$$\phi = 0.5 \tan^{-1} \left(\frac{2l_{2,1}}{l_{2,0} - l_{2,2}} \right) \tag{15}$$

where the coefficients $l_{2,k}$, $k = 0, 1, 2$ are defined in Appendix B. The optimum locus can easily be written in canonical form in the new coordinate system (x', y', z'):

$$\frac{(z_0' - z_c)^2}{d_{z1}} + \frac{(y_0' - y_c)^2}{d_{y1}} = 1 \tag{16}$$

where

$$d_{z1} = \frac{R^2}{A^-} \tag{17}$$

$$d_{y1} = \frac{R^2}{A^+} \tag{18}$$

$$R^2 = 0.25 \left(\frac{C^2}{A^-} + \frac{D^2}{A^+} \right) \tag{19}$$

$$A^{\pm} = \frac{l_{2,2} + l_{2,0}}{2} \mp \cos(2\phi) \left[\frac{l_{2,2} - l_{2,0}}{2} - l_{2,1} \tan(2\phi) \right] \tag{20}$$

$$C = (l_{1,1} \tan \phi + l_{1,0}) \cos \phi \tag{21}$$

$$D = (l_{1,1} - l_{1,0} \tan \phi) \cos \phi \tag{22}$$

$$z_c = -\frac{C}{2A^-} \tag{23}$$
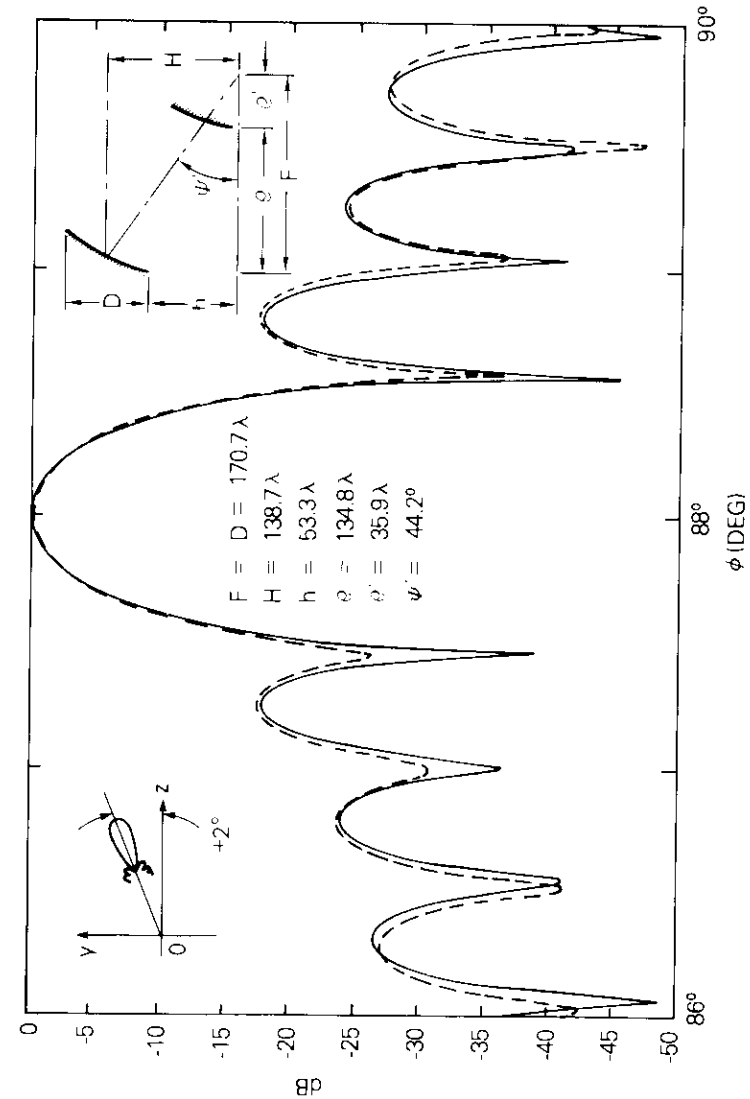
Figure 15. Patterns in the Scan Plan for Antenna Feed Locations (solid line) and Locus Utilized by Ohm [13] (dashed line)

$$y_c = -\frac{D}{2A^-} \quad . \tag{24}$$

The vertex of the locus coincides with the origin in the (x, y, z) coordinate system where the first- and second-order solutions intersect and the y'-axis is parallel to the first-order approximation locus, which is a straight line only if

$$\frac{l_{2,1}}{l_{2,0} - l_{2,2}} = \frac{l_{1,1}l_{1,0}}{l_{1,0}^2 - l_{1,1}^2} \quad . \tag{25}$$

Equation (16), which represents the second-order line, could be a hyperbola or an ellipse depending on the sign of the ratio d_{-1}/d_{v1}. (A circle is a special case of an ellipse.) For all sets of parameters studied, the sign was found to be minus; therefore, the locus is a hyperbola (see, for example, Figure 7). That ratio was also calculated for several other sets of antenna parameters:

$$0.1 \le \beta \le 0.6 \quad , \qquad 1 \le \frac{F_p}{F_{\mu}} \le 4 \quad , \qquad 80 \le \frac{F_p}{\lambda} \le 160 \quad .$$

In every set of antenna parameters the sign was minus, i.e., the optimum locus was a hyperbola.

Conclusions

The optimum feed position in offset Cassegrain antennas has been found in analytical form directly in terms of the reflector parameters for a priori specified beam directions and 2-dimensional beam scanning in the plane of symmetry. The results have been verified using computer analysis of the far-field patterns. The method which was developed can be extended to other dual reflector antennas and to general beam scanning in any direction.

The results can be applied to the design of multibeam and shaped beam antenna systems. Locating the cluster of feeds on the optimal feed loci permits the sharpest beams and minimum scan loss, which can contribute to the formation of shaped beams with high isolation between closely spaced shaped beams. Furthermore, based on the optimum feed locus, it is possible to assess the ultimate scanned beam performance that can be achieved with a conventional offset Cassegrain

antenna. This knowledge then provides a sound basis for exploring alternative microwave optics approaches to multiple-beam antennas.

References

[1] R. W. Kreutel et al., "Antenna Technology for Frequency Reuse Satellite Communications," *Proc. IEEE*, Vol. 65, No. 3, March 1977, pp. 370–378.
[2] F. Taormina et al., "INTELSAT IV-A Communications Antenna—Frequency Reuse through Spatial Isolation," ICC '76 *Conference Digest*, Vol. I, pp. 4-10—4-14.
[3] G. H. Schennum and H. T. Ward, "INTELSAT V Spacecraft Antenna Subsystem," ICC '80 *Conference Digest*, Vol. 2, pp. 25.1.1–25.2.6.
[4] A. W. Rudge and N. A. Adatia, "Offset-Parabolic-Reflector Antennas: A Review," *Proc. IEEE*, Vol. 66, No. 12, December 1978, pp. 1592–1618.
[5] R. Mittra et al., "An Efficient Technique for the Computation of Vector Secondary Patterns of Offset Paraboloid Reflectors," *IEEE Transactions on Antennas and Propagation*, AP-27, May 1979, pp. 294–304.
[6] B. S. Wescott and F. Brickell, "Dual Reflectors for Shaped Beams and Zero Cross-Polarization," *IEEE Proceedings on Microwaves, Optics, and Acoustics*, Vol. 3, No. 6, November 1979, pp. 247–252.
[7] V. Galindo-Israel, R. Mittra, and A. G. Cha, "Aperture Amplitude and Phase Control of Offset Dual Reflectors," *IEEE Transactions on Antennas and Propagation*, AP-27, 1979, pp. 154–164.
[8] Y. Mizuguchi, M. Akagawa, and H. Yokoi, "Offset Gregorian Antenna," *Electronics and Communications in Japan*, Vol. 61-B, No. 3, 1978, pp. 58–66.
[9] T. Takano et al., "Offset Cassegrain Earth Station Antenna for the Japanese Domestic Satellite Communication System, *IEEE Transactions on Communications*, COM-28, No. 6, June 1980, pp. 883–889.
[10] J. Ruze, "Lateral-Feed Displacement in a Paraboloid," *IEEE Transactions on Antennas and Propagation*, AP-13, September 1965, pp. 660–665.
[11] W. Imbriale, P. Ingerson, and W. Wong, "Large Lateral-Feed Displacements in a Parabolic Reflector," *IEEE Transactions on Antennas and Propagation*, AP-22, November 1974, pp. 742–745.
[12] A. Mrstik, "Scan Limits of Off-Axis Fed Parabolic Reflector," *IEEE Transactions on Antennas and Propagation*, AP-27, September 1979, pp. 647–651.
[13] E. Ohm, "System Aspects of a Multibeam Antenna for Full U.S. Coverage," International Conference on Communications, June 10–14, 1979, Boston, Massachusetts.

[14] W. C. Wong, "On the Equivalent Parabola Technique to Predict the Performance Characteristics of a Cassegrain System with an Offset Feed," *IEEE Transactions on Antennas and Propagation*, AP-21, May 1973, pp. 335–339.

[15] M. Akagawa and D. F. DiFonzo, "Beam Scanning Characteristics of Offset Gregorian Antennas," IEEE Antennas & Propagation Society Symposium, University of Washington, Seattle, Washington, June 18–22, 1979.

[16] W. D. White and L. K. DeSize, "Scanning Characteristics of Two-Reflector Systems," 1962, *IRE Convention Record*, Pt. 1, pp. 44–70.

[17] V. Krichevsky and D. F. DiFonzo, "Optimum Feed Locus for Beam Scanning in Offset Cassegrain Antenna," International IEEE/APS Symposium on Antennas and Propagation, 1980, *Proc.*, pp. 553–556.

[18] V. Krichevsky and D. F. DiFonzo, "Optimum Feed Locus for General Three-Dimensional Beam Scanning in Offset Cassegrain Antenna," International IEEE/APS Symposium, Los Angeles, California, June 15–19, 1981.

[19] M. Abramowitz and I. Stegun, *Handbook of Mathematical Tables*, National Bureau of Standards, December 1972.

Appendix A. *Analytical expressions of the coefficients in series expansions of beam scan angle*

$$a_{1,0} = \chi_t \sin \theta_1 (\cos \theta_1 + \cos \theta_2)$$

$$a_{1,1} = -a_{1,0} \cot \theta_t$$

$$a_{2,0} = -a_{1,0} H$$

$$a_{2,1} = -\frac{a_{1,t}}{2 \cos \theta_1 \sin \theta_2} R$$

$$a_{2,2} = -a_{1,0} V$$

where

$$\chi_t = \frac{1 - \beta}{2F_p(1 + \beta)}$$

$$H = \frac{-1}{F_n \eta^2} \left\{ \eta_+(q_3 - 1) - \beta q_1 q_4 + \beta \eta_+ - \left(\frac{q_1}{2} - \sin^2 \theta_t \right) \right.$$

$$(3\eta_+ - 2 - 2\beta q_1) - 2\beta q_2 \Big\} + \frac{1}{4\eta_-^{(1)2} F_p} \Big\{ \eta_.(q_6 - 1) - 2\beta [(q_4 - 1)$$

$$(1 + q_1) + q_2] - [\cos \theta_1 + \cos (2\theta_1) \cos \theta_2] \frac{2 \cos (s/2)}{\cos (t/2)}$$

$$\cdot (\eta_- - 2\beta \cos t) + \eta_+^{(1)2} Q_s(Q_s - 4 \sin \theta_1) \Big\}$$

$$V = \frac{1}{F_n \eta^2} \left\{ \eta_- q_3 - \beta q_1(1 + q_4) - \frac{\cos \theta_1}{2 \cos(t/2) \cos(s/2)} \right.$$

$$[- \beta \eta_+ + q_5(3\eta_+ - 2 - 2\beta q_1) + 2\beta q_2] \Big\}$$

$$+ \frac{1}{4\eta_+^{(1)2} F_p} \Big\{ - \eta_. q_6 + 2\beta[q_4(1 + q_1) + q_2]$$

$$+ \eta_+^{(1)2} Q_c(Q_c - 2 \cos \theta_1) + (2 \cos^2 \theta_1 + q_2)(\eta_+ - 2\beta q_1) \Big\}$$

and

$$q_i = \mu_1 \cos^2 t + \mu_2 \cos^2 s + \mu_3 \cos t \cos s + \mu_4 \cos t + \mu_5 \cos s$$

$$q_1 = \{0, 0, 0, 1, 1\} \quad , \qquad q_4 = \{1, 1, 0, 0, 0\}$$

$$q_2 = \{0, 0, 1, 0, 0\} \quad , \qquad q_5 = \{0, 0, 1, 1, 1\}$$

$$q_3 = \{1, 1, 1, 0, 0\} \quad , \qquad q_6 = \{1, 1, 1, 1, 1\}$$

$$\eta_\pm = (1 \pm \beta^2) \quad , \quad \eta_\pm^{(1)} = 1 \pm \beta$$

$$\begin{Bmatrix} Q_c \\ Q_s \end{Bmatrix} = \frac{\cos(s/2)}{\cos(t/2)} \begin{Bmatrix} \cos s \\ \sin s \end{Bmatrix}$$

$$R = \frac{1}{F_H \eta_\pm^2} \left\{ -P_t^{(1)} + P_s^{(1)} + \cos\frac{t}{2}\cos\frac{s}{2}(P_{ts}^{(2)} - P_{st}^{(2)}) \right\}$$

$$+ \frac{1}{2F_{pt}\eta^{(1)2}} \left\{ \frac{1}{2}(P_t^{(3)} - P_s^{(3)}) - 2\cos\frac{t}{2}\cos\frac{s}{2}(P_{ts}^{(4)} - P_{st}^{(4)}) \right.$$

$$\left. - 2\eta_\pm^{(1)2} \frac{(\cos t - \cos s)\cos(s/2)}{4\cos t/2}(2\sin s\, Q_c - 2U_{st}^{(5)}) \right\}$$

$$P_t^{(1)} = U_{tt}^{(5)} U_1 U_2 \quad , \quad P_t^{(3)} = U_3 U_4 U_{tt}^{(5)}$$

$$P_{ts}^{(2)} = \frac{U_1 U_3}{1 + \cos t} U_{ts}^{(5)} \quad , \quad P_s^{(3)} = P_t^{(3)} \Big|_{s \to t}$$

$$P_{st}^{(2)} = P_{ts}^{(2)} \Big|_{\substack{t \to s \\ s \to t}} \quad , \quad P_{ts}^{(4)} = U_3 U_{ts}^{(5)}$$

$$P_{st}^{(4)} = P_{ts}^{(4)} \Big|_{\substack{t \to s \\ s \to t}}$$

$$U_1 = \cos t - \beta \quad , \quad U_{ts}^{(5)} = \sin\frac{3t + s}{2}$$

$$U_2 = 1 - \beta\cos t \quad , \quad U_{tt}^{(5)} = \sin 2t$$

$$U_3 = 1 - 2\beta\cos t + \beta^2$$
$$U_4 = 1 + \cos t$$
$$t = \theta_1 + \theta_2$$
$$S = \theta_1 - \theta_2$$

Appendix B. Analytical expression of the coefficients used in the optimum feed locus presentation

$$l_{1,0} = -f_8 a_{1,1} + f_6 a_{1,0} + f_2 a_{1,0} a_{1,1} - f_1 a_{1,0}^2$$

$$l_{1,1} = f_7 a_{1,0} - f_6 a_{1,1} - f_1 a_{1,0} a_{1,1} + f_2 a_{1,1}^2$$

$$l_{2,0} = -3f_{10} a_{1,1} + 2f_8 a_{1,0} a_{1,1} + f_2(a_{1,1} a_{2,0} + a_{1,0} a_{2,1})$$
$$- f_8 a_{2,1} + f_{12} a_{1,0} - f_3 a_{1,0}^2 - 3f_1 a_{1,0} a_{2,0} + 2f_6 a_{2,0}$$

$$l_{2,1} = (f_{11} a_{1,0} - f_{12} a_{1,1}) - (f_4 a_{1,0}^2 - f_5 a_{1,1}^2)$$
$$- a_{2,1}(f_1 a_{1,0} - f_2 a_{1,1}) + a_{2,0}(f_7 - f_1 a_{1,1})$$
$$- a_{2,2}(f_8 - f_2 a_{1,0})$$

where

$$f_j = \chi_1 \sum_{k=0}^{2} T_{j,k} L_k^{(j)} \quad , \quad j = 1, 2$$

$$4f_j = \chi_1 \sum_{k=0}^{4} T_{j,k} L_k^{(j)} \quad , \quad j = 3, 4, 5$$

$$f_j = \chi_1^2 \sum_{k=0}^{4} T_{j,k} L_k^{(j)} \quad , \quad j = 6, 7, 8$$

$$8f_j = \chi_1^2 \sum_{k=0}^{4} T_{j,k} L_k^{(j)} \quad , \quad j = 9, 10, 11, 12$$

and

$$L_k^{(j)} = \frac{\sin(k\theta_2)}{(k\theta_2)} \cdot \begin{Bmatrix} \cos(k\theta_1) \\ \sin(k\theta_1) \end{Bmatrix} \quad , \quad \begin{matrix} j = 1, 3, 7, 8, 10, 11 \\ j = 2, 4, 5, 6, 9, 12 \end{matrix}$$

$$T_{1,0} = T_{1,2} = -T_{2,2} = T_{6,1} = T_{6,3} = -T_{7,3} = -T_{8,1} = T_{8,2} = T_{8,3} = -0.5$$

$$-T_{1,1} = T_{2,1} = T_{7,2} = 1$$

$$T_{2,0} = T_{6,0} = 0, T_{6,2} = -0.75$$

$$T_{6,4} = -T_{7,4} = T_{8,4} = -0.125$$

$$T_{7,0} = 0.875, T_{7,1} = 1.5, T_{8,0} = 0.625$$

$$T_{4,0} = T_{5,0} = T_{9,0} = T_{12,0} = 0$$

$-0.5(T_{3,0}) = \{0, 1, 1, 0, -1\}$, $0.5(T_{3,1}) = \{2, 1, 0, 1, 2\}$,

$0.5(T_{3,2}) = \{2, -1, -1, 1, 0\}$, $-0.5(T_{4,2}) = \{1, 0, 0, 1, -1\}$,

$T_{5,1} = \{4, 5, 2, 1, 6\}$, $0.5(T_{5,2}) = \{1, -1, -2, 0, 1\}$,

$0.5(T_{3,4}) = -T_{4,4} = T_{5,4} = \{0, 0, 1, 1, -1\}$,

$-0.5(T_{3,3}) = T_{4,1} = T_{4,3} = -T_{5,3} = \{0, 3, 2, -1, 2\}$

$T_{9,1} = \{2, -3, -2, 3, -4\}$, $2T_{9,2} = \{4, -12, -7, 9, -13\}$,

$2T_{9,3} = \{4, -9, -4, 9, -12\}$, $T_{9,4} = \{1, -3, -1, 3, -4\}$,

$2T_{9,5} = \{0, -3, 0, 3, -4\}$, $2T_{9,6} = \{0, 0, 1, 1, -1\}$,

$T_{10,0} = \{5, 4, 0, 1, 7\}$, $T_{10,1} = \{4, -1, -4, 1, 4\}$,

$-2T_{10,2} = \{8, 16, 7, -1, 13\}$, $-2T_{10,3} = \{8, 1, -8, -1, 12\}$,

$-T_{10,4} = \{1, -4, -4, 1, -1\}$, $T_{10,5} = -T_{9,5}, T_{10,6} = -T_{9,6}$

$T_{11,0} = \{5, 2, -2, 1, 9\}$, $T_{11,1} = \{8, -3, -8, 3, 12\}$,

$2T_{11,2} = \{16, -16, -19, 13, 4\}$, $2T_{11,3} = \{16, -17, -16, 17, -12\}$,

$T_{11,4} = \{3, -10, -6, 7, -9\}$, $T_{11,5} = -T_{12,5}, T_{11,6} = -T_{12,6}$

$-T_{12,1} = \{2, 1, -2, -1, 10\}$, $-2T_{12,2} = \{20, 12, -5, 3, 33\}$,

$-2T_{12,3} = \{20, -7, -20, 7, 12\}$, $T_{12,4} = \{-3, -11, -9, 5, 6\}$,

$2T_{12,5} = \{0, 9, 0, -9, 12\}$, $2T_{12,6} = \{0, 0, -3, -3, 3\}$.

The numbers in braces denote coefficients Π_i in

$$\Pi = \frac{\sum_{i=0}^{3} \Pi_i \beta^{(3-i)}}{F_{II}(1 - \beta^2)^2} + \frac{\Pi_4}{4F_p}$$

That formula, for example, can be used to explicitly write coefficient $T_{11,0}$ as

$$T_{11,0} = \frac{5\beta^3 + 2\beta^2 - 2\beta + 1}{F_{II}(1 - \beta^2)^2} + \frac{9}{4F_p}$$

Vladimir Krichevsky received an M.S. and a Ph.D. in radiophysics from Leningrad University and Kharkov University, USSR, respectively. Before joining COMSAT in 1978, he was with the University of Illinois, and earlier the Leningrad Institute of Communication. He is currently a member of the technical staff in the Antenna Department of the Antennas and Propagation Laboratory at COMSAT Laboratories. He is a member of the IEEE.

Daniel F. DiFonzo received a B.E.E. from Villanova University in 1962 and an M.S. from California State University in 1972. He is presently Director of the Antennas and Propagation Laboratory at COMSAT Laboratories, responsible for directing and performing research and development related to propagation studies and communications satellite and earth station antenna systems. Specifically, he has performed extensive analytical and experimental studies of techniques for the control and measurement of microwave antenna polarization properties and the design of multiple-beam spacecraft antennas. He is a member of IEEE, APS, and MTT.

Solar absorptance degradation of the COMSTAR satellite centimeter-wave beacon thermal radiators

N. L. HYMAN

(Manuscript received December 11, 1980)

Abstract

The centimeter wave beacons on the COMSTAR satellites have heat-rejecting radiators of silver-under-quartz optical solar reflectors (OSRS). Constant internal power dissipation, well-defined solar exposure, and reliable temperature telemetry have permitted accurate derivation of the increase in their solar absorptance (α_s). Each of three satellites has provided more than 2 years of data [5,500 to 6,000 equivalent sun hours (ESH) in synchronous orbit]. Methods of data collection, reduction, and interpretation are presented. A dependence of α_s upon solar incidence angles greater than 15° off-normal was discovered. Rates of increase in α_s are constant after the first year, varying from 0.012 to 0.021 per year among radiators. Prediction error is estimated to be less than 5 percent. The larger α_s degradation rate of one set of radiators may be due to inadequate cleaning of surface contamination resulting from 2-year storage.

Introduction

The genesis of this paper can be found in the concluding sentence of Reference 1, which describes the COMSTAR beacon thermal and structural design: "Mirror degradation is . . . an area of prime concern,

159

and monitoring of mirror degradation will continue throughout the life of each beacon."

The OSR mirror of the beacon thermal radiators serves as the basis for many other satellite temperature control systems because of its low solar absorptance (α_s) and a relatively low rate of α_s increase. Some flight experiments for measuring α_s of thermal control coatings have indicated no change for the OSR during 1,580 ESH [2] and up to 2,800 ESH [3]. The sample coatings probably avoided surface contamination before and after launch, agreeing with laboratory α_s measurements of pristine OSR samples exposed to radiation and particulates. One flight experiment, however, revealed probable post-launch contamination with an initial OSR α_s significantly greater than laboratory measurement, followed by an appreciable increase during the first year [4]. Also, higher-than-predicted and increasing temperatures from satellites with OSR radiators have aroused strong suspicion of appreciable α_s increase initiated by contaminants or differential electrostatic arc discharge [5]–[7].

The beacon experiment investigates microwave propagation; original objectives did not include a study of the radiator's thermal coating. However, in one respect, the beacon can serve as a coatings experiment more practical and valuable than dedicated flight experiments. It more closely represents large OSR radiators which are not subject to the extreme control, care, and cleaning given to sample coatings. Temperature sensors within the beacon were provided for experiment performance evaluation. Their use for determining the increase of α_s with time was facilitated by their measurement accuracy, constant internal power dissipation, a superinsulated package, and well-defined solar flux incidence.

This paper describes the procedures for predicting α_s degradation from temperature telemetry data and presents the results as a 2-year α_s profile for the 28-GHz beacon radiators on COMSTAR D-1, D-2, and D-3. The phenomena which cause degradation will not be discussed, nor will procedures for applying the results to radiator design under different orbital environments. The greatest impediment to utilizing the results is not prediction inaccuracy, which is very low, but the large and not thoroughly understood differences in the degradation rate among radiators.

Beacon thermal characteristics

The beacon package as a means for OSR α_s measurement can be described as a radiator surface of OSRs attached to a baseplate, upon which are mounted components that produce uniformly distributed constant heat dissipation. The radiator surface views only the diurnal sun. Heat flow other than that through the radiator is negligible due to a superinsulation blanket covering all nonradiator surfaces and a low conductance mounting to the satellite mast.

Heat dissipation is 30 ± 3 W per package and is practically constant with time. Figure 1 shows the radiator surface normal 15° north of the equatorial plane, an attitude which excludes radiative input from satellite surfaces and results in a yearly exposure of 2,580 ESH. The exposed surface is a 26×44-cm rectangle, 98 percent covered by 2.54-cm-square OSRs bonded to the aluminum honeycomb substrate with DC93-500 adhesive. The OSR is 0.02-cm-thick Corning 7940 fused silica with a deposited silver backing protected by a dielectric overcoat.

Absorptance change calculation

Within the nonisothermal beacon package, the temperature of a telemetry sensor does not necessarily follow the average temperature of either the radiator or the heat-generating components. In the following equation describing heat balance for an entire package, temperatures are effective averages:

$$Q_d + Q(t) + A\alpha_s F(t) - A\epsilon\sigma T_r^4 = MC\frac{dT_p}{dt} \qquad (1)$$

where Q_d = total internally dissipated power, constant with time
   $Q(t)$ = net heat input from external sources other than via the radiator, a function of time
   A, ϵ = radiator area and emittance ($A \approx 1,120$ cm^2, $\epsilon = 0.78$, assumed constant)
   $F(t)$ = incident solar flux, a function of time
   MC = total package thermal capacitance ($MC \approx 4045$ W-s/ °C for 28-GHz package)
   T_r, T_p = effective average temperatures for the radiator surface and total package.
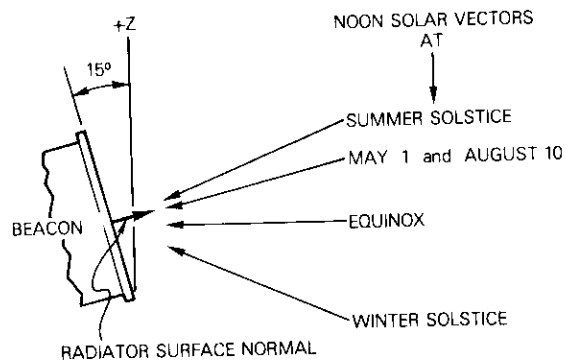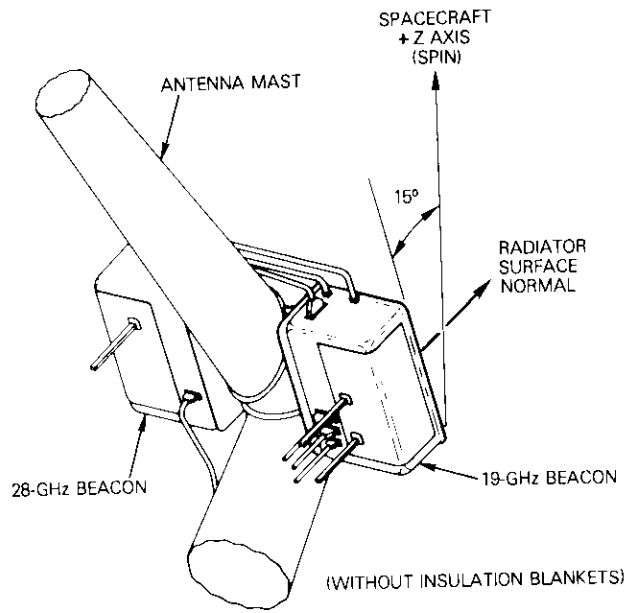
Figure 1. *Beacon-on-COMSTAR Geometry*

Simplification is realized by considering only temperature extremes. Near maximum temperature, telemetry data reveal a very slow change, approximately 0.1°C over 1 hour. Thus, it can be assumed that the temperature extremes $T_{r\text{max}}$ and $T_{p\text{max}}$ occur simultaneously with the sensor temperature extreme T_{max}. When $dT_p/dt = 0$, $T_{r\text{max}}$ and T_{max} differ by an amount, ΔT_x, which is assumed to be the same throughout the year, and for all values of α_s. Equation (1) can therefore be put in the form

$$Q_d + Q(t) + A\alpha_s F(t) - A\epsilon\sigma\left(T_{\text{max}} + \Delta T_x\right)^4 = 0 \quad . \tag{2}$$

The relationship between changes in T_{max} and α_s can be obtained by differentiating equation (2):

$$dQ(t) + A\alpha_s dF(t) + AF(t)d\alpha_s - 4A\epsilon\sigma\left(T_{\text{max}} + \Delta T_x\right)^3 dT_{\text{max}} = 0 \quad . \tag{3}$$

Finding a simple relationship between $d\alpha_s$ and dT_{max} is complicated by unknown ΔT_x, and $Q(t)$ and $F(t)$ which vary throughout the year at times of T_{max}. The incident solar flux can be accurately determined as a function of time; the net heat flow through insulation blanket and mast attachment hardware, although relatively small, presents a difficult challenge.

Because of the difficulty in estimating $dQ(t)$ and ΔT_x in equation (3), a 14-node analytical thermal model, which accounts for all components of $Q(t)$ and simulates a ΔT_x effect with a resistance between the sensor and radiator, was used for $\Delta\alpha_s$ predictions. This model was developed after flight temperatures became available, making it possible to refine properties such as thermal mass and sensor-to-radiator resistance, and to include second-order effects such as solar reflection from the insulation hump covering the mast.

Many computer runs using this model to predict daily temperature profiles throughout the year with various α_s were graphically compiled into "working curves" such as those of Figure 2, which are applicable to the D-2 and D-3 28-GHz packages, with $Q_d = 32$ W. Another set of similar curves with $Q_d = 29$ W was used for the D-1 28-GHz package.* The bottom curve is based on a constant $\alpha_s = 0.13$, an

---

*This procedure was initially applied only to the 28-GHz package because, soon after the D-1 launch, power in the 19-GHz package dropped due to a current supply malfunction; treatment of temperature data from 19-GHz packages is described later.
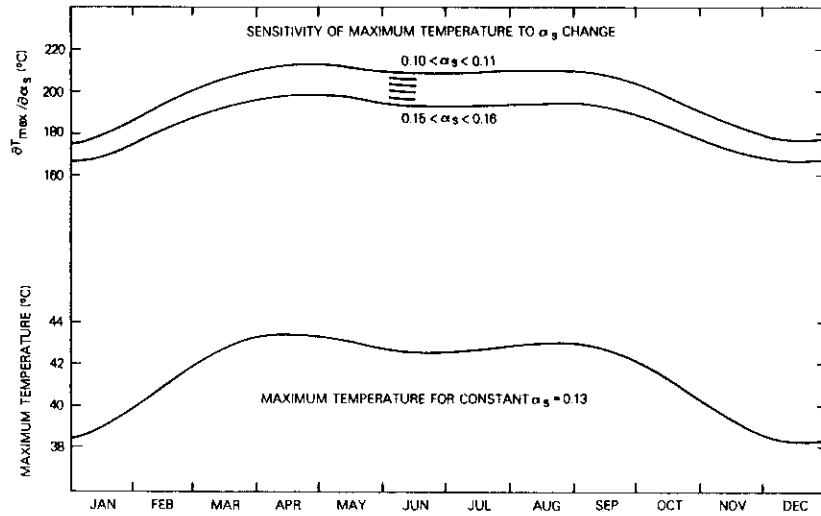
Figure 2. *Predicted Maximum Diurnal Temperature Characteristics of 28-GHz Beacon on COMSTAR D-2 and D-3: 32 W Dissipation*

approximate median; those at the top present the sensitivity of T_{max} to α_S change, $\partial T/\partial \alpha_S$, which varies with day of year and α_S magnitude. A predicted α_S for a particular day is thus

$$\alpha_S = 0.13 + \frac{T_{max} - T_{pr}}{\partial T/\partial \alpha} \qquad (4)$$

where T_{max} = maximum telemetry sensor temperature
   T_{pr} = predicted maximum with $\alpha_S = 0.13$
   $\partial T/\partial \alpha_S$ = a value from the curves based upon the previously
   derived α_S.

The random error introduced by this graphical data reduction process is acceptably small, estimated to be $\pm 0.02°$ for temperature and 2 percent for $\partial T/\partial \alpha_S$*. This is equivalent to an uncertainty of approximately 1 percent in $\Delta \alpha_S$/yr calculations.

---

*For an α_{S_1} different from 0.13, the correct $\partial T/\partial \alpha_S$ is an effective average corresponding to an α_S between α_{S_1} and 0.13. The greater the difference between α_{S_1} and 0.13, the greater the possible error in estimating $\partial T/\partial \alpha_S$ from the series of curves.

A 26-month history of maximum temperatures of the D-3 28-GHz package is shown in Figure 3, along with the prediction for $\alpha_S = 0.13$. The three α_S *vs* time curves of Figure 4 were derived from maximum temperature telemetry, working curves such as those in Figure 2, and equation (4).
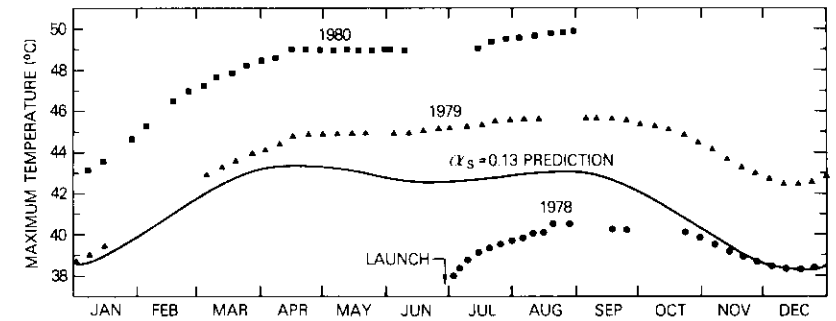
Figure 3. *28-GHz Beacon on COMSTAR D-3: History of Telemetered Maximum Daily Temperature and Predicted Maximum Temperature for $\alpha_S = 0.13$*

Constant power dissipation

Since beacon maximum temperature is a function not only of α_S but of internal power dissipation, an accurate measure of Q_d, unavailable from telemetry, is essential for precise α_S determination. The 29 and 32 W used for the working curves were estimated from telemetered minimum temperatures. Some uncertainty in Q_d magnitude is acceptable for predicting change in α_S; differences in Q_d would merely shift the α_S *vs* time curves of Figure 4 vertically without noticeably affecting shape or slope.

A constant Q_d can be confirmed by examining the history of telemetered minimum temperature. Applying equation (2) to a minimum when $F(t) = 0$ yields

$$Q_d = A\epsilon\sigma\left(T_{min} + \Delta T_n\right)^4 - Q(t) \qquad (5)$$

where ΔT_n is the constant temperature difference between T_{min} and
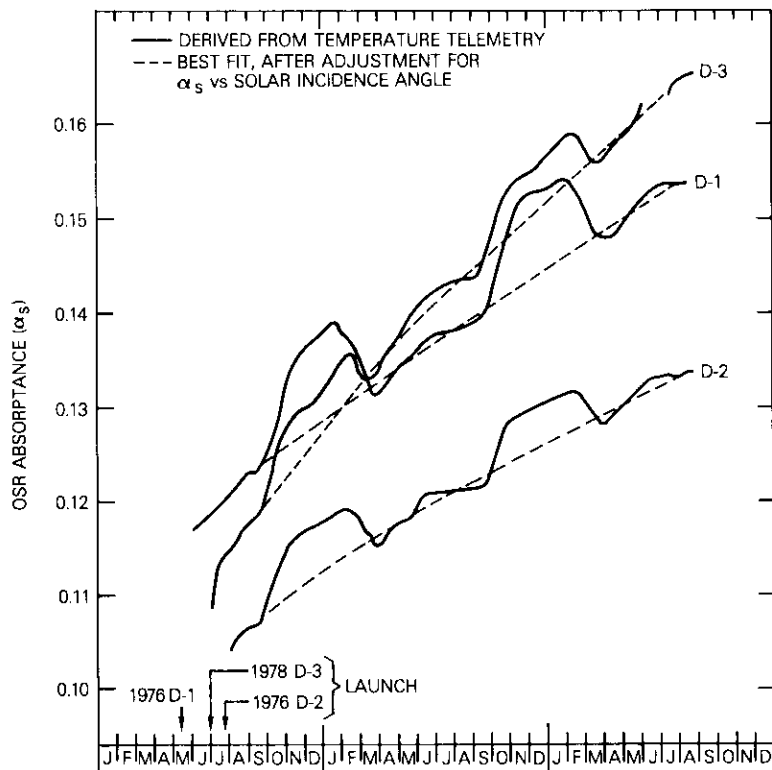
Figure 4. *28-GHz Beacon OSR Absorptance* vs *Time on COMSTAR D-1, D-2, and D-3*

T_{rmin}. Since temperature does not decay to a steady-state minimum, independent of the temperature level at which cooldown began, T_{min} becomes a weak function of T_{max}, or α_S.

Because $Q(t)$ is a complex function of sun attitude, difficult to predict, the most practical use of equation (5) is with a time displacement of exactly 1 year and equal $Q(t)$. Thus, over a one-year interval, assuming that $\Delta T_n = 0$ and neglecting the effect of variable α_S,

$$\Delta Q_d = A\epsilon\sigma\Delta T_{min}^4 \quad . \tag{6}$$

Minimum temperature history of the D-1 28-GHz package is plotted in Figure 5. The year-to-year variation is remarkably low; all data,

---
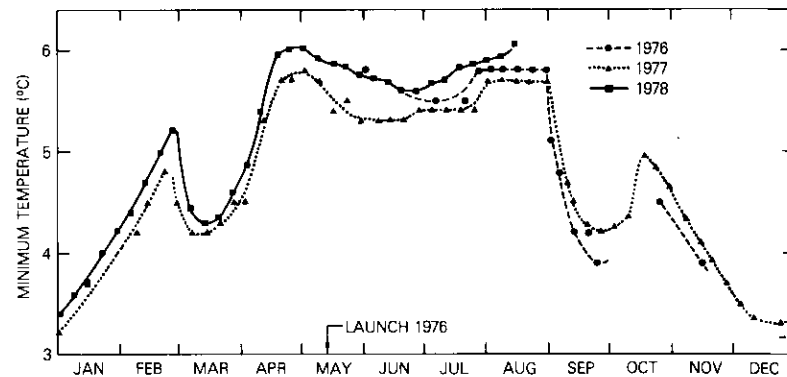
Figure 5. *COMSTAR D-1 28-GHz Beacon Minimum Temperature History*

including that from D-2 and D-3, are contained in a $\pm 0.2°C$ band (most within $\pm 0.1°C$). This variation cannot be fully explained by effects of α_S increase (calculated with $\partial T_{min}/\partial\alpha_S$ obtained from the thermal model and $\Delta\alpha_S$ from Figure 4); it must also be attributed to Q_d variation. To determine the effect of ΔQ_d on $\Delta\alpha_S$, it is assumed that T_{min} varies only because of ΔQ_d; the apparent change in α_S from a change in Q_d is expressed as

$$\Delta\alpha_S = \frac{\partial T_{max}/\partial Q_d}{\partial T_{max}/\partial\alpha_S \cdot \partial T_{min}/\partial Q_d}\Delta T_{min} \quad . \tag{7}$$

The partial derivatives are estimated from thermal model results and yield $\Delta\alpha_S = (0.004/°C)\Delta T_{min}$.

A change of $0.2°C$ in T_{min} (corresponding to a ΔQ_d of 0.085W, or 0.3 percent) means an apparent α_S change of 0.008. Thus, if Q_d is assumed constant, a maximum uncertainty in $\Delta\alpha_S$ per year ranging from 3.8 to 6.4 percent is introduced. This is acceptably low for this study; therefore, a constant Q_d is assumed.

Effect of solar incidence angle

The limited data of Reference 1, from launch to late October 1976, indicated α_S increasing at a rate of 40 percent per year. The solid curves of Figure 4 show that this alarming conclusion resulted from an observation time span which covered the rising portion of an unex-

pected cyclic phenomenon. All curves show an abrupt linear rise in α_s beginning at autumnal equinox and an equally sharp decay ending at vernal equinox. In a 2- to 3-month intermediate time, α_s increases at a fairly constant rate equal to the rate during the half-year from vernal to autumnal equinox. Since α_s degradation is a monotonically increasing phenomenon [8], these anomalous steep cyclic decreases, and corresponding increases, deserve explanation.

The wide seasonal variation in solar incidence angle near local noon suggests the influence of the phenomenon of increasing α_s with decreasing incidence angle, α_s approaching unity at grazing angles [9]. Integrating sphere spectroreflectometer measurements were made on an OSR sample at 20° (assumed the same as normal) and 40° (the maximum near local noon). The measured α_s increase of 0.005 (0.061 to 0.066) explains most of the increase observed on the D-2 and D-3 28-GHz radiators and about half that on the D-1.

An estimate of α_s variation with effective incidence angle was obtained by first assuming a linear α_s vs time relation for normal incidence from autumnal to vernal equinox, following the curves' general slope after excluding sharp increases and decreases. The difference in α_s between this line and the original, higher profile was assumed to be the increase due to angle-of-incidence effects. A correlation of this $\Delta\alpha_s$ with the seasonal incidence angle at local noon is not equivalent to a controlled laboratory measurement with fixed vectors, because of the superimposed diurnally changing solar vector. Errors are not expected to be appreciable, however, since incidence angle changes are gradual in the vicinity of local noon (e.g., during the 3 hours centered at noon, winter solstice, the change is only 6°).

Figure 6 shows α_s difference as a function of the angle between the noon solar and surface normal vectors. The D-2 and D-3 profiles are almost congruent and are close in slope to the spectroreflectometer measurements. No explanation of the larger slope of D-1 can be offered. Based on the realistic appearance of the data in Figure 6, it is reasonable to conclude that the dashed lines between September and March in Figure 4 represent α_s vs time "corrected" to normal solar incidence.

Yearly fractional change in α_s

Equation (2) can be rewritten disregarding the difference between the sensor and radiator average temperature:
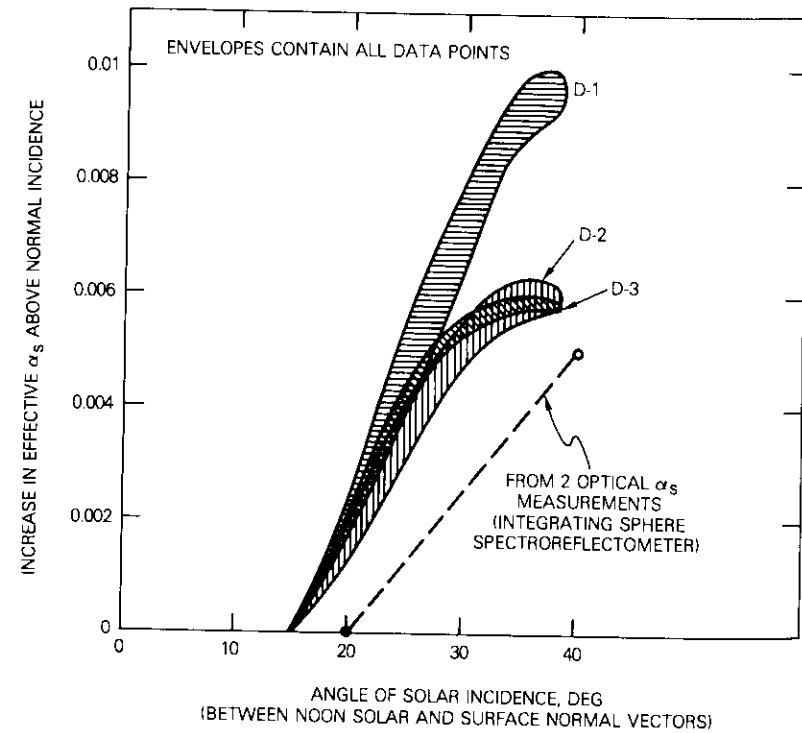
Figure 6. *Effective Absorptance as a Function of Noon Angle of Solar Incidence on 28-GHz Beacon Radiator*

$$\alpha_s = \frac{A\epsilon\sigma T_{max}^4 - Q_n}{AF(t)} \qquad (8)$$

where Q_n is a net heat flow rate, a sum of Q_d and $Q(t)$.

Rewriting equation (5) and again neglecting the temperature difference between the sensor and radiator at the time of minimum temperature yields

$$Q_n = A\epsilon\sigma T_{min}^4 \qquad (9)$$

If it is assumed that Q_n at minimum temperature is equal to Q_n at maximum temperature (since almost all of Q_n is the constant dissipation

Q_d), equations (8) and (9) can be combined as follows:

$$\alpha_S = \frac{\epsilon\sigma}{F(t)}(T_{max}^4 - T_{min}^4) \quad . \qquad (10)$$

If the application of this equation is restricted to two points in time exactly 1 year apart, when the solar vectors $F(t)$ are equal, differentiating yields

$$\frac{\Delta\alpha_S}{\alpha_{S_1}} = \frac{T_{max_2}^4 - T_{max_1}^4}{T_{max_1}^4 - T_{min}^4} \qquad (11)$$

where T_{max_1} and T_{max_2} are maximum temperatures separated by 1 year, and T_{min} represents the approximately equal minimums at both times.

Equation (11) was applied to all the temperature data for the three 28-GHz packages. The resultant curves of Figure 7 agree with $\Delta\alpha_S/\alpha_S$ extracted from Figure 4 to within 5 percent. Although these 1-year-interval $\Delta\alpha_S/\alpha_S$ results are not as revealing or useful as α_S vs time curves, equation (11) was used to efficiently reduce 19-GHz data; the results are included in Figure 7.* The D-1 unit was excluded because of a power loss anomaly.

Figure 7 confirms that α_S degradation characteristics of adjacent 19- and 28-GHz radiators are quite similar; the $\Delta\alpha_S/\alpha_S$ of the final, flat portions of the corresponding curves differ by less than 8 percent.

Temperature telemetry

The two beacon telemetry temperature sensors used for this study, one in each of the 19- and 28-GHz packages, were thermistors (YSI 44006) bonded to aluminum tabs secured under equipment mounting screws. The temperature-voltage relation is fairly linear; in the two temperature ranges of most interest, 0–10°C and 40°C–50°C, the octal count resolution (corresponding to 0.02-V difference in output voltage) is 0.35°C and 0.41°C, respectively.

Resolution was improved with a graphics computer program which displays a channel of stored telemetry data as a function of time on

---

*A gradual decrease of D-2 dissipation with time was revealed from T_{min} data, implying an addition of 0.015–0.018 to the plotted $\Delta\alpha_S/\alpha_S$ values.
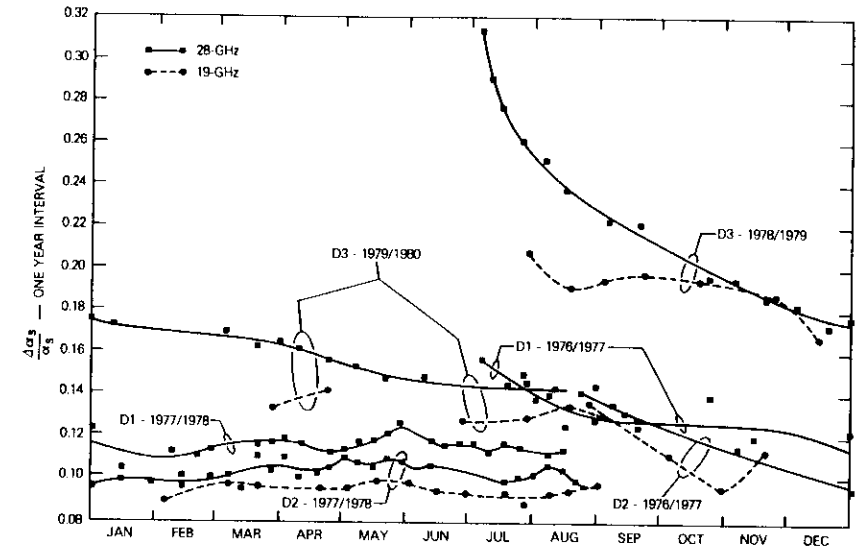
Figure 7. *Fractional Change in α_S Over 1-Year Intervals*

any assigned set of scales, providing detailed close-ups of maximum and minimum temperatures. When a sensor jumped from one count to the next in a certain time interval (data points were never more than 10 minutes apart), it was assumed that at some time in that interval the actual temperature was at the midpoint of the counts. The accurate, high-resolution, temperature-time "points" (horizontal lines of time interval width) thus generated were then fitted with a smooth curve as shown in Figure 8. Temperature extremes read from such curves are estimated to be accurate within ±0.02°C, accounting for errors in curve formulation as well as reading resolution. This is equivalent to less than ±0.8 percent in $\Delta\alpha_S$/year calculations.

Measurement and computation accuracy

Since temperature changes are sufficient data from which to derive changes in α_S, the telemetry circuit characteristics related to accuracy are stability (repeatability) during the 2-year data collection period and changes in absolute error with temperature change. The thermistor and linearizing resistor of the temperature sensor circuit should not encounter characteristics changes with time in their relatively benign environment. Telemetry calibration reference voltages that ensure
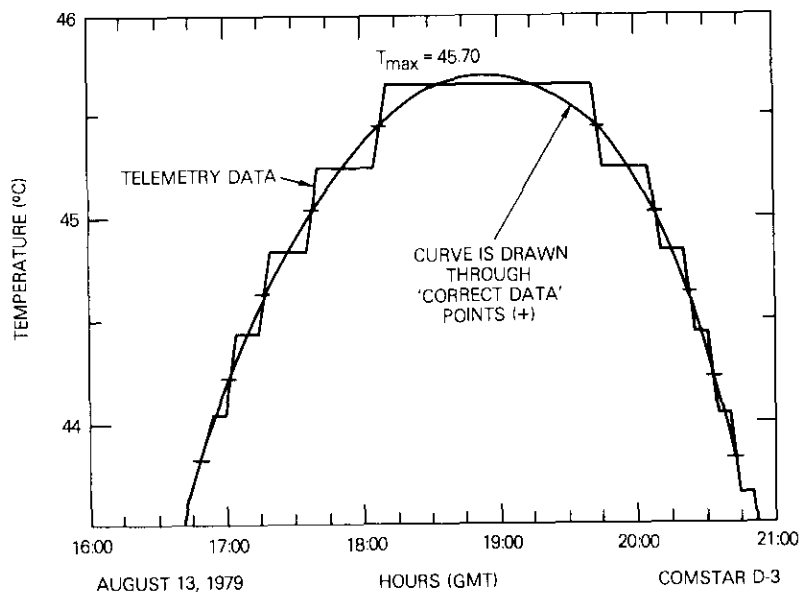
Figure 8. *Example of Temperature Telemetry Display and Graphical Procedure for Obtaining Maximum Temperature*

accurate telemetry calibration on the ground remained unchanged throughout the data collection periods.

Thermistor circuit output over a wide temperature range was compared with adjacent test thermocouple sensors during beacon acceptance testing. Of particular interest was the temperature difference over the range of maximum temperatures, 40°C to 50°C. No change was noticed for D-1 and D-2; for D-3, the 1°C change was considered within the thermocouple measurement error and recording resolution. This source of error was assumed to be negligible.

A potentially serious source of error is the deficiency of the analytical thermal model; that is, the inherent errors in working curves such as those in Figure 2. Simulation by thermal model is admittedly imperfect, but errors which could affect the prediction of absolute α_s become second-order effects for $\Delta\alpha_s$ prediction. Comparing $\Delta\alpha_s$ vs time based on thermal model predictions with the $\Delta\alpha_s/\alpha_s$ per year derived simply from temperature extremes and equation (11) yields agreement within

5 percent. Thus, the rates of change of Figure 4 are probably correct within a total error of 5 percent.

A closer examination of the curves in Figure 4 confirms this conclusion. The solid lines include all data points; the dashed lines are linearized mean values and account for incidence-angle effects. The difference between the solid and dashed lines when there is no incidence angle correction is less than ± 0.0015 and always of the same shape from year to year and from satellite to satellite. This suggests slight inexactness in modeling, most likely seasonally changing heat input parameters, but is of no concern over the long term because of its yearly cycle repeatability. Moreover, the designer wanting to use these study results will not be nearly as concerned with such small prediction error as with interpreting the $\Delta\alpha_s$ differences among radiators, an order of magnitude larger.

$\Delta\alpha_s$ differences among radiators

The curves of Figure 4 are transposed to an ESH scale and displayed together in Figure 9. Differences in vertical displacement between curves are of no special concern, since a degree of error* in determining absolute values of α_s can be tolerated without affecting the most important characteristic, the time rate of change of α_s.

The shapes of all the curves are similar in that they have a higher initial slope until approximately the first summer solstice (2,000 to 3,000 ESH) when the slope abruptly decreases and remains constant until the end (5,500 to 6,000 ESH).† The D-3 slopes are, however, disconcertingly higher than the other two; the initial (0.031/yr) and final (0.021/yr) slopes are some 70 and 35 percent greater, respectively, than the corresponding D-1 slopes.

This study is intended to aid predictions of end-of-life radiator performance. If the results are limited only to D-1 and D-2, a reasonable design guide for a similarly exposed radiator would be the more conservative D-1 curve. With much greater D-3 degradation, however, justification is desired before conservatism is invoked in favor of its use.

---

*Internal dissipation inputs to the thermal model are uncertain by ± 1 W or ± 0.01 in α_s.

†The rapid rise in D-3 α_s during the first month may have occurred on D-1 and D-2, but detailed telemetry close to launch was not preserved.
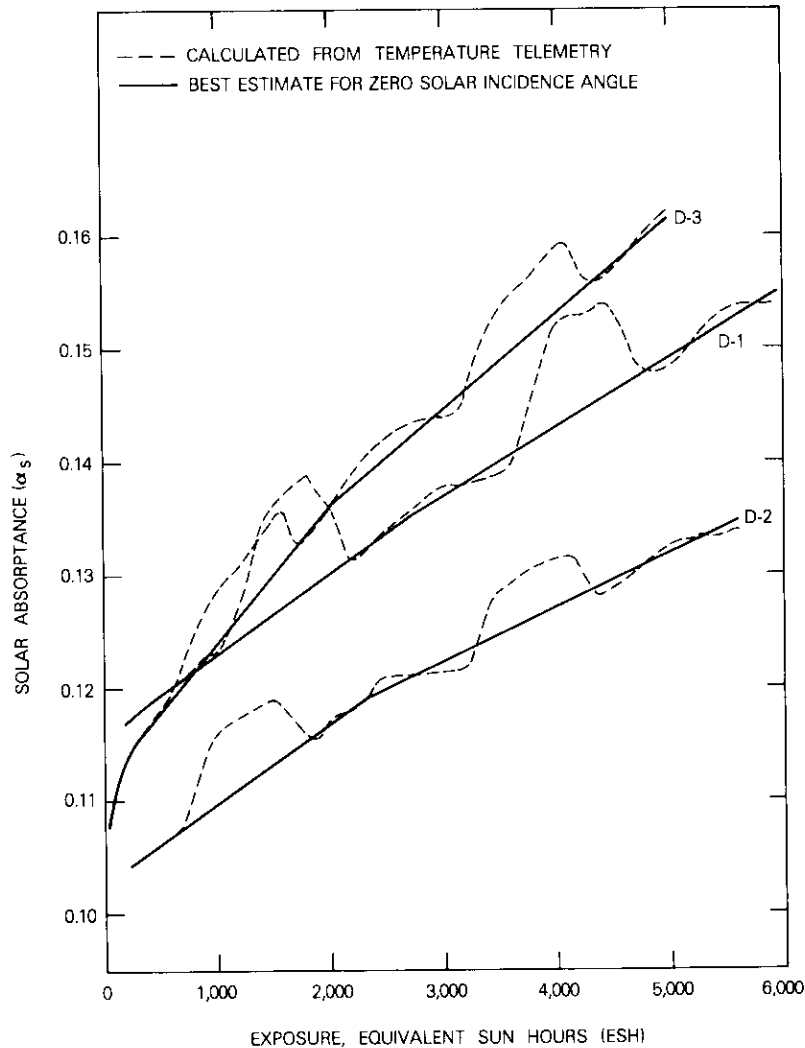
Figure 9. *Solar Absorptance Histories of 28-GHz Beacon Radiators on COMSTAR D-1, D-2, and D-3*

Storage, cleaning, and contamination

A speculative explanation for the higher D-3 degradation rate is based on one distinct difference: approximately 2 years longer storage time. Reflectivity measurements of witness plates placed near the D-3 and D-4 beacons during storage revealed definite deposits (especially with the D-4, which remained in storage more than 4 years) that would be ripe for darkening upon ultraviolet exposure. Analysis of these deposits was not justified since their location was not precisely representative of the beacon radiator. Because such deposits were not anticipated nor possible effects understood, only standard cleaning procedures were used and cleaning effectiveness was not measured. Inadequate removal of such contaminants was a definite possibility, and could explain higher D-3 degradation.

Surface contamination is evidenced by high α_s just after launch. Based on α_s laboratory measurements of 0.061, clean-radiator α_s (including between-mirror spaces) is expected to be approximately 0.08; Figure 9 indicates initial α_s between 0.100 and 0.115. These higher values could be due to imperfect cleaning and/or to contaminant deposit immediately following launch. The relatively cold radiators of a beacon before turn-on could be a prime condensing surface for outgassed contaminants.

The COMSTAR D-4, launched in February 1981, may provide useful, and perhaps conclusive, data on solar absorptance. The 19-GHz radiator was cleaned "as usual" while the 28-GHz radiator remained uncleaned. (Planned beacon operation of only 6 months will limit the α_s increase of contaminated mirrors to nondangerous levels.) Comparing the α_s histories from these extreme cases should reveal much about the relative contributions of storage and post-launch contaminants.

The lack of a definitive explanation of the different α_s degradation rates inhibits confident use of the study results. However, it is significant that vastly different degradation rates did occur with identical radiators on identical satellites. Since the fabrication, storage, cleaning, and in-orbit contamination exposure of these radiators were similar to that of many other satellite radiators, presumably such variable degradation rates are not unique.

Conclusions

Solar absorptance degradation behavior of the beacon thermal radiators of the COMSTAR D-1, D-2, and D-3 satellites has been accurately derived from temperature telemetry data. After a rapid rise during the first year, rates of absorptance increase during the second year were constant, varying from 0.012 to 0.021 per year. The large difference among radiators may be due to uneven removal of storage deposits and variable in-orbit contamination. Degradation rate prediction accuracy, estimated at 5 percent, is negligible. A dependency of absorptance upon angle of solar incidence was deduced from flight data and supported by laboratory measurements. Remaining uncertainties should be lessened after a planned half-year of $\Delta\alpha_s$ predictions from D-4 telemetry data following prelaunch cleaning of only one of the beacon radiators.

References

[1] N. Hyman et al., "Thermal and Structural Design Aspects of the Centimeter Wave Beacon," *COMSAT Technical Review*, Vol. 7, No. 1, Spring 1977, pp. 171–196.

[2] J. P. Millard and B. D. Pearson, Jr., "Optical Stability of Coatings Exposed to Four Years Space Environment on OSO III," *AIAA Progress in Astronautics and Aeronautics: Thermophysics and Spacecraft Thermal Control*, edited by R. G. Hering, Vol. 35, 1973, pp. 249–262.

[3] D. F. Hall and A. A. Fote, "α_s/e Measurements of Thermal Control Coatings on the P78-2 (SCATHA) Spacecraft," AIAA-80-1530, AIAA 15th Thermophysics Conference, July 1980.

[4] R. A. Winn, "ML-101 Thermal Control Coatings: Five Year Space Exposure," AFML-TR-78-99, July 1978.

[5] J. P. Bouchez and J. Gulpen, "The European Geostationary Communications Satellite OTS: Two Years of Thermal Control Experience in Orbit," AIAA-80-1500, AIAA 15th Thermophysics Conference, July 1980.

[6] D. G. T. Curran and J. M. Millard, "Results of Contamination/Degradation Measurements on Thermal Control Surfaces of an Operational Satellite," AIAA-77-740, AIAA 12th Thermophysics Conference, June 1977.

[7] R. C. Adamo and J. E. Nanevicz, "Spacecraft-Charging Studies of Voltage Breakdown Processes on Spacecraft Thermal Control Mirrors," *Progress in Astronautics and Aeronautics: Spacecraft Charging by Magnetospheric Plasmas*, edited by A. Rosen, Vol. 47, 1975, pp. 225–235.

[8] J. B. Schutt and C. H. Duncan, "A Biased Model for Calculating the Evolution in Solar Absorptance," Institute of Environmental Sciences 19th Annual Technical Meeting, April 1973, pp. 5–9.

[9] J. W. Stultz, "Solar Absorptance of Second Surface Mirrors for High Angles of Incidence," AIAA Paper 74-670, AIAA/ASME 1974 Thermophysics and Heat Transfer Conference, Boston, Massachusetts, July 1974.

Nelson Hyman received a B.M.E. from Georgia Institute of Technology in 1958 and an M.S.M.E. from the University of Maryland in 1959. Prior to joining COMSAT Laboratories in 1969, he engaged in spacecraft thermal design with NASA/GODDARD Space Flight Center and Fairchild Industries. As a member of the technical staff in the Thermal Control and Environmental Testing Department of the Spacecraft Laboratory, he has participated in a variety of thermal analysis, evaluation, and development tasks, from satellites and their subsystems to earth terminal equipment. He was the principal contributor to the thermal design of the Centimeter Wave Beacon.
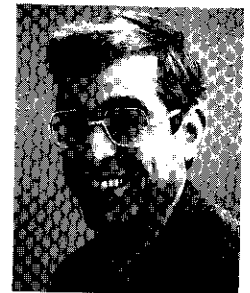
ese lugar geométrico reduciendo al mínimo el error de fase con respecto a la dirección del haz. Las soluciones se pueden representar en forma cerrada respecto de los parámetros geométricos de la antena.

La solución de primer orden produce una línea recta óptima a lo largo de la cual deberán colocarse los alimentadores; la solución de segundo orden produce una curva de puntos que representa una hipérbola en todos los casos considerados. Los análisis de computadora de varias configuraciones específicas de antena Cassegrain de alimentador descentrado confirman que las soluciones descritas permiten que el rendimiento del haz explorado sea superior al que se obtiene, por ejemplo, con el método más convencional de desplazar transversalmente el alimentador en posición normal al eje de un cono que subtiende el subreflector.

Degradación producida por la absorsancia solar en los radiadores de baliza de ondas centimetricas de los satélites COMSTAR

N. L. HYMAN

Abstracto

Las balizas de ondas centimétricas de los satélites COMSTAR tienen radiadores disipadores de calor con reflectores ópticos solares (OSR) de plata cubierta de cuarzo. La constante disipación interna de la potencia, una exposición solar bien definida y una telemetría fiable sobre temperaturas han permitido calcular con exactitud el aumento en la absorsancia solar de esas balizas (α_s). Tres de estos satélites han suministrado el equivalente a más de dos años de datos (igual a 5.500 a 6.000 horas de Sol en órbita síncrona). Se presentan métodos de compilación, reducción e interpretación de datos. Se descubrió una dependencia de la α_s sobre los ángulos de incidencia solar mayores del 15° fuera de lo normal. Los índices de aumento en α_s son constantes después del primer año, con variaciones entre 0,012 y 0,021 por año de un radiador a otro. El error de predicción se calcula que es menor del 5 por ciento. La mayor tasa de degradación por α_s observada en un juego de radiadores puede atribuirse a una limpieza inadecuada de la superficie contaminada como resultado de dos años de almacenamiento.

Author Index, CTR 1980

Code numbers listed below are to be used for ordering reprints from Lab Records, COMSAT Laboratories. 22300 COMSAT Drive, Clarksburg. Maryland 20734.

AUTRY, R. G., see Kreutel, R. W. [CTR80/198].

CALVIT, T. O., "Ship-to-Shore Tests of a MARISAT 56-kbit/s Data Service," Fall, pp. 417–426 [CTR80/201].

COOK, W., Kaul, A., Hodge, G., and Marchese, J., "An International Experiment in High-Speed Computer Networking via Satellite," Spring, pp. 27–90 [CTR80/189].

DORIAN, C., Potts, J. B., Reinhart, E., and Weiss, H., "The 1979 World Administrative Radio Conference and Satellite Communications," Spring, pp. 1–26 [CTR80/188].

DUNLOP, J. D., and Stockel, J. F., "Nickel-Hydrogen Battery Technology—Development and Status," Fall, pp. 281–298 [CTR80/196].

GREENE, K. H., see Kreutel, R. W. [CTR80/198].

GREENE, K., Sones, W., Grossman, M., Jones, M., and Jacobus, N., "Automatic Seismic Observatory Communications System," Spring, pp. 179–222 [CTR80/193].

GROSSMAN, M., see Greene, K. [CTR80/193].

HORNA, O. A., "Fast Algorithms for the Computation of Binary Logarithms," Spring, pp. 91–102 [CTR80/190].

HUNG, H.-L., and Hyman, N. L., "Thermoelectrically Cooled MESFET Low-Noise Amplifier for Earth Stations," Fall, pp. 299–320 [CTR80/197].

HYMAN, N. L., see Hung, H.-L. [CTR80/197].

JACOBUS, N., see Greene, K. [CTR80/193].

JONES, M., see Greene, K. [CTR80/193].

KAUL, A., see Cook, W. [CTR80/189].

KENNEDY, D. J., "A Model for Calculation of Rain-Induced Cross-Polarization Discrimination at 6/4 GHz," Spring, pp. 223–232 [CTR80/194].

KREUTEL, R. W., Williams, A. E., Greene, K. H., Lee, Y. S., and Autry, R. G., "Optical Transmission Technology in Satellite Communications," Fall, pp. 321–368 [CTR80/198].

LEE, L. N., and Weng, M. I., "2-Bit Soft-Decision Weighted Erasure Decoding for Binary Block Codes," Fall, pp. 397–416 [CTR80/200].

LEE, Y. S., see Kreutel, R. W. [CTR80/198].

MORGAN, W. L., "Geosynchronous Satellite Log for 1980," Spring, pp. 233–262 [CTR80/195].

Comsat Authors' Presentations and Publications—1980

The following is a cross-referenced index of technical publications by COMSAT authors outside of *COMSAT Technical Review*. The code number at the end of an entry is the reprint code number by which copies may be ordered from Lab Records at COMSAT Laboratories, 22300 at COMSAT Drive, Clarksburg, Maryland 20734.

ALLISON, J. F., see Meulenberg, A. (80CLR01), (80CLR52).

ARNDT, R. A., see Meulenberg, A. (80CLR01), (80CLR52).

ARNSTEIN, D. S., "A New Technique for Detectability Analysis of PN Spread-Spectrum Multiple Access Systems with a Nonlinearity," Int. Conf. on Comm., June 80, *CONF. RECORD*, Vol. 3, pp. 62.1.1–62.1.5 (80CLR17).

ATIA, A. E., see Bonetti, R. (80CLR28).

ATOHOUN, I., see Riginos, V. (80CLR35), (80CLR47).

BAKER, W. E., "The Effects of Radiation on the Characteristics of Power MOSFET's," POWERCON 7 Seventh National Solid-State Power Conv. Conf., March 80, *PROC.*, pp. D3-1–D3-6 (80CLR54).

BARGELLINI, P. L., "Satellite Communications Systems and Their Integration in Terrestrial Networks," 27th Congresso Scientifico Internazionale per L'Elettronica—Sistemi Elettronici per le Telemisure e il Telerilevamento, March 80, *PROC.*, pp. 406–413 (80CLR34).

BARRETT, M. F., see Hsing, J. C. (80CLR06).

BILLERBECK, W. J., "Statistical Analysis of Ni-Cd Battery Degradation and Applications to New Spacecraft Designs," 15th Intersociety Energy Conv. Engineering Conf., Aug. 80, *PROC.*, pp. 110–118 (80CLR43).

BONETTI, R., & Atia, A. E., "Resonant Frequency of Dielectric Resonators in Inhomogeneous Media," IEEE MTT-S Int. Microwave Symposium, May 80, *DIGEST*, pp. 218–219 (80CLR28).

BRISKMAN, R. D., "Domestic Communications Satellites: Systems Considerations for Rural Areas," IEEE MEXICON-80 Conf., Oct. 80 *CONF. RECORD*, Vol. II, pp. 1–9 (80CLR57).

CALVIT, T. O. & Heitman, L. B.,* "High-Speed Satellite Data Transmission of Maritime Seismic Data, "AIAA 8th Comm. Satellite Systems Conf., Apr. 80, A COLLECTION OF TECH. PAPERS, pp. 714–722, AIAA Paper 80-0480 (80CLR25).

CARPENTER, E., "A Dual-Band Corrugated Feed Horn," IEEE Int. Symp. on Antennas and Propagation, June 80, *DIGEST*, Vol. 1, pp. 213–216 (80CLR18).

CHARTOFF, M. R., see Zaghloul, A. I. (80CLR11).

*Non-COMSAT Author.

*Non-COMSAT Author.
†INTELSAT Author.

*Non-COMSAT Author.

*Non-COMSAT Author.

SORBELLO, R. M., "Multibeam Antennas: A Key Element in High Capacity Geostationary Platforms," NTC '80 IEEE National Telecomm. Conf., Nov.-Dec. 80, *CONF. RECORD*, Vol. 3, pp. 75.3.1–75.3.5 (80CLR51).

SORBELLO, R. M., Karmel, P. R.* & Gruner, R. W., "Feed Array and Beam Forming Network Design for a Reconfigurable Satellite Antenna," IEEE Int. Symposium on Antennas and Propagation, June 80, *DIGEST*, Vol. 1, pp. 78–81 (80CLR10).

STOCKEL, J. F., see Dunlop, J. D. (80CLR42).

STOCKEL, J. F., Dunlop, J. D. & Betz, F. E.,* "NTS-2 Nickel-Hydrogen Battery Performance," *J. OF SPACECRAFT AND ROCKETS*, Jan.-Feb. 80, pp. 31–34 AIAA Paper 78-563R (80CLR04).

STRAUSS, R. & Owens, J. R.,† "Past and Present INTELSAT TWTA Life Performance," AIAA 8th Comm. Satellite Systems Conf., Apr. 80, *A COLLECTION OF TECH. PAPERS*, pp. 98–106, AIAA Paper 80-0486 (80CLR22).

UZUNOGLU, V., "Synchronization and Synchronous Oscillators," INFO II, 2nd Int. Conf. on Inf. Sciences and Systems, July 79, *ADVANCES IN COMM.*, Vol. 1, pp. 437–448 (80CLR48).

WELTI, G. R., "Application of Intersatellite Links to Collocated Telecommunications Satellites," ITC/USA/'80 Int. Telemetering Conf., Oct. 80, *PROC.*, Vol. XVI, pp. 199–208 (80CLR55).

WELTI, G. R., "Bandwidth-Efficient Modulation for Multichannel Telephone Transmission via Satellite," NATO Advanced Study Institute on New Concepts in Multi-user Communication, Norwich, U.K., Aug. 80 (80CLR60).

WELTI, G. R., Sandrin, W. A. & Neyer, R.,* "Application of Predistortion Linearization to Satellite Transponder," Int. Conf. on Comm., June 80, *CONF. RECORD*, Vol. 2, pp. 33.5.1–33.5.2 (80CLR16).

ZAGHLOUL, A. I., see MacPhie, R. H.* (80CLR31).

ZAGHLOUL, A. I. & Chartoff, M. R., "Correlation Matrix Solution to Mutual Coupling Between Rectangular Apertures," IEEE Int. Symposium on Antennas and Propagation, June 80, *DIGEST*, Vol. 1, pp. 170–173 (80CLR11).

*Non-COMSAT Author.
†INTELSAT Author.